

הרצל 234, ת.ד. 26, רחובות 7610001, ישראל  
234 Herzl St., P.O.B 26, Rehovot 7610001, Israel  
www.weizmann.ac.il

טלפון +972-(0)8-934-4237  
פקס +972-(0)8-934-4124  
yinon.rudich@weizmann.ac.il

מכון ויצמן למדע  
WEIZMANN INSTITUTE OF SCIENCE

פרופסור יגון רודיך  
דיקן, פקולטה לכימיה  
**Prof. Yinon Rudich**  
Dean, Faculty of Chemistry

November 30, 2018

Prof. Ryan Sullivan – Editor

Dear Ryn,

We thank you for forwarding the Reviewers' comments to us. Overall, we find them very supportive of our work. We have replied to each one of the comments and changed the manuscript accordingly. Below please find our detailed responses to the 2 Reviewer's' comments and the manuscript and SI with the corrections also made in the text.

Finally, please note that we added Daphne Meidan as a co-author. Daphne contributed to the work and her name was omitted in the ACPD version by mistake.

We hope that we have supplied all the necessary information and that the paper can now be accepted for publication in ACP.

Thank you for handling this manuscript

Yours,

Yinon Rudich

1 *Interactive comment on “Dynamic changes of optical and chemical properties of tar ball aerosols by*  
2 *atmospheric photochemical aging” by Li et al.*

3 **Li et al.**

4 yinon.rudich@weizmann.ac.il

5

6 **Anonymous Referee #1:** Generally speaking, this is an interesting paper where 'tar ball aerosol particles' were  
7 produced and photochemically aged in an OFR. I am not sure whether tar balls in atmospheric aerosol particles  
8 are an important topic. As they are mentioned in the title, the reader expects tar balls to be central for this paper,  
9 but it seems to me, the real topic of the paper is BrC formed after wood combustion, and tar balls have been  
10 identified with that BrC. Maybe the authors can straighten this out with regard to the title and the focus of the  
11 introductory text part. The specific tar ball aerosol generation is interesting. However, this is a laboratory method  
12 to obtain as much as possible tar balls in the generated aerosols. How realistic is this aerosol for the environment?  
13 I wonder if some key parameters of the 'tar ball aerosol' generated in the lab should be given in the experimental,  
14 or, at the latest, early in the results section: Give the particle size distribution, give a rough chemical composition,  
15 OC/EC, WSOC, weight fraction of tar balls. Do these particles still contain inorganic constituents? How much?  
16 When this is not done, the reader starts into the results section without knowledge about what has actually been  
17 generated and is now undergoing heterogeneous oxidation in the OFR. Much of this information is available,  
18 but scatter through the manuscript. I would strongly recommend to introduce a section 'Initial tar ball aerosol  
19 characteristics after generation'. Maybe the chemical information and the optical measurement results should  
20 be separated. Overall, the manuscript call for a better organization. The obtained results are interesting but their  
21 atmospheric relevance should be discussed in view of realistic fraction of tar balls over EC or over OC. Some  
22 statements in the conclusion section are very broad , line 676 ff.

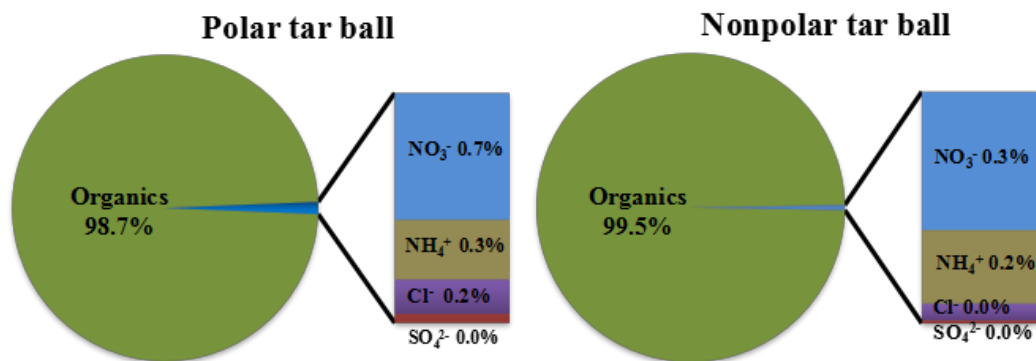
23 **Authors' reply:** We appreciate the Reviewer's general comments. Tar balls are abundant carbonaceous  
24 particles produced by incomplete burning of biofuels. Tar balls contribute a significant number concentration  
25 and mass loading in fire emissions. These ubiquitous particles have strong absorption and present potential light  
26 absorption across the entire solar spectrum. Due to the strong absorption and high concentrations, they can alter  
27 local photochemistry and perturb the radiative balance in the atmosphere on regional and global scales (Pósfai  
28 et al., 2004; Hand et al., 2005; Alexander et al., 2008; Chen et al., 2017; Sedlacek III et al., 2018). In ambient  
29 biomass burning emissions, tar ball particles coexist with other types of pyrolysis particles (e.g., inorganic salts,

30 fly ashes, amorphous carbonaceous aerosol, soot, etc.) as both internal and external mixtures, and they can  
31 undergo rapid atmospheric processes (dilution due to transport, mixing, removal by precipitation,  
32 photochemical and nocturnal oxidation, etc.) once they are released from the fires. Therefore, there are many  
33 practical difficulties in intensive investigation of the chemical and optical properties of ambient wood tar  
34 aerosols.

35 New methods for laboratory generation of tar ball particles from wood pyrolysis have recently been suggested,  
36 and the laboratory-produced tar ball aerosols resemble atmospheric tar balls in most of their observed properties,  
37 including the signature feature of spherical morphology and light absorption, elemental ratio, and similar  
38 chemical compositions (Tóth et al., 2014, 2018; Hoffer et al., 2016, 2017). These laboratory-generated tar balls  
39 are with the similar size range of atmospheric tar ball aerosols (Sedlacek III et al., 2018; Giroto et al., 2018).  
40 This opens up the possibility to conduct detailed laboratory experiments on proxies of tar ball aerosols to  
41 understand their basic physical and chemical processes. In this study, we followed the reported production  
42 protocol (Tóth et al., 2014; Hoffer et al., 2016) to produce liquid wood tar from pyrolysis of wood under high  
43 temperature (dry distillation over 500 °C to mimic a smoldering process), then tar ball droplets were generated  
44 via aerosolization from these tar solutions. The generated tar droplets underwent subsequent dehydration and  
45 heat shock to produce tar ball particles. To study the extensive optical and chemical properties of wood pyrolysis  
46 tar materials, polar and nonpolar tar materials were further separated and concentrated to produce polar and  
47 nonpolar tar ball particles (Hoffer et al., 2016, 2017).

48 Before starting the photochemical aging studies, the laboratory-generated fresh tar ball particles were  
49 extensively characterized and compared with previous studies on ambient biomass burning organic aerosols  
50 (BBOA). As shown in Figure S3 of their morphology (supporting information, SI), the lab-generated tar balls  
51 are amorphous, carbonaceous spherules with major carbon and minor oxygen content. The O/C ratio in the bulk  
52 tar balls was 0.2~0.4 (Figure 2, Table S1 in SI), which is consistent with ambient tar balls and BBOA (Sumlin  
53 et al., 2017, 2018; Aiken et al., 2008; Li et al., 2012; Zhou et al., 2017). The detailed chemical information of  
54 fresh tar balls was obtained using high resolution time-of-flight aerosol mass spectrometer (HR-ToF-AMS) and  
55 by single-particle laser desorption/resonance enhanced multiphoton ionization mass spectrometry (SP-LD-  
56 REMPI-MS). The mass spectra for typical polar and nonpolar tar balls are shown in Figure 2, Figure 3, and  
57 Table S2 (SI). It is clear that the tar balls contain significant fractions of aromatic hydrocarbons and methoxy-  
58 phenolic compounds. These results are consistent with the finding that BBOA or wood tar aerosols consist of  
59 major poly-aromatic hydrocarbons (Tóth et al., 2018, Li et al., 2017; Tivanski et al., 2007; Chen and Bond,  
60 2010). In the manuscript, the mass spectra of these atmospherically-relevant tar balls are extensively described  
61 and compared with previous studies on field and domestic released BBOA.

62 We observed weak signals of inorganic ions (e.g.,  $\text{NO}_3^-$ ,  $\text{Cl}^-$ ,  $\text{SO}_4^{2-}$ , and  $\text{NH}_4^+$ ) in the AMS mass spectra of the  
63 tar balls, and the mass fractions of these inorganics contributed less than 1.5 wt.% of the bulk aerosols in total  
64 (see below Figure R1, pie chart of tar ball chemical composition from AMS measurement), indicating that the  
65 generated wood tar particles are dominantly carbonaceous aerosols, the result has been verified by many studies  
66 (Pósfai et al., 2004; Hand et al., 2005; Adachi and Buseck, 2011).



67

68 Figure R1. Chemical composition of polar and nonpolar tar ball aerosols obtained from AMS measurement

69 Following the Reviewer's suggestion, we measured the OC-EC-TC fractions (total carbon, TC = OC+EC) in  
70 the tar ball aerosols using carbon analyzer based on thermal-optical reflectance (TOR) based on the IMPROVE  
71 protocol. It is clear that the EC content was almost below detection limit for both polar- and nonpolar-tar balls,  
72 the slight EC fraction in nonpolar tar ball is less than 0.7% of the TC content and resides in EC1, which can be  
73 termed as non-refractory char-EC, empirically defined as EC1 – PC. Char-EC is stripped from some OC under  
74 oxygen-free heating during OC/EC measurement, which has much weaker absorption, and thus can be classified  
75 as brown carbon rather than black carbon (Andreae and Gelencsér, 2006; Arora et al., 2015; Kim et al., 2011;  
76 Han et al., 2008, 2009). Many other studies on biomass burning emissions from wildfires and domestic burning  
77 have also reported negligible EC content in tar ball aerosols (Chakrabarty et al., 2010; Tivanski et al., 2007;  
78 Hand et al., 2005; China et al., 2013). These results further support the finding that the composition of the wood  
79 tar we generated is dominated by carbonaceous material.

80 Table R1. Raw blank corrected elemental carbon composition in polar and nonpolar tar ball samples from  
81 thermal-optical measurements

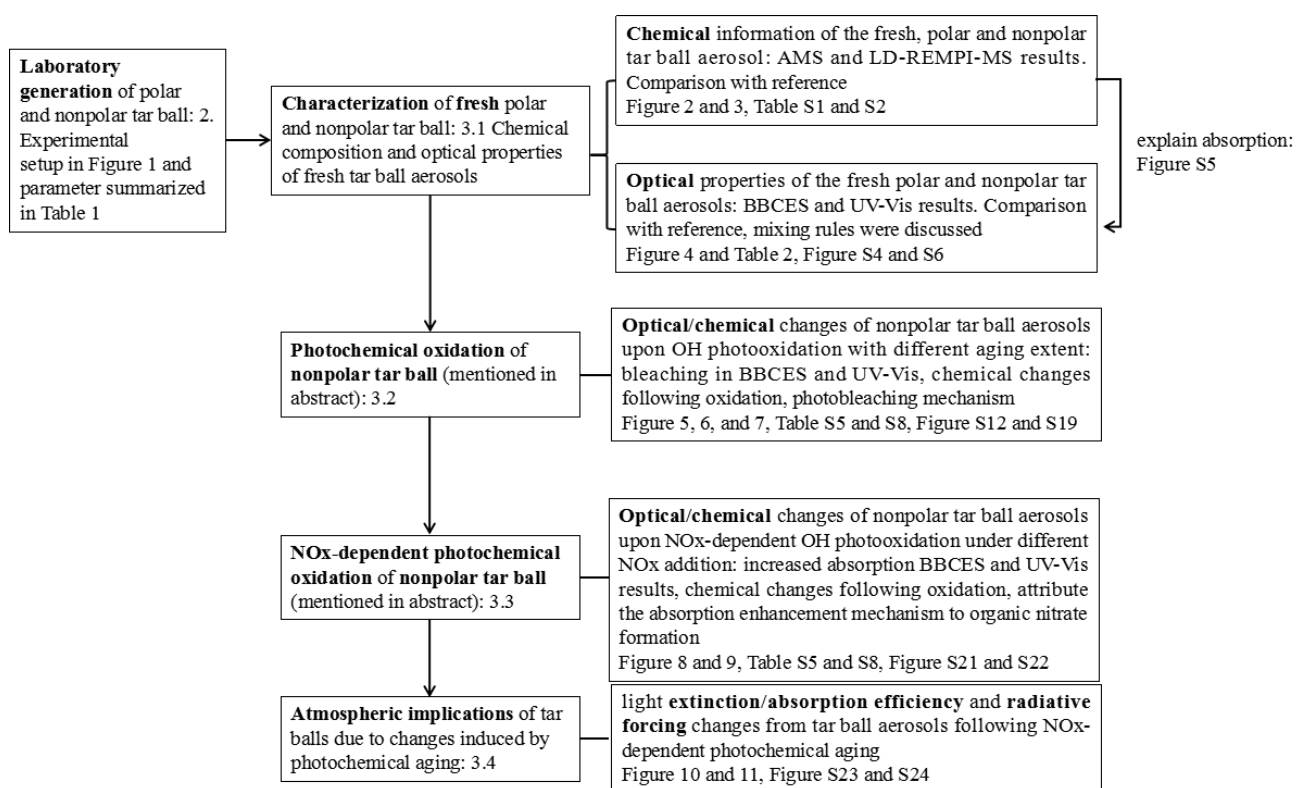
Tar ball	OC1	OC2	OC3	OC4	PC	EC1	EC2	EC3	OC	EC
Carbon ( $\mu\text{g cm}^{-2}$ )										
Polar	7.3	6.1	3.5	0.0	2.0	2.0	0.0	0.0	18.9	0.0
Nonpolar	10.8	9.6	6.0	2.9	7.9	8.1	0.1	0.0	37.2	0.3

82 Note: OC1, OC2, OC3, OC4 are four organic fractions determined at 140, 280, 480, and 580 °C pyrolysis temperatures, respectively, in  
83 a helium (He) atmosphere. EC1, EC2, and EC3 are three EC fractions being oxidized at 580, 740, and 840 °C, respectively, in a 2%  
84 O<sub>2</sub>/98% He atmosphere. OC=OC1+OC2+OC3+OC4+PC, EC=EC1+EC2+EC3-PC.

85 The light absorption properties of laboratory-generated tar balls were also characterized, see Figure 4 and  
86 Table 2. The wavelength-dependent refractive index (RI) was retrieved over the UV-Vis range (365~425nm) for  
87 fresh tar ball aerosols and are reported for the first time and compared with reference values from environmental  
88 tar balls and BBOA (Sedlacek III et al., 2018; Sumlin et al., 2017, 2018; Chakrabarty et al., 2010). The identical

89 values at some discrete wavelength and the spectral-dependence trends of the RI further justify the use of the  
 90 laboratory-generated tar balls for studying the optical and chemical behavior of ambient tar ball and/or BBOA  
 91 in atmospheric process. The RI of tar balls were retrieved based on Mie-Lorenz scattering theory from size- and  
 92 wavelength-resolved extinction cross section measurements of 200~350 nm tar ball aerosols (see the method in  
 93 manuscript and tar ball size distribution in Figure S1, SI).

94 This manuscript focuses on the changes in absorption by tar ball aerosols upon photochemical aging. It was  
 95 found that OH oxidation bleached the tar balls by depleting of absorbing moieties, while addition of NO<sub>x</sub> during  
 96 aging inhibited the bleaching and even restored the absorption of tar balls by forming nitrogen-containing  
 97 functional groups. The changes in the broadband optical properties of the tar balls under different oxidation  
 98 conditions are presented in the paper, and the chemical mechanisms attributing to the optical changes were  
 99 discussed. The entire manuscript follows the following scheme:



100 To summarize: this study probed for the first time changes in the optical and chemical properties of proxies  
 101 for tar ball aerosols due to OH radical aging with different oxidation extent from 0.7 to 6.7 atmospheric  
 102 equivalent days in the presence/absence of NO<sub>x</sub>. We also assessed pristine photolysis under different photon  
 103 fluxes and O<sub>3</sub> oxidation of tar balls in the OFR. Finally the atmospheric and climatic implications of tar balls  
 104 were discussed using a simple radiative transfer model.

105 The particulate inorganic and OC-EC composition have been discussed and added in the manuscript and in the  
 106 supporting information:

107 Page 11, Line 272 in manuscript: “as no other refractory elemental carbon (EC) content was detected in our  
 108 samples with a thermal-optical analysis method (details see in SI).”

109 Page 4 in supporting information: Part 2. OC-EC content of fresh polar and nonpolar tar ball aerosols

110 Page 11, Line 297 in manuscript: “Negligible fractions of inorganics (e.g., sulfate, nitrate, chloride, and  
111 ammonium) in tar balls were obtained from AMS measurement as shown in Fig. S2 (SI), and these results  
112 further confirm that tar ball aerosols are dominated by carbonaceous compounds with minor amounts of N, S,  
113 and Cl (Pósfai et al., 2004; Hand et al., 2005; Adachi and Buseck, 2011). Thereafter, only organics in tar balls  
114 are considered,”

115 Page 5 in supporting information: Part 3.Fresh tar ball composition from HR-Tof-AMS measurement

116 Reference

- 117 Aiken, A. C., Decarlo, P. F., Kroll, J. H., Worsnop, D. R., Huffman, J. A., Docherty, K. S., Ulbrich, I. M., Mohr,  
118 C., Kimmel, J. R., and Sueper, D.: O/C and OM/OC ratios of primary, secondary, and ambient organic aerosols  
119 with high-resolution time-of-flight aerosol mass spectrometry, *Environ. Sci. Technol.*, 42, 4478-4485,  
120 doi: 10.1021/es703009q, 2008.
- 121 Alexander, D. T., Crozier, P. A., and Anderson, J. R.: Brown carbon spheres in East Asian outflow and their  
122 optical properties, *Science*, 321, 833-836, doi: 10.1126/science.1155296, 2008.
- 123 Andreae, M., and Gelencsér, A.: Black carbon or brown carbon? The nature of light-absorbing carbonaceous  
124 aerosols, *Atmos. Chem. Phys.*, 6, 3131-3148, doi:10.5194/acp-6-3131-2006, 2006.
- 125 Arora, P., and Jain, S.: Estimation of organic and elemental carbon emitted from wood burning in traditional  
126 and improved cookstoves using controlled cooking test, *Environ. Sci. Technol.*, 49, 3958-3965,  
127 doi:10.1021/es504012v, 2015.
- 128 Asa-Awuku, A., Sullivan, A., Hennigan, C., Weber, R., and Nenes, A.: Investigation of molar volume and  
129 surfactant characteristics of water-soluble organic compounds in biomass burning aerosol, *Atmos. Chem. Phys.*,  
130 8, 799-812, doi:10.5194/acp-8-799-2008, 2008.
- 131 Bluvshstein, N.; Lin, P.; Flores, J. M.; Segev, L.; Mazar, Y.; Tas, E.; Snider, G.; Weagle, C.; Brown, S. S.; Laskin,  
132 A., Broadband optical properties of biomass - burning aerosol and identification of brown carbon chromophores.  
133 *J. Geophys. Res. Atmos.*, 122, 5441-5456, doi:10.1002/2016JD026230, 2017.
- 134 Chakrabarty, R., Moosmüller, H., Chen, L.-W., Lewis, K., Arnott, W., Mazzoleni, C., Dubey, M., Wold, C., Hao,  
135 W., and Kreidenweis, S.: Brown carbon in tar balls from smoldering biomass combustion, *Atmos. Chem. Phys.*,  
136 10, 6363-6370, doi:10.5194/acp-10-6363-2010, 2010.
- 137 Chen, J., Li, C., Ristovski, Z., Milic, A., Gu, Y., Islam, M. S., Wang, S., Hao, J., Zhang, H., and He, C.: A review  
138 of biomass burning: Emissions and impacts on air quality, health and climate in China, *Sci. Total Environ.*, 579,  
139 1000-1034, doi:10.1016/j.scitotenv.2016.11.025, 2017.
- 140 Chen, Y., and Bond, T.: Light absorption by organic carbon from wood combustion, *Atmos. Chem. Phys.*, 10,  
141 1773-1787, doi:10.5194/acp-10-1773-2010, 2010.
- 142 Giroto, G., China, S., Bhandari, J., Gorkowski, K., Scarnato, B., Capek, T., Marinoni, A., Veghte, D., Kulkarni,  
143 G., and Aiken, A.: Fractal-like Tar Ball Aggregates from Wildfire Smoke, *Environ. Sci. Technol. Lett.*,  
144 doi:10.1021/acs.estlett.8b00229, 2018.
- 145 Han, Y., Han, Z., Cao, J., Chow, J., Watson, J., An, Z., Liu, S., and Zhang, R.: Distribution and origin of  
146 carbonaceous aerosol over a rural high-mountain lake area, Northern China and its transport significance, *Atmos.*  
147 *Environ.*, 42, 2405-2414, doi:10.1016/j.atmosenv.2007.12.020, 2008.
- 148 Han, Y., Lee, S., Cao, J., Ho, K., and An, Z.: Spatial distribution and seasonal variation of char-EC and soot-EC  
149 in the atmosphere over China, *Atmos. Environ.*, 43, 6066-6073, doi:10.1016/j.atmosenv.2009.08.018, 2009.
- 150 Han, Y., Cao, J., Lee, S., Ho, K., and An, Z.: Different characteristics of char and soot in the atmosphere and  
151 their ratio as an indicator for source identification in Xi'an, China, *Atmos. Chem. Phys.*, 10, 595-607,  
152 doi:10.5194/acp-10-595-2010, 2010.

153 Hand, J. L., Malm, W., Laskin, A., Day, D., Lee, T. b., Wang, C., Carrico, C., Carrillo, J., Cowin, J. P., and Collett,  
154 J.: Optical, physical, and chemical properties of tar balls observed during the Yosemite Aerosol Characterization  
155 Study, *J. Geophys. Res. Atmos.*, 110, doi:10.1029/2004JD005728, 2005.

156 Hoffer, A., Tóth, A., Nyirő-Kósa, I., Pósfai, M., and Gelencsér, A.: Light absorption properties of laboratory-  
157 generated tar ball particles, *Atmos. Chem. Phys.*, 16, 239-246, doi:10.5194/acp-16-239-2016, 2016.

158 Hoffer, A., Tóth, Á., Pósfai, M., Chung, C. E., and Gelencsér, A.: Brown carbon absorption in the red and near-  
159 infrared spectral region, *Atmos. Chem. Phys.*, 10, 2353-2359, doi:10.5194/acp-2016-452, 2017.

160 Kim, K. H., Sekiguchi, K., Kudo, S., and Sakamoto, K.: Characteristics of Atmospheric Elemental Carbon(Char  
161 and Soot) in Ultrafine and Fine Particles in a Roadside Environment, Japan, *Aerosol Air Qual. Res.*, 11, 1-12,  
162 doi:10.4209/aaqr.2010.07.0061, 2011.

163 Li, C., Hu, Y., Zhang, F., Chen, J., Ma, Z., Ye, X., Yang, X., Wang, L., Tang, X., and Zhang, R.: Multi-pollutant  
164 emissions from the burning of major agricultural residues in China and the related health-economic effects,  
165 *Atmos. Chem. Phys.*, 17, 4957-4988, doi: 10.5194/acp-17-4957-2017, 2017.

166 Li, Y. J., Yeung, J. W., Leung, T. P., Lau, A. P., and Chan, C. K.: Characterization of organic particles from  
167 incense burning using an aerodyne high-resolution time-of-flight aerosol mass spectrometer, *Aerosol Sci.*  
168 *Technol.*, 46, 654-665, doi:10.1080/02786826.2011.653017, 2012.

169 Lin, P., Bluvshstein, N., Rudich, Y., Nizkorodov, S. A., Laskin, J., and Laskin, A.: Molecular Chemistry of  
170 Atmospheric Brown Carbon Inferred from a Nationwide Biomass Burning Event, *Environ. Sci. Technol.*, 51,  
171 11561-11570, doi:10.1021/acs.est.7b02276, 2017.

172 Lin, P.; Fleming, L. T.; Nizkorodov, S. A.; Laskin, J.; Laskin, A., Comprehensive Molecular Characterization  
173 of Atmospheric Brown Carbon by High Resolution Mass Spectrometry with Electrospray and Atmospheric  
174 Pressure Photoionization. *Anal. Chem.*, 90, 12439-12502, doi:10.1021/acs.analchem.8b02177, 2018.

175 Pósfai, M., Gelencsér, A., Simonics, R., Arató, K., Li, J., Hobbs, P. V., and Buseck, P. R.: Atmospheric tar balls:  
176 Particles from biomass and biofuel burning, *J. Geophys. Res. Atmos.*, 109, doi:10.1029/2003JD004169, 2004.

177 Rajput, P., and Sarin, M.: Polar and non-polar organic aerosols from large-scale agricultural-waste burning  
178 emissions in Northern India: implications to organic mass-to-organic carbon ratio, *Chemosphere*, 103, 74-79,  
179 doi:10.1016/j.chemosphere.2013.11.028, 2014.

180 Sedlacek III, A. J., Buseck, P. R., Adachi, K., Onasch, T. B., Springston, S. R., and Kleinman, L.: Formation  
181 and evolution of Tar Balls from Northwestern US wildfires, *Atmos. Chem. Phys.*, 18, 11289-11301,  
182 doi:10.5194/acp-18-11289-2018, 2018.

183 Sengupta, D., Samburova, V., Bhattarai, C., Kirillova, E., Mazzoleni, L., Iaukea-Lum, M., Watts, A., Moosmü  
184 ller, H., and Khlystov, A.: Light absorption by polar and non-polar aerosol compounds from laboratory biomass  
185 combustion, *Atmos. Chem. Phys.*, 18, 10849-10867, doi:10.5194/acp-18-10849-2018, 2018.

186 Sumlin, B. J., Pandey, A., Walker, M. J., Pattison, R. S., Williams, B. J., and Chakrabarty, R. K.: Atmospheric  
187 Photooxidation Diminishes Light Absorption by Primary Brown Carbon Aerosol from Biomass Burning,  
188 *Environ. Sci. Technol. Lett.*, 4, 540-545, doi:10.1021/acs.estlett.7b00393, 2017.

- 189 Sumlin, B. J., Oxford, C. R., Seo, B., Pattison, R. R., Williams, B. J., and Chakrabarty, R. K.: Density and  
190 homogeneous internal composition of primary brown carbon aerosol, *Environ. Sci. Technol.*, 52, 3982-3989,  
191 doi: 10.1021/acs.est.8b00093, 2018.
- 192 Tivanski, A. V., Hopkins, R. J., Tyliszczak, T., and Gilles, M. K.: Oxygenated interface on biomass burn tar  
193 balls determined by single particle scanning transmission X-ray microscopy, *J. Phys. Chem. A*, 111, 5448-5458,  
194 doi: 10.1021/jp070155u, 2007.
- 195 Tóth, A., Hoffer, A., Nyirő-Kósa, I., Pósfai, M., and Gelencsér, A.: Atmospheric tar balls: aged primary droplets  
196 from biomass burning?, *Atmos. Chem. Phys.*, 14, 6669-6675, doi:10.5194/acp-14-6669-2014, 2014.
- 197 Tóth, Á., Hoffer, A., Pósfai, M., Ajtai, T., Kónya, Z., Blazsó, M., Czégény, Z., Kiss, G., Bozóki, Z., and Gelencsér,  
198 A.: Chemical characterization of laboratory-generated tar ball particles, *Atmos. Chem. Phys.*, 18, 10407-  
199 10418, doi:10.5194/acp-18-10407-2018, 2018.
- 200 Zhou, S., Collier, S., Jaffe, D. A., Briggs, N. L., Hee, J., Sedlacek III, A. J., Kleinman, L., Onasch, T. B., and  
201 Zhang, Q.: Regional influence of wildfires on aerosol chemistry in the western US and insights into atmospheric  
202 aging of biomass burning organic aerosol, *Atmos. Chem. Phys.*, 17, 2477-2493, doi:10.5194/acp-17-2477-2017,  
203 2017.

204

205

206

1 **Anonymous Referee #2:** This manuscript describes the systematic study of how the chemical  
2 and optical properties of laboratory-generated tar ball aerosols change upon reaction with OH,  
3 exposure to 254 nm light and oxidation in the presence of NO<sub>x</sub>. What is really interesting  
4 about this study is that the authors extracted the polar (water-soluble) and non-polar fractions  
5 and found significant differences in both chemical composition and the responses to oxidation.  
6 The formation of organic-nitrates was found to increase absorption, which at least partially  
7 offsets the decrease in absorption (“bleaching”) observed upon photolysis and oxidation by  
8 OH radicals. By using a range of EADs (Equivalent daytime Atmospheric oxidation Days) of  
9 ~0.5-7 days, the authors explore atmospherically relevant extents of oxidation. The use and  
10 description of a controlled method for obtaining reproducible tar ball extract samples in the  
11 laboratory is also important. This procedure allows the authors to make systematic studies of  
12 semi-authentic aerosol samples that appear to be consistent with ambient tar ball samples.  
13 Overall, this manuscript is well written, and the data are interpreted carefully. Given the  
14 growing evidence of the importance of tar balls in atmospheric aerosols and the open  
15 questions about brown carbon’s molecular composition, this manuscript is an important  
16 contribution in this area and is appropriate for ACPD.

17 Specific comments:

18 1. Since the photolysis was carried out at only one wavelength, 254 nm, statements about  
19 increases in absorption from the formation of organic-nitrates offsetting bleaching from  
20 photolysis should be highly qualified.

21 **Authors’ reply:** We thanks the Reviewer for the thoughtful comments. Tar ball particles  
22 underwent photochemical aging in the OFR. This included NO<sub>x</sub>-dependent OH  
23 photooxidation and photolysis at 254 nm. We suggest that NO<sub>x</sub>-dependent OH radical aging  
24 should be the dominant photochemical pathway that bleach, darken and oxidize tar balls  
25 (Sumlin et al., 2017). The role of photolysis in tar ball chemical and optical changes were  
26 investigated, and the results are discussed in detail in the Supporting Information Part 12  
27 **(Optical and chemical changes for tar ball aerosols due to photolysis from UV light  
28 irradiation in the OFR)**. Specifically, we exposed the tar balls to the same aging condition  
29 without O<sub>3</sub> and NO<sub>x</sub> addition, where the actual UV flux is higher without O<sub>3</sub>, RO<sub>2</sub>/HO<sub>2</sub>  
30 radicals and NO<sub>x</sub> that absorb some of the photons. However, no significant chemical and RI  
31 changes were observed in the tar balls even under maximum UV flux in the OFR. On the  
32 experimental time scale (residence time ~144s in the OFR), the small observed changes  
33 during photolysis can be neglected compared to the extensive bleaching and oxidation  
34 observed under the same conditions in presence of OH radical. We have clarified these points  
35 in the paper ([Page 18, Line 496-504](#)).

36 It was also found that addition of NO<sub>x</sub> restored absorption and counteracted the OH  
37 photochemical bleaching of the tar balls to facilitate absorption under high NO<sub>x</sub> concentration.  
38 We suggest that the formation of organic nitrates offsets the bleaching from photolysis and  
39 from OH photooxidation to eventually enhance light absorption of the tar balls. It is correct  
40 that 254nm UV photolysis in the OFR does not represent the solar irradiation in the  
41 atmosphere, it is arbitrary to state that increases in absorption from the formation of  
42 organic-nitrates offset bleaching from photolysis. We corrected this statement ([Page 2, Line  
43 35-36](#)), and we will quantify the photolysis and OH radical oxidation effect in a following

44 study, and study the chemical process of some related organic-nitrates during their lifetime in  
45 the atmosphere.

46 Page 2, Line 35-36 in manuscript: “These observations suggest that secondary organic nitrate  
47 formation counteracts the bleaching by OH radical photooxidation to eventually regain some  
48 absorption of the tar balls aerosols.”

49 2. Equation 4: How is the mass concentration of the solution,  $C$ , determined in calculating the  
50 MAC (mass absorption cross section)?

51 **Authors’ reply:** The mass concentration of BrC extracted in methanol solution was calculated  
52 to be in the range of 0.01~0.02 g L<sup>-1</sup>. The BrC concentration was calculated from filter mass  
53 loading of tar ball aerosol (100~150 μg), methanol volume (7.5 mL) assuming hundred  
54 percent extraction efficiency, and OM/OC ratio from AMS measurement. The mass loading  
55 for each filter sample was estimated from the aerosol volume distribution measured by SMPS,  
56 particle density measured from AAC-SMPS (~1.24-1.33 g cm<sup>-3</sup>), and the total sampling  
57 volume. The BrC mass concentration can be calculated by the function shown below:

$$C_{BrC} = \frac{V_{tar} \times \rho_{eff} \times t \times v}{V_{methanol}} \times r$$

58 Where  $V_{tar}$  is the tar ball aerosol volume concentration measured by SMPS between 14 and  
59 670 nm,  $\rho_{eff}$  is effective density calculated from aerodynamic and electric-mobility  
60 distribution for fixed monodispersed tar ball,  $t$  is the filter sampling time,  $v$  is filter sampling  
61 flow,  $V_{methanol}$  is the total volume of solvent used to extract the filter sample,  $r$  is organic  
62 carbon (OC) fraction in tar ball aerosol, which can be derived from AMS measurement of  
63 OC/OM with the assumption that the EC content can be neglected in tar ball aerosol (as  
64 discussed above).

65 We added this information in the methods part of the manuscript:

66 Page10 Line 270 in manuscript: “ $C$  is the extracted organic carbon mass concentration in  
67 solvent (g m<sup>-3</sup>), which can be determined directly by normalizing the extract concentration  
68 and OC mass fraction for tar balls as OC/OM obtained from AMS data, as no other refractory  
69 elemental carbon (EC) content was detected in our samples (details see in SI).”

70

71 3. Line 597: “EAD” should be “EDA”.

72 **Authors’ reply:** Thanks. “EAD” has been corrected in Page 22, Lin 620.

73

74 4. What fraction of the mass and/or the absorption is attributable to the polar vs. the non-polar  
75 fractions?

76 **Authors’ reply:** In this study, light absorbing properties of polar and nonpolar chemical  
77 matrix from wood pyrolysis were characterized. We found that the refractive index for the  
78 mixture of polar and nonpolar organic fractions fit both volume and molar mixing rules (see  
79 supporting information of prediction of mixture tar ball optical properties based on different  
80 mixing rules). However, the actual fractions of the polar and nonpolar compounds

81 contributing to the mass/absorption of ambient tar ball or BBOA are still under study, as they  
82 vary with biofuel, burning conditions, atmospheric processes, and also the method/efficiency  
83 used to classify the polar and nonpolar materials from the sample (Sengupta., et al., 2018; Lin  
84 et al., 2017; Chen and Bond, et al., 2010; Sumlin et al., 2017) (Page 6, Line 133-137).  
85 According to most previous studies, the nonpolar or less polar fractions have higher  
86 absorption properties compared with the polar fraction from BBOA. Sengupta et al. (2018)  
87 reported that the fuel mass normalized nonpolar fraction is 2-3 times more absorbing than the  
88 polar fraction, and complex fuel-dependence and atmospheric aging dependence were  
89 observed for absorption changes of both fractions. Lin et al. (2017) and Bluvshstein et al.  
90 (2017) tracked the absorption changes of BBOA with respect to different solvent extraction  
91 during a whole fire episode, and found distinct different absorbing features for the  
92 water-extracted fraction compared to the organic solvent extracts, while acetonitrile and  
93 orgmix (acetonitrile: dichloromethane: hexane = 2:2:1, v/v) extracts exhibited similar  
94 absorption. According to Lin et al. (2017), from the beginning to the end of the fire event,  
95 organic extracts showed higher light absorption at shorter wavelength ( $\lambda < 380$  nm). In contrast,  
96 higher light absorption with an absorption feature around 450 nm (attributed to nitro-phenols)  
97 hump was observed for water extracts.

98 Rajput et al. (2014) classified the mass fractions of polar and nonpolar organic matter from  
99 agricultural-waste burning emissions. Nearly 85 wt.% of the burning organic emissions was  
100 attributed to a polar fraction, and this fraction from wheat residue burning was much lower  
101 than from paddy burning. Asa-Awuku et al. (2008) suggested that relative molar proportion of  
102 nonpolar (hydrophobic) to polar (hydrophilic) compounds in original biomass burning aerosol  
103 is 1:3 from Köhler Theory Analysis (Page 6, Line 133-137; Page 17, Line 451-456).

104 In short, the polar fraction dominates the bulk organic aerosol from biomass burning.  
105 However, the real polar fraction in the tar balls is undefined, as tar balls belong to BBOA but  
106 from specific burning condition with special physicochemical properties. The topic raised in  
107 the Reviewer's question will be part of our following research topic to investigate the exact  
108 contribution of both the polar/nonpolar matrix and to identify specific chromophore  
109 molecules to tar ball aerosol absorption/mass. We have sent the samples of the fresh and aged  
110 laboratory-generated polar/nonpolar tar ball for extensive molecular chemical analysis using  
111 HPLC/PDA/HRMS (high performance liquid chromatography platform coupled to  
112 photo-diode array and high resolution mass spectrometry detectors) and other common MS  
113 techniques (e.g., ESI/APPI-MS, electrospray ionization/atmospheric pressure photo ionization  
114 mass spectrometry), the results will be published in a different manuscript.

115 We have added the discussion of polar and nonpolar fractions contribution to tar ball  
116 aerosols mass and absorption in the manuscript:

117 Page 6, Line 133-137: "The actual fractions of the polar and nonpolar compounds  
118 contributing to the mass of ambient tar ball or biomass burning organic aerosol (BBOA) can  
119 vary with biofuel sources, burning condition, atmospheric process, and also method/efficiency  
120 to classify the polar and nonpolar materials from the sample (Sengupta., et al., 2018; Lin et al.,  
121 2017, 2018; Chen and Bond, et al., 2010; Rajput et al., 2008),"

122 Page 17, Line 451-456: "As mentioned above, the real fractions of polar and nonpolar BrC  
123 contributing to the mass/absorption of BBOA are undefined, some investigations report that

124 the polar BrC dominate the tar balls' mass (50~85%), but contribute less to the absorption in  
125 BBOA (less than 40%) (Asa-Awuku et al., 2008; Bluvshstein et al., 2017; Lin et al., 2017,  
126 2018; Rajput et al., 2014; Sengupta et al., 2018). The "linear mixing rule" confirmed in this  
127 study should be helpful in the mathematical modeling to assess the climatic impacts of  
128 biomass burning related BrC aerosol, when their chemical composition is classified."

129 Reference

130 Asa-Awuku, A., Sullivan, A., Hennigan, C., Weber, R., and Nenes, A.: Investigation of molar  
131 volume and surfactant characteristics of water-soluble organic compounds in biomass burning  
132 aerosol, *Atmos. Chem. Phys.*, 8, 799-812, doi:10.5194/acp-8-799-2008, 2008.

133 Bluvshstein, N.; Lin, P.; Flores, J. M.; Segev, L.; Mazar, Y.; Tas, E.; Snider, G.; Weagle, C.;  
134 Brown, S. S.; Laskin, A., Broadband optical properties of biomass - burning aerosol and  
135 identification of brown carbon chromophores. *J. Geophys. Res. Atmos.*, 122, 5441-5456,  
136 doi:10.1002/2016JD026230, 2017.

137 Chen, Y., and Bond, T.: Light absorption by organic carbon from wood combustion, *Atmos.*  
138 *Chem. Phys.*, 10, 1773-1787, doi:10.5194/acp-10-1773-2010, 2010.

139 Lin, P., Bluvshstein, N., Rudich, Y., Nizkorodov, S. A., Laskin, J., and Laskin, A.: Molecular  
140 Chemistry of Atmospheric Brown Carbon Inferred from a Nationwide Biomass Burning  
141 Event, *Environ. Sci. Technol.*, 51, 11561-11570, doi:10.1021/acs.est.7b02276, 2017.

142 Lin, P.; Fleming, L. T.; Nizkorodov, S. A.; Laskin, J.; Laskin, A., Comprehensive Molecular  
143 Characterization of Atmospheric Brown Carbon by High Resolution Mass Spectrometry with  
144 Electrospray and Atmospheric Pressure Photoionization. *Anal. Chem.*, 90, 12439-12502,  
145 doi:10.1021/acs.analchem.8b02177, 2018.

146 Rajput, P., and Sarin, M.: Polar and non-polar organic aerosols from large-scale  
147 agricultural-waste burning emissions in Northern India: implications to organic  
148 mass-to-organic carbon ratio, *Chemosphere*, 103, 74-79,  
149 doi:10.1016/j.chemosphere.2013.11.028, 2014.

150 Sengupta, D., Samburova, V., Bhattarai, C., Kirillova, E., Mazzoleni, L., Iaukea-Lum, M.,  
151 Watts, A., Moosmüller, H., and Khlystov, A.: Light absorption by polar and non-polar aerosol  
152 compounds from laboratory biomass combustion, *Atmos. Chem. Phys.*, 18, 10849-10867,  
153 doi:10.5194/acp-18-10849-2018, 2018.

154 Sumlin, B. J., Pandey, A., Walker, M. J., Pattison, R. S., Williams, B. J., and Chakrabarty, R.  
155 K.: Atmospheric Photooxidation Diminishes Light Absorption by Primary Brown Carbon  
156 Aerosol from Biomass Burning, *Environ. Sci. Technol. Lett.*, 4, 540-545,  
157 doi:10.1021/acs.estlett.7b00393, 2017.

158

1 **Dynamic changes of optical and chemical properties of tar ball**  
2 **aerosols by atmospheric photochemical aging**

3 Chunlin Li,<sup>†</sup> Quanfu He,<sup>†</sup> Julian Schade,<sup>‡</sup> Johannes Passig,<sup>‡,§</sup> Ralf Zimmermann,<sup>‡,§</sup> **Daphne**  
4 **Meidan**,<sup>†</sup> Alexander Laskin,<sup>§</sup> and Yinon Rudich<sup>†,\*</sup>

5 <sup>†</sup>Department of Earth and Planetary Sciences, Weizmann Institute of Science, Rehovot 76100, Israel

6 <sup>‡</sup>Joint Mass Spectrometry Centre, University of Rostock, Dr.-Lorenz-Weg 2, 18059 Rostock, Germany

7 <sup>§</sup>Joint Mass Spectrometry Centre, Cooperation Group ‘Comprehensive Molecular Analytics’ (CMA), Helmholtz  
8 Zentrum München, Ingolstädter Landstrasse 1, 85764 Neuherberg, Germany

9 <sup>§</sup>Department of Chemistry, Purdue University, West Lafayette, Indiana 47907, United States

10

11 *Correspondence to:* Yinon Rudich (yinin.rudich@weizmann.ac.il)

12 **Abstract.** Following wood pyrolysis, tar ball aerosols were laboratory generated from wood tar separated into  
13 polar and nonpolar phases. Chemical information of fresh tar balls was obtained from a high-resolution time-of-  
14 flight aerosol mass spectrometer (HR-ToF-AMS) and single-particle laser desorption/resonance enhanced  
15 multiphoton ionization mass spectrometry (SP-LD-REMPI-MS). Their continuous refractive index (RI) between  
16 365 and 425 nm was retrieved using a broadband cavity enhanced spectroscopy (BBCES). Dynamic changes of  
17 the optical and chemical properties for the nonpolar tar ball aerosols in NO<sub>x</sub>-dependent photochemical process  
18 were investigated in an oxidation flow reactor (OFR). Distinct differences in the chemical composition of the  
19 fresh polar and nonpolar tar aerosols were identified. Nonpolar tar aerosols contain predominantly high-molecular  
20 weight unsubstituted and alkyl-substituted polycyclic aromatic hydrocarbons (PAHs), while polar tar aerosols  
21 consist of a high number of oxidized aromatic substances (e.g., methoxy-phenols, benzenediol) with higher O:C  
22 ratio and carbon oxidation state. Fresh tar balls have light absorption characteristics similar to atmospheric brown  
23 carbon (BrC) aerosol with higher absorption efficiency towards the UV wavelengths. The average retrieved RI is  
24  $1.661+0.020i$  and  $1.635+0.003i$  for the nonpolar and polar tar aerosols, respectively, with absorption Ångström  
25 exponent (AAE) between 5.7 and 7.8 in the detected wavelength range. The RI fits a volume mixing rule for  
26 internally mixed nonpolar/polar tar balls. The RI of the tar ball aerosols decreased with increasing wavelength  
27 under photochemical oxidation. Photolysis by UV light (254 nm), without strong oxidants in the system, slightly  
28 decreased the RI and increased the oxidation state of the tar balls. Oxidation under varying OH exposure levels  
29 and in the absence of NO<sub>x</sub> diminished the absorption (bleaching), and increased the O:C ratio of the tar balls. The  
30 photobleaching via OH radical initiated oxidation is mainly attributed to decomposition of chromophoric  
31 aromatics, nitrogen-containing organics, and high-molecular weight components in the aged particles. Photolysis  
32 of nitrous oxide (N<sub>2</sub>O) was used to simulate NO<sub>x</sub>-dependent photochemical aging of tar balls in the OFR. Under  
33 high NO<sub>x</sub> condition with similar OH exposure, photochemical aging lead to the formation of organic-nitrates,  
34 increased both oxidation degree and light absorption for the aged tar ball aerosols. These observations suggest  
35 that secondary organic nitrate formation counteracts the bleaching by OH radical photooxidation to eventually  
36 regain some absorption of the aged tar balls aerosols. The atmospheric implication and climate effects from tar  
37 balls upon various oxidation processes are briefly discussed.

## 38 1 Introduction

39 Organic aerosol (OA), which represent a ubiquitous and dominant burden of the tropospheric particulate pollutants,  
40 play important roles in atmospheric chemistry and balance of regional and global radiation (Jimenez et al., 2009;  
41 Kanakidou et al., 2005; Seinfeld and Pandis, 2016; Shrivastava et al., 2017). An indirect climate influence of OA  
42 relies on their interaction with water thus acting as cloud condensation nuclei (CCN) that may alter the  
43 hydrological cycle (cloud formation and perception) and modify Earth's albedo (Forster and Taylor, 2006; IPCC,  
44 2013; Seinfeld and Pandis, 2016). The direct climate effect of OA is through extinction of incoming solar radiation  
45 and outgoing longwave radiation. Of particular importance is the warming effect due to light-absorbing  
46 carbonaceous aerosol commonly termed as brown carbon (BrC) (Andreae and Gelencsér, 2006). BrC is an  
47 important yet poorly understood OA component due to its complex physical properties, undefined chemical  
48 composition, and also its dynamic evolution under atmospheric processes (Adler et al., 2010; Moise et al., 2015;  
49 Laskin et al. 2015). It has been estimated that BrC accounts for 10-40% of the total light absorption in the  
50 atmosphere and when deposited on snow pack (Bahadur et al., 2012; Park et al., 2010), and contributes to global  
51 forcing of 0.10-0.25 W m<sup>-2</sup>, with even higher values on regional scales (Feng et al., 2013).

52 The origin of BrC can be either primary (i.e., directly emitted) or secondary (i.e., generated by reactions of  
53 aromatic or carbonyl compounds in clouds or particles) (Laskin et al., 2015). On a global scale, biomass burning  
54 releases over two-thirds of primary BrC and also contributes substantially to overall secondary OA formation  
55 (Jacobson, 2014; Jo et al., 2016). Better understanding of the optical properties of biomass burning BrC aerosols  
56 is crucial for constraining its atmospheric and climatic implications and Earth's energy balance. Unlike black  
57 carbon that absorbs light strongly throughout the entire UV-visible range, different chromophores that may also  
58 be coupled via charge transfer complexes enable BrC absorption in a much more pronounced and complicated  
59 wavelength-dependence manner (Phillips and Smith, 2004; Reid et al., 2005; Lin et al., 2016, 2017).

60 Tar balls are a specific type of particles produced from wood combustion (especially from biomass  
61 smoldering burning) which are abundant in the troposphere (Pósfai et al., 2004; Hand et al., 2005; Chen et al.,  
62 2017). Tar ball particles have been collected and identified in many biomass burning plumes (Pósfai et al., 2004;  
63 Fu et al., 2012; Li et al., 2017). Microanalysis has found that tar balls are homogeneous spherical carbonaceous  
64 particles with sizes ranging from tens to hundreds of nanometers. These particles contribute a considerable fraction  
65 of the biomass burning BrC (Pósfai et al., 2004; Hand et al., 2005; Li et al., 2017). The estimated burden of tar  
66 balls on regional and global climatic forcing has been emphasized ([Chung et al., 2012](#); [Jacobson, 2012, 2014](#)).

67 Tar balls from different burning conditions and bio-fuels coexist with many other types of particles (e.g., inorganic  
68 salts, soot, and other carbonaceous aerosols in form of internal or external mixing), and these smoke particles  
69 undergo rapid atmospheric processing once they are released from the fire (Pósfai et al., 2004; Hand et al., 2005;  
70 Li et al., 2015, 2017). However, *in situ* determination of the optical properties of these particles during their  
71 lifetimes in the air has seldom been reported due to inherent difficulty in selective tar balls sampling out of  
72 complex particle ensembles typical of field burning emissions.

73 The complex refractive index ( $RI=n+ki$ ,  $n$  and  $k$  are real and imaginary parts, corresponding to scattering  
74 and absorption, respectively) is an intrinsic optical property of aerosols. Quantifying the RI of OA is highly needed  
75 for evaluating the related radiative forcing influence (Moise et al., 2015). Recently, several studies have  
76 investigated the optical properties of tar ball particles (Chakrabarty et al., 2010; Hoffer et al., 2016;  
77 Sedlacek et al., 2018). The optical measurements reported for tar balls or other biomass burning BrC, were  
78 discrete over several wavelengths that were constrained by instruments measuring particle light coefficients, or  
79 indirectly inferred from calculations based on their electron energy-loss spectra or from UV-Vis absorption of  
80 solutions containing dissolved tar balls (Alexander et al., 2008). Hand et al. (2005) measured light scattering  
81 coefficients of tar balls-dominated fire plumes using a nephelometer, and reconstructed the scattering coefficients  
82 with simplified organic carbon (OC) and elemental carbon (EC) data to get an average RI of  $1.56+0.02i$  for tar  
83 balls at  $\lambda = 632$  nm. Chakrabarty et al. (2010) measured the RI of tar ball particles from smoldering biomass  
84 combustion at 405, 532, and 780 nm, they observed a clear wavelength-, biofuel-, and even burning condition-  
85 dependent RI. The light absorption by tar balls was similar to humic-like substance (HULIS) with an imaginary  
86 part (0.002~0.015) that increased exponentially towards the near UV wavelengths. Recently, Hoffer et al. (2016)  
87 generated tar ball particles from flameless wood pyrolysis in the laboratory. They reported a higher RI value of  
88  $1.84+0.20i$  at 550 nm, which fell closer to RI of soot than to that of HULIS. Large discrepancies reside in these  
89 results and discrete RI values make it difficult to decipher the complicated wavelength-dependence character of  
90 tar balls optical properties, which finally constrains the assessment of its radiative forcing effect.

91 Freshly emitted smoke BrC contain chromophores with diverse chemical structures, polarity, and volatility  
92 (Lin et al., 2016, 2017). After emission into the atmosphere, smoke particles undergo dynamic changes as a result  
93 of dilution, precipitation, and chemical processing on scales of seconds to days, which eventually affect the  
94 physiochemical properties of BrC particles during their lifetimes in the atmosphere (Reid et al., 2005; Li et al.,  
95 2015; Laskin et al., 2015). Sumlin et al. (2017) simulated atmospheric photooxidation of biomass burning BrC,  
96 and reported that photooxidation diminishes their light absorption. Zhong and Jang (2014) investigated the

107 influence of humidity and NO<sub>x</sub> presence in photochemical aging of biomass burning BrC. They found that  
108 sunlight faded the color of BrC, and humidity facilitated the decay of light absorption by BrC, while presence of  
109 NO<sub>x</sub> delayed the fading. Overall, they concluded that light absorption by BrC is governed by chromophores  
110 formation and bleaching by sunlight in the atmosphere. Therefore, evaluating the climatic impacts of tar ball  
111 particles requires more extensive investigation of its optical properties, and understanding of the dynamic  
112 transformations of the optical properties during atmospheric aging.

113 In this study, we generated proxies for tar ball particles by flameless wood pyrolysis (Tóth et al., 2014; Hoffer  
114 et al., 2016). This method allows consistent and continuous generation of tar ball proxy aerosols for studying their  
115 properties and processes. The RI of the tar aerosols as a function of wavelength in the ultraviolet-short visible  
116 region (365~425nm, 0.5 nm resolution) was determined using a broadband cavity enhanced spectrometer  
117 (BBCES). A high resolution time of flight aerosol mass spectrometer (HR-ToF-AMS) and a single-particle mass  
118 spectrometer applying laser desorption/resonantly enhanced multiphoton ionization (SP-LD-REMPI-MS) were  
119 used for probing the chemical profile of tar ball aerosols under NO<sub>x</sub>-dependent multiple-day photochemical  
120 oxidation. Specifically, the dynamic changes of their optical properties in correlation with their chemical  
121 composition were investigated. The atmospheric implications and climate forcing due to atmospheric aging of tar  
122 aerosols and evolution of their optical properties were also explored.

## 113 2 Experiment

### 114 2.1 Tar ball particle generation

115 Following the formation mechanism in biomass burning process, polydisperse tar ball particles were generated  
116 from droplets of wood tar in the laboratory (Tóth et al., 2014; Hoffer et al., 2016). In this study, a similar procedure  
117 was applied for producing tar ball aerosols. In brief, commercial wood pellets (Hallingdal Trepellets, water content  
118 of 6.55 wt.%, size of 2~3 cm in length, 0.2-0.3 cm in diameter) were smashed, heated and dry-distilled in absence  
119 of air (25°C min<sup>-1</sup> increase to 530 °C from room temperature, and held for 20 min at 530 °C) to produce liquid tar-  
120 water emulsions (~25 mL per hundred grams of used wood pellets). The emulsions were filtrated using 0.45 μm  
121 pore size filters (PTFE membrane, diameter 47 mm, Pall Corp.) to remove particulate matter or solid precipitation.  
122 After overnight static stabilization, the wood tar solution was phase-separated into water soluble and non-soluble  
123 oily phases at an initial 3:1 volume ratio. Herein, we will term these two fractions as ‘polar’ and ‘nonpolar’ phases,  
124 respectively. The phase-separated solution was further concentrated using a heating plate at 300 °C with N<sub>2</sub> purge  
125 flow to prevent oxidation. A final 1:1 volume ratio of polar to nonpolar phase was obtained; then the concentrated

126 solutions were sealed and stored in the dark under 2 °C for following experiments. With respect to their potential  
127 reactivity and instability, the distillation products were used within a few days.

128 For particle optical measurement, tar balls were produced from aerosolization of above predefined wood tar  
129 diluted in methanol (Gradient grade for HPLC, purity $\geq$ 99.9 wt.%, Merck) using a constant output atomizer (Model  
130 3076, TSI) with high-purity N<sub>2</sub> as a carrier gas. As the actual fractions of the polar and nonpolar compounds  
131 contributing to the mass of ambient tar ball or biomass burning organic aerosol (BBOA) can vary with biofuel  
132 sources, burning condition, atmospheric process, and also method/efficiency to classify the polar and nonpolar  
133 materials from the sample (Sengupta, et al., 2018; Lin et al., 2017, 2018; Chen and Bond, et al., 2010; Rajput et  
134 al., 2008), tar ball aerosols in this study were generated from polar, nonpolar, and mixtures of two phase tar  
135 solutions at volume mixing ratio of 2:1, 1:1, and 1:2, respectively. Activated charcoal denuders and quartz heating  
136 tube (150 °C, residence time ~0.7s for particles at a nitrogen flow of 1.0 LPM) were used after the atomizer to  
137 outgas the methanol from the gaseous and particulate phases. Mesh filters (TSI) downstream were used to filter  
138 out some ultrafine (less than 100 nm) particles.

## 139 2.2 NO<sub>x</sub>-dependent OH oxidation of tar ball aerosols

140 Heterogeneous oxidation of tar ball aerosols was simulated using an oxidation flow Reactor (OFR), shown  
141 schematically in [Fig. 1](#). The OFR has been characterized (Kang et al., 2007; Peng et al., 2015, 2016) and the  
142 operational procedures have been described previously (He et al. 2018). Briefly, the OFR consists of a horizontal  
143 13.3 L aluminum cylindrical chamber (46 cm long  $\times$  22 cm ID) operating in continuous flow mode. The chamber  
144 is equipped with two power controllable ozone-free mercury-lamps with peak emission at  $\lambda=254$  nm (82-934-08,  
145 BHK Inc., CA, USA). The two UV lamps are surrounded by Pyrex sheath tubes that are continuously purged with  
146 N<sub>2</sub> to cool the lamps and remove outgassing compounds. OH radicals in the OFR are produced through photolysis  
147 of externally introduced O<sub>3</sub> under 254 nm illumination and the further reaction of singlet oxygen (O<sup>1</sup>D) with water  
148 vapor:



151 External O<sub>3</sub> was produced by irradiation of 0.2 LPM high purity O<sub>2</sub> using a mercury lamp ( $\lambda=185$ nm, 78-2046-  
152 07, BHK Inc., CA). The O<sub>3</sub> concentration downstream of the OFR was measured by an O<sub>3</sub> monitor (2B  
153 Technology). A Nafion membrane humidifier (Perma Pure LIC, NJ) was used to supply water vapor to the OFR.  
154 Tar ball aerosols carried by 1.0 LPM N<sub>2</sub> flow from the atomizer were introduced into OFR. The initial aerosol

155 concentrations in the OFR were mediated by controlling the concentration of the wood tar solution to be atomized  
156 until the number of 350 nm particles was above  $100 \text{ cm}^{-3}$ , as shown in Fig. S1 of tar ball aerosols size distribution  
157 (SI, supporting information). Finally, a total flow of 5.5 LPM with 36~38% RH, initial 27~28 ppm  $\text{O}_3$ , and  
158  $200\sim 250 \mu\text{g m}^{-3}$  tar ball particles (assuming material density of  $1.0 \text{ g cm}^{-3}$ ) was maintained, with a corresponding  
159 plug flow residence time (RT) of 144s for aerosols in the OFR.

160 The extent of simulated daytime oxidation by OH exposure was varied by changing the UV light intensity. Here,  
161 OH exposures in the OFR were inferred by measuring the decay of added  $\text{SO}_2$  (monitored by Thermo  $\text{SO}_2$  analyzer,  
162 model 43i) due to reaction with OH radicals at specific UV lamp intensity. A low concentration ( $\sim 60 \text{ ppb}$ ) of  $\text{SO}_2$   
163 was used to minimize its influence on the OH radical reactivity. Typical total OH exposures ranged from  
164  $(8.7 \pm 2.3) \times 10^{10}$  to  $(8.6 \pm 1.7) \times 10^{11} \text{ molec cm}^{-3} \text{ s}$  or 0.5~7 equivalent daytime atmospheric oxidation days (EAD)  
165 were maintained, taking typical ambient average OH concentration as  $1.5 \times 10^6 \text{ molec cm}^{-3}$  (Kang et al., 2007;  
166 Peng et al., 2015, 2016).

167 In addition to reactions with oxidants, organic aerosols may change their chemical and physical properties by  
168 photolysis (Epstein et al., 2014; Lee et al., 2014; Wong et al., 2014). Therefore, the influence of light irradiation  
169 during tar ball photochemical aging was assessed at the short exposure time in the OFR. Here, tar balls aging was  
170 repeated at the same conditions (e.g., RT, RH,  $\text{N}_2/\text{O}_2$  flow, tar balls concentration, UV lamp power) without  $\text{O}_3$   
171 supply in the OFR. The 254 nm photon flux at specific to maximal UV lamp power was calculated by fitting the  
172 OH exposure estimated from  $\text{SO}_2$  decay and by the Aerodyne OFR Exposure Estimator (v3.1,  
173 <https://sites.google.com/site/pamwiki/hardware/estimation-equations>).

174 Under polluted conditions, nitrogen oxides ( $\text{NO}_x$ ) are often involved in the atmospheric transformations of  
175 organic aerosol and alter their physiochemical properties (Rollins et al., 2012; Ng et al., 2007; Lin et al., 2015).  
176 Therefore,  $\text{NO}_x$  influence on tar ball aerosol aging was also investigated. Due to rapid conversion of  $\text{NO}_x$   
177 ( $\text{NO} + \text{NO}_2$ ) into nitric acid ( $\text{HNO}_3$ ) under high  $\text{O}_3$  and OH concentrations, simple addition of  $\text{NO}_x$  into OFR cannot  
178 sustain  $\text{NO}_x$  levels that compete with  $\text{HO}_2$  radicals in the reaction with organic proxy (ROO).  $\text{NO}_x$  generated via  
179  $\text{N}_2\text{O}$  reaction with  $\text{O}^1\text{D}$  has been modeled and tested to suit the characterization of  $\text{NO}_x$ -dependent SOA formation  
180 pathways using OFR (Peng et al. 2017; Lambe et al., 2017). In this study,  $\text{N}_2\text{O}$  (99.999%) addition of 0.5 vol.%  
181 and 2.0 vol.% were used during tar ball aerosol photochemical oxidation in the OFR, and equivalent OH exposure  
182 of about 4.0 EAD was maintained.  $\text{NO}_x$  ( $\text{NO}$  and  $\text{NO}_2$ ) concentrations downstream of the OFR was measured  
183 using a  $\text{NO}/\text{NO}_2$  analyzer (Ecotech, Serinus 40  $\text{NO}_x$ ). Experimental parameters including initial  $\text{O}_3$  and  $\text{N}_2\text{O}$   
184 concentrations,  $\text{NO}_x$ , moisture ratio, maintained OH exposures and the corresponding photon flux at 254 nm are

185 presented in Table 1.

### 186 **2.3 Online optical and chemical characterization**

187 Prior to the optical and chemical measurements, excess ozone and NO<sub>x</sub> were removed from the sample air stream  
188 following the OFR using two diffusion denuders packed with Carulite (Carus Corporation, Peru, IL) and one  
189 activated charcoal tube. The stream flow was further dehydrated with two silica gel diffusion dryers. Afterward,  
190 the tar ball aerosols were characterized by a combination of on-line chemical and optical instruments.

191 Bulk chemical fragments and organic elemental ratios of tar ball aerosols were monitored in real time by the  
192 HR-ToF-AMS (Aerodyne Research Inc., Billerica, MA, USA) in alternating high sensitivity V and high-resolution  
193 W modes. The working principles of the AMS have been described in details elsewhere (DeCarlo et al., 2006). In  
194 short, aerosol particles are separated from the gas phase through an aerodynamic lens system and then transferred  
195 into the vacuum system, where they are impacted onto a vaporizer at about 600 °C, thus vaporizing the particles.  
196 The analyte vapors are ionized with 70 eV electron impact ionization (EI). A time-of-flight mass spectrometer is  
197 used for high-resolution analysis of the ions. SQUIRREL v1.16 and PIKA v1.57 codes  
198 (<http://cires.colorado.edu/jimenez-group/ToFAMSResources/ToFSoftware/>) were used to process the collected  
199 AMS data. Four ion groups were classified as C<sub>x</sub>H<sub>y</sub><sup>+</sup>, C<sub>x</sub>H<sub>y</sub>O<sup>+</sup>, C<sub>x</sub>H<sub>y</sub>O<sub>z</sub><sup>+</sup> (z>1), and C<sub>x</sub>H<sub>y</sub>O<sub>i</sub>N<sub>p</sub><sup>+</sup> (i≥0, p≥1) based  
200 on fragment features. The ions O<sup>+</sup>, OH<sup>+</sup>, and H<sub>2</sub>O<sup>+</sup> were included in the C<sub>x</sub>H<sub>y</sub>O<sub>z</sub><sup>+</sup> group, as concentrations of these  
201 species were calculated from the organic CO<sub>2</sub><sup>+</sup> ion abundance using the method in Aiken et al (2008). The ambient  
202 improved (AI) atomic ratios of oxygen to carbon (O:C), hydrogen to carbon (H:C), nitrogen to carbon (N:C), and  
203 organic mass to organic carbon (OM/OC) were generated from the measured ion fragments.

204 Particle-bound organic molecules were measured using a custom single-particle time-of-flight mass  
205 spectrometer. This instrument features laser desorption and resonantly enhanced multiphoton ionization (SP-LD-  
206 REMPI-ToF-MS), allowing for the detection of aromatic substances on individual particles. Detailed description  
207 and application of the instrument in LD-REMPI ionization mode is given by Bente et al. (2008) and Passig et al.  
208 (2017). Briefly, aerodynamically accelerated particles are individually sized using laser velocimetry, and heated  
209 by a pulsed CO<sub>2</sub> infrared laser (10.6 μm) to desorb organic molecules. Aromatic substances in the gas plume are  
210 selectively ionized via REMPI by a KrF-excimer laser pulse (248 nm) and detected in the positive MS flight tube.  
211 The REMPI-MS technique is very sensitive and selective for aromatic substances (Boesl et al., 1978; Grotemeyer  
212 et al., 1986; Rettner and Brophy, 1981) and suitable for studies on pyrolysis and (wood) combustion processes  
213 (Heger et al., 1999; Czech et al., 2017). For the tar ball aerosols it provides complementary information to the

214 HR-ToF-AMS spectra. A custom software on LabView basis records and calculates the aerodynamic size and  
215 individual mass spectra of the particles.

216 For optical measurements, tar ball aerosols were size-selected using an Aerosol Aerodynamic Classifier (AAC,  
217 Cambustion, UK). AAC has significant advantages over the commonly used Differential Mobility Analyzer  
218 (DMA) classifier. The AAC classifies particles based on the aerodynamic size without charging and hence it  
219 avoids the contribution of multiply charged particles, thus generating real monodisperse size-selected particles  
220 distribution, reducing the errors associated with multiply charged large particles. In addition, the AAC has higher  
221 particle transmission efficiency at the relevant size range (Tavakoli and Olfert, 2013, 2014). Aerodynamic size-  
222 classified particles after the AAC were further scanned by a scanning mobility particle sizer (SMPS, classifier  
223 Model 3080, DMA Model 3081, CPC model 3775, TSI) to derive their mobility size distribution. The effective  
224 density of tar balls can be estimated from Equation 1 with assumptions of homogeneous composition and particle  
225 shape factor of 1.0, which was verified later in this study:

$$226 \rho_{eff} = \frac{D_{aero}}{D_m} \rho_0 \quad [1]$$

227 Where  $\rho_{eff}$  is an effective density,  $D_{aero}$  and  $D_m$  are aerodynamic and mobility diameters, respectively.  $\rho_0$  is unit  
228 density of 1.0 g cm<sup>-3</sup>.

229 Based on the derived effective density, size-specific tar ball aerosols covering mobility diameters between 175  
230 to 350 nm with an interval of 25 nm were size-selected via AAC, and monodisperse tar balls were introduced into  
231 a dual-channel broad-band cavity enhanced spectrometer (BBCES) for light extinction ( $\alpha_{ext}$ ) measurements in the  
232 wavelength of 360~395 nm and 385~435 nm (at resolution 0.5 nm). A detailed description of the instrument can  
233 be found elsewhere (Washenfelder et al., 2013; Flores et al., 2014a, b). With the combination of a condensation  
234 particle counter (CPC, Model 3575, TSI) to measure particle concentration ( $N$ ) in series, size-specific particle  
235 extinction cross section ( $\sigma_{ext}$ ) can be calculated by Equation (2):

$$236 \sigma_{ext}(\lambda, D_p, RI) = \frac{\alpha_{ext}(\lambda, D_p, RI)}{N(D_p)} \quad [2]$$

237 Where  $\lambda$  is the wavelength of incidence light,  $D_p$  is the particle mobility diameter.

238 Using the Mie-Lorenz scattering theory, the wavelength-dependent complex refractive index of spherical  
239 homogeneous particles was derived (Pettersson et al. 2004; Abo Riziq et al. 2007). The retrieval algorithm was  
240 limited to search for  $n \geq 1$  and  $k \geq 0$  as their physical boundaries. Thereafter, spectral dependent extinction,  
241 scattering, and absorption cross sections ( $\sigma_{ext}$ ,  $\sigma_{sca}$ , and  $\sigma_{abs}$ ) were calculated from the complex RI at specific  
242 particle size. Using these parameters, the single scattering albedo, indicating the scattering fraction of light

243 extinction ( $SSA = \sigma_{sca}/\sigma_{ext}$ ), was calculated.

244 The absorption and extinction Ångström exponents ( $\mathring{A}_{abs}$  and  $\mathring{A}_{ext}$ ) describe the spectral dependence of aerosol  
245 light properties, and are widely used in climate modeling (Russell et al., 2010). It is customary to extrapolate the  
246 optical spectral absorption and extinction fitting to the range of wavelengths using a power law  $\propto \lambda^{-\mathring{A}_{abs}}$  and  $\propto \lambda^{-\mathring{A}_{ext}}$ ,  
247 respectively. In this work, we determined  $\mathring{A}_{ext}$  and  $\mathring{A}_{abs}$  with a linear regression of  $\ln(\sigma_{ext})$  and  $\ln(\sigma_{abs})$  against  
248  $\ln(\lambda)$  over the range of 365 to 425 nm:

$$249 \mathring{A}_{ext} = -\frac{\ln(\sigma_{ext})}{\ln(\lambda)} \quad \mathring{A}_{abs} = -\frac{\ln(\sigma_{abs})}{\ln(\lambda)} \quad [3]$$

250 Here  $\mathring{A}_{ext}$ ,  $\mathring{A}_{abs}$ , and SSA were calculated for tar ball aerosols with a median diameter of 150 nm.

## 251 2.4 Offline optical characterization

252 In addition to the *in-situ* measurements, tar ball particles were also collected quantitatively onto Teflon filters (47  
253 mm diameter, 0.45  $\mu\text{m}$  porosity, Pall Corp.) at sampling flow rate of 2 LPM and then extracted using methanol  
254 (HPLC grade, purity  $\geq 99.9\%$ , Merck) for offline UV-Vis absorption measurement (Cary 60 UV-VIS spectroscopy,  
255 Agilent). Methanol extraction of organic compounds has been commonly performed in various studies (Hoffer et  
256 al., 2006; Laskin et al., 2009; Yee et al., 2013; Finewax et al., 2018; Xie et al., 2017). Here we verified the  
257 completeness of the extraction by extracting each filter twice with methanol. Moreover, vortex shaking (Vortex  
258 Genie-2, Scientific Industries) rather than sonication was applied to avoid chemical degradation of the extracts  
259 upon ultrasonic irradiation (Miljevic et al., 2014; Mutzel et al., 2013). The methanol extractable BrC mass  
260 absorption cross section (MAC,  $\text{m}^2 \text{g}^{-1}$ ) and refractive imaginary  $k$  of the tar balls were estimated based on  
261 following relations (Chen and Bond, 2010; Laskin et al., 2015):

$$262 MAC_{(\lambda)} = \frac{Abs_{(\lambda)} \times \ln(10)}{C \times b} \quad [4]$$

$$263 k_{(\lambda)} = \frac{\lambda \times \rho \times MAC_{(\lambda)}}{4\pi} \quad [5]$$

264  $Abs_{(\lambda)}$  is the base-10 absorbance result from UV-VIS spectroscopy (unitless),  $b$  is the optical length of the solution  
265 (1 cm),  $C$  is the extracted organic carbon mass concentration in solvent ( $\text{g m}^{-3}$ ), which can be determined directly  
266 by normalizing the extract concentration and OC mass fraction for tar balls as OC/OM obtained from AMS data,  
267 as no other refractory elemental carbon (EC) content was detected in our samples (details see in SI).  $\lambda$  is the  
268 incident light wavelength, and  $\rho$  is material density ( $\text{g cm}^{-3}$ ). Here, the derived effective density  $\rho_{eff}$  was used. The  
269 absorption Ångström exponent based on MAC was also derived as  $\mathring{A}_{abs-UV-Vis}$  over the 365-425 nm spectral range.

270 In addition, particles were impacted at a flow of  $2.5 \text{ L min}^{-1}$  onto cyclopore track-etched polycarbonate

271 membrane (47 mm, 0.1 $\mu$ m porosity, Whatman Inc.) to investigate the morphology of tar balls using Scanning  
272 Electronic Microscopy (SEM, JEOL JSM-7000F).

## 273 2.5 Radiative impacts of tar ball aerosols

274 To assess the climatic influence of tar ball aerosols, a wavelength-dependent direct shortwave aerosol simple  
275 radiative forcing efficiency (SRF, W g<sup>-1</sup>) was estimated using the clear sky air mass global horizontal solar  
276 spectrum (AM1GH), assuming that tar ball aerosols form a uniform, optically thin aerosol layer at the lower  
277 troposphere or on ground (Bond and Bergstrom, 2006; Levinson et al., 2010):

$$278 \frac{dSRF}{d\lambda} = -\frac{1}{4} \frac{dS(\lambda)}{d\lambda} \tau_{atm(\lambda)}^2 (1 - F_c) [2(1 - R_{sfc})^2 \beta(\lambda) MSC(\lambda) - 4R_{sfc} \cdot MAC(\lambda)] \quad [6]$$

279 Where  $dS(\lambda)/d\lambda$  is the solar irradiance (photons s<sup>-1</sup> cm<sup>-2</sup>),  $\tau_{atm}$  is the atmospheric transmission (taking 0.79 for  
280 simple calculation),  $F_c$  is the cloud fraction (approximately 0.6),  $R_{sfc}$  is the surface albedo (approximate 0.19 for  
281 urban area ground and 0.8 for snow) (Chen and Bond, 2010),  $\beta$  is the average up-scatter fraction (the fraction of  
282 scattered sunlight that is scattered into the upward hemisphere), and  $MSC(\lambda)$  is wavelength-dependent mass  
283 scattering cross section, respectively. We simply calculated radiative forcing of particles with atmospheric relevant  
284 size of 50 to 500 nm, and SRF was estimated and integrated over the measured range of 365~425nm. The actinic  
285 flux over 365~425 nm was obtained from the “Quick TUV Calculator”, available at  
286 [http://cprm.acom.ucar.edu/Models/TUV/Interactive\\_TUV/](http://cprm.acom.ucar.edu/Models/TUV/Interactive_TUV/) using the following parameters: SZA (solar zenith  
287 angle) of 0 degree, noon time, June 30, 2000, 300 Dobson overhead ozone column, surface albedo of 0.19 for  
288 urban area and 0.8 for snow, and 0 km altitude.

## 289 3 Results and discussion

### 290 3.1 Chemical composition and optical properties of fresh tar ball aerosols

291 Negligible fractions of inorganics (e.g., sulfate, nitrate, chloride, and ammonium) in tar balls are obtained from  
292 AMS measurement as shown in Fig. S2 (SI), and these results confirm again that tar ball aerosols contain  
293 dominated carbonaceous compounds with minor amounts of N, S, and Cl (Pósfai et al., 2004; Hand et al., 2005;  
294 Adachi and Buseck, 2011). Thereafter, only organics in tar balls are considered, and the high-resolution bulk  
295 organic mass spectra for polar and nonpolar tar ball particles are given in Fig. 2. The mass spectra features and  
296 particle effective densities are summarized and compared in Table S1 (SI). Distinct differences in the chemical  
297 composition were observed between polar and nonpolar tar ball aerosols. The alkyl fragments (C<sub>x</sub>H<sub>y</sub><sup>+</sup>, e.g., C<sub>n</sub>H<sub>2n-</sub>  
298 <sub>1</sub><sup>+</sup>, C<sub>n</sub>H<sub>2n+1</sub><sup>+</sup>) dominate the signals for nonpolar particles (accounting for ~56% of total fragments), implying that

the nonpolar tar balls have compositional similarity with common hydrocarbon organic aerosol (HOA). The  $C_xH_yO^+$  fragments are the primary ions for the polar tar balls, contributing ~42% of their mass spectrum, suggesting that most of the organic constituents in the polar tar balls are substantially oxygenated. Both spectra exhibit significant intensity at  $m/z$  28 ( $CO^+$ ),  $m/z$  29 ( $CHO^+$ ), and  $m/z$  43 ( $C_2H_3O^+$ ), indicating the presence of carbonyl ions. The strong signal at  $m/z$  31 ( $CH_3O^+$ ) results from methoxy species that preferably partition into the polar tar fraction. In addition, the significant signals at  $m/z$  50-52 ( $C_4H_2^+$ ,  $C_4H_3^+$ ,  $C_4H_4^+$ ),  $m/z$  65 ( $C_5H_5^+$ ),  $m/z$  77-78 ( $C_6H_5^+$ ,  $C_6H_6^+$ ),  $m/z$  81 ( $C_6H_9^+$ ), and  $m/z$  91 ( $C_7H_7^+$ ), which are characteristic of aromatic compounds, indicate that tar balls, especially from the nonpolar phase, contain a considerable amount of aromatic organics or present high aromaticity. Ion peaks at  $m/z$  77-78, 81, and 91 are typical for monocyclic aromatics such as alkyl-substituted benzene (for  $m/z$  77-78, 91) and heterocyclic aromatics (for  $m/z$  81) (Li et al., 2012). While the relative higher signal at  $m/z$  128 ( $C_{10}H_8^+$ ) in the nonpolar tar ball mass spectra can be assigned to molecular ion of naphthalene (Herring et al., 2015). Moreover, signals at  $m/z$  55 and 57 ( $C_3H_3O^+$ ,  $C_3H_5O^+$ ) are signature fragments of aliphatic and non-acid oxygenated organics that are used to trace cooking emissions (He et al., 2010), and these two fragments were also observed in the tar ball aerosols. Similar to ambient biomass burning emissions,  $C_2H_4O_2^+$  ( $m/z$  60) and  $C_3H_5O_2^+$  ( $m/z$  73), two characteristic fragments from levoglucosan and similar cellulose pyrolyzed species (e.g., mannosan, galactosan) were detected in all the tar ball aerosols, and these fragments were more prominent in the polar aerosols due to the solubility of levoglucosan and analogs in water. Weimer et al. (2008) reported the percentage of  $m/z$  60 and 73 for the burning of various woods to be 0.6-4.1% and 0.1-2.0%, respectively. The percentage of these two fragments in our tar ball aerosols (0.7-1.6% for  $m/z$  60 and 0.5-0.9% for  $m/z$  73) are comparable to the literature data, although the fuel and the pyrolysis procedure are different. The  $m/z$  137 peak is dominated by fragments of  $C_8H_9O_2^+$  and  $C_7H_5O_3^+$ , and these fragments have been determined in biomass burning emissions and were assigned to lignin-related ions with methoxy-phenolic structures (Li et al., 2012; Li et al., 2014). Phenols and methoxy phenols are prominent compounds, accounting for 41% of the identified organic species, in primary BBOA (Schauer et al., 2001). The signal at  $m/z$  137 is much higher in the nonpolar phase tar ball aerosols (1.0% and 0.5% for nonpolar and polar tar balls, respectively), and the fraction of fragment  $m/z$  137 is consistent with reference values of 0.3-2.0% (Li et al., 2012).  $m/z$  44 ( $CO_2^+$ ), a marker fragment of carboxylic acids has been parameterized as  $f_{44}$  (fraction of mass spectrum signal at  $m/z$  44) to present the oxidation degree of organic aerosols (Aiken et al., 2008; Ng et al., 2010). Higher  $f_{44}$  values indicate more oxidized OA (OOA), while less oxidized OA is characterized by lower  $f_{44}$  (Schauer et al., 2001). Peroxides can also produce  $CO_2^+$  signal via extensive fragmentation in the AMS (Aiken et al., 2008).  $f_{44}$  has also been shown

329 to be linearly correlated with the elemental O:C ratio of OA (Aiken et al., 2008). In this study,  $f_{44}$  for the nonpolar  
330 and polar tar ball aerosols are 1.9% and 2.4%, and the corresponding O:C ratios are 0.25 and 0.44. The higher  
331 O:C and H:C ratios explain the polarity of the polar tar ball aerosols. The simplified average carbon oxidation  
332 state ( $\overline{OSc} \approx 2O:C-H:C$ ) describe the oxidation level of particulate complex organic mixtures (Kroll et al., 2011).  
333 The calculated  $\overline{OSc}$  for the tar ball aerosols are -1.05~-0.76, which agrees well with reference values of -1.0~-0.7  
334 for primary BBOA (Kroll et al., 2011). These values are in the broad range of -1.7~-1.6 for HOA and -0.5~0 for  
335 semivolatile OOA (Aiken et al., 2008). In addition, a small fraction of nitrogen-containing organic compounds  
336 (NOC) was detected, with the  $C_xH_yO_iN_p^+$  group contributing 1.6~3.6% of the tar ball mass spectra with estimated  
337 N:C ratio below 0.01, which agrees with previously reported N:C values of 0.008~0.018 for biomass burning  
338 emissions (He et al., 2010). Biomass burning is an important source of NOC in the atmosphere, alkaloid and nitro-  
339 aromatic constituents were detected to be abundant constituents of the NOC (Laskin et al., 2009; Lin et al., 2017).  
340 Nitroaromatic compounds were also identified in urban fire emissions (Bluvshstein et al., 2017; Lin et al., 2017).  
341 Although these compounds constitute a small fraction of the BBOA mass, these chromophoric NOC species  
342 accounted for 50~80% of the total visible light absorption by the extractable BrC (Lin et al., 2017).

343 Fragments larger than 100 amu ( $f_{m/z>100}$ ) contribute a large fraction of the total organic signals for tar ball  
344 aerosols, consistent with biomass burning emissions that contain a large fraction of high-molecular weight  
345 compounds (Ge et al., 2012; Zhou et al., 2017).  $f_{m/z>100}$  is 32% for the nonpolar tar ball aerosols, which is higher  
346 than that of the polar particles (15%), demonstrating that the nonpolar tar balls consists of more high-molecular  
347 weight organics. The measured effective densities for polar and nonpolar tar balls are 1.33 and 1.24 g cm<sup>-3</sup>.  
348 Chemical characteristics from AMS and densities for internal mixture tar balls follow the volume-linear mixing  
349 of polar and nonpolar tar solutions.

350 A considerable aromatic fraction in the tar ball aerosols was confirmed by the LD-REMPI-MS measurement.  
351 Fig. 3 presents the mass spectra of aromatic substances obtained for each one exemplary polar and one nonpolar  
352 particle, respectively. Aerodynamic size distributions for the detected tar ball aerosols are given in Fig. S3, and  
353 substances identified in the mass spectra are listed in Table S2 (SI). The features in the mass spectra are consistent  
354 with the polarity of examined tar ball aerosols and ambient BBOA (Lin et al., 2018). The complex REMPI-  
355 spectrum shows rows of intense unsubstituted and partially alkylated PAH peaks in the nonpolar tar balls,  
356 including naphthalene, acenaphthylene, phenanthrene, pyrene, and in particular, the softwood combustion marker  
357 retene at  $m/z$  234 and some possible derivatives (oxidized-retene at  $m/z$  250 with one oxygen addition, methyl-  
358 retene at  $m/z$  248 with one methyl addition) (McDonald et al., 2000; Shen et al., 2012). Retene and some of the

359 aforementioned PAHs are also observed in the polar tar ball aerosols' mass spectra with lower intensities. In  
360 contrast, the polar tar ball REMPI mass spectra shows strong peaks from oxidized aromatics, more specifically,  
361 benzenediol and methoxy-phenols (e.g., catechol, guaiacol, acetovanillone, syringaldehyde, conifery aldehyde,  
362 etc.). These results are also verified in ambient BBOA, of which the nonpolar BrC consists of primary  
363 unsubstituted PAHs, while the polar fraction includes major aromatic acids and phenols (Lin et al., 2018). The  
364 REMPI mass spectra corresponds to the large fractions of CHO<sup>+</sup> and CH<sub>3</sub>O<sup>+</sup> fragments and high O:C ratios  
365 observed for the polar tar aerosols via HR-ToF-AMS, and keep in consistence with the strong signals of typical  
366 aromatic fragments observed in the nonpolar tar aerosols in Fig. 2. The dominance of aromatic compounds in tar  
367 ball chemical composition agrees well with previous work on BBOA (Schauer et al., 2001; Wei et al., 2015; Bente  
368 et al. 2008, 2009; Czech et al. 2017). Biomass burning is a major source of environmental PAHs (alkylated PAHs,  
369 oxygenated-PAHs, phenols, nitrogen-substituted PAHs, etc.) in both particulate and gaseous phases, and extensive  
370 emissions of PAHs from incomplete combustion pose a great threat to ecosystem and human health due to their  
371 carcinogenic toxicity (Li et al., 2017; Shen et al., 2013; Sigsgaard et al., 2015; Shrivastava et al., 2017). Moreover,  
372 the primary PAHs can act as precursors that substantially contribute to ambient SOA or BrC aerosol when involved  
373 in atmospheric photochemical aging, leading to profound climatic influence (Yee et al., 2013; Yu et al., 2014; Lu  
374 et al., 2011; Zhang et al., 2012 ).

375 The complex refractive index (RI) of tar ball aerosols was retrieved under the assumption that the particles have  
376 similar chemical composition and a spherical shape. The SEM images shown in Fig. S4 (SI) confirm the spherical  
377 morphology and homogeneous composition of the tar ball particles generated in this study. Electron energy-loss  
378 spectroscopy (EELS) spectra indicates that the tar ball particles contain major C and minor O, which fits the AMS  
379 result and previous work (Pósfai et al., 2004; Chakrabarty et al., 2010). Continuous spectral-dependent RI and  
380 SSA for tar balls were derived and are presented in Fig. 4, RI results for tar ball aerosol at mixing ratio of 2:1 and  
381 1:2 are presented in Fig. S5 (SI). Although scattering dominates the light extinction, absorption in the UV and in  
382 the visible ranges was unambiguously identified for the tar ball aerosols, with characteristic absorption similar to  
383 atmospheric BrC and HULIS (Hoffer et al., 2006; Bluvshstein et al., 2017; Lin et al., 2017). The imaginary part,  $k$ ,  
384 increases towards the UV range, presenting 0.02~0.03 difference over the measured spectra range. The real part,  
385  $n$ , for the nonpolar tar balls decreased from 1.673 at 365nm to 1.647 at 425nm, which is almost parallel to the  
386 descending  $n$  for the polar tar balls ranging from 1.651 at 365nm to 1.625 at 425nm.  $k$  is 0.029~0.013 for the  
387 nonpolar tar ball over light wavelength of 365~425nm, while the imaginary part for nonpolar aerosols is 0.007 at  
388 365nm and zero at wavelength longer than 410 nm, indicating that there is no detectable absorption or  $k$  is lower

389 than our detection limit. The [overwhelming imaginary part for the nonpolar tar aerosol agrees with many reports](#)  
390 [that nonpolar or less polar organics have higher absorption compared with the polar BrC in BBOA \(Lin et al.,](#)  
391 [2018; Sengupta et al., 2018\)](#). The [stronger absorption](#) and relative higher scattering abilities, resulting in a lower  
392 SSA compared with the polar tar ball aerosols. The SSA increases towards the visible wavelength from 0.86 at  
393 365nm to 0.90 at 425nm for nonpolar tar ball, and the corresponding values are 0.95 to 1.0 for the polar tar balls.

394 The optical properties of aerosols relate to their chemical composition. Evidently, most of the PAHs identified  
395 in the tar ball aerosols with high intensity have strong absorption between 350 and 450nm ([Samburova et al., 2016;](#)  
396 [Lin et al., 2018\)](#), as shown in [Fig. S6 \(SI\)](#), which coincide the range of tar ball absorption measured here, implying  
397 that PAHs could be a dominate contributor to the absorption of fresh tar balls. Higher imaginary  $k$  can be explained  
398 partly by the larger proportion of PAHs as well as more high-molecular-weight organics present in the nonpolar  
399 tar ball particles, as conjugated aromatic rings and phenols contribute to the major chromophores in the wood  
400 smoke (Laskin et al., 2015; [Lin et al., 2017, 2018\)](#). High-molecular weight organics may resemble HULIS that  
401 can form charge transfer complexes (Phillips and Smith, 2004), that can absorb light at a longer wavelength range.  
402 The result is consistent with the finding that higher molecular weight and aromaticity result in stronger absorption  
403 for atmospheric BrC (Dinar et al., 2008). Moreover, the higher NOC content may also contribute to the  
404 chromophores in the nonpolar tar aerosols ([Lin et al., 2017, 2018\)](#).

405 The average RIs at 375 and 405 nm are  $1.671+0.025i$  and  $1.659+0.017i$  for nonpolar tar ball aerosols. The  
406 corresponding RIs are  $1.647+0.005i$  and  $1.635+0.04i$  for the polar tar ball aerosols. The imaginary part  $k$  retrieved  
407 from the BBCES data, though low, agrees well with  $k$  values calculated from UV-Vis absorption of the bulk  
408 solution. The MAC for the methanol extracted BrC in tar ball aerosol is shown in [Fig. S7 \(SI\)](#). The absorption  
409 may be different for complex materials in the particulate and in the aqueous phases since parameters such as shape  
410 factor, mixing state, together with artifacts from the optical instruments detection and data retrieval methods can  
411 all affect the final optical results, while solvent-dependent extraction/dissolving efficiency of chromophores or  
412 solvent effect (e.g., pH in water solution) may impact the solution absorption coefficient (Huang et al., 2018; Lin  
413 et al., 2017). The light absorption coefficient of particulate BrC has been reported to be 0.7~2.0 times that of bulk  
414 BrC extracts by Liu et al. (2013).

415 The absorption Ångström exponent ( $\hat{A}_{\text{abs}}$ ) is often used to describe the wavelength-dependence of aerosol light  
416 absorption with a value of nearly 1 for BC particles and values substantially larger than 1 indicating the  
417 contribution from BrC (Reid et al., 2005; Chen and Bond, 2010). In this work,  $\hat{A}_{\text{abs}}$  for the nonpolar and polar tar  
418 ball particles ranges from 5.9 to 6.8 between 365 and 425 nm, which is consistent with values of 5.7~7.8 calculated

419 from the bulk absorption in solution. The nonpolar tar balls have a lower  $\hat{A}_{\text{abs}}$ . The difference in  $\hat{A}_{\text{abs}}$  reflects the  
420 different chemical composition of chromophores in the particles, as inferred also from the AMS data. Bluvshstein  
421 et al. (2017) reported relative low values of  $\hat{A}_{\text{ext}}$  (2~3) and  $\hat{A}_{\text{abs}}$  (4~6) over 300~650 nm for ambient fire plume,  
422 which are likely affected by BC in the smoke aerosol and also due to lower wavelength dependence of aerosol  
423 absorption and scattering over the longwave visible range. Overall, the broadband optical results for fresh tar ball  
424 aerosols are consistent with limited discrete measurements of atmospheric BBOA as summarized in Table 2. It  
425 has also been found that the biomass fuel type, combustion conditions, and atmospheric processing eventually  
426 affect the optical properties of BBOA. Lack et al. (2012) modeled core-shell absorption for primary organic matter  
427 (POM) and BC from biomass burning. They found that the imaginary part of the RI and BrC MAC of POM at  
428 404 nm were  $0.007 \pm 0.005$  and  $0.82 \pm 0.43 \text{ m}^2 \text{ g}^{-1}$ , respectively. Charkey et al. (2010) compared the optical  
429 properties of tar balls from smoldering combustion of different biomass. Fuel-dependent imaginary RI for tar ball  
430 at 405 nm was 0.008~0.015 and  $\hat{A}_{\text{abs}}$  over 405~532 nm was 4.2~6.4, which is in line with the  $\hat{A}_{\text{abs}}$  value of 6~7  
431 reported for BBOA derived HULIS (Hoffer et al., 2006). Sedlacek et al. (2018) observed a weak absorption for  
432 wildfire produced tar balls with RI of  $1.56 + 0.02i$ . Sumlin et al. (2018) simulated BrC formation under different  
433 pyrolysis temperatures. The BrC produced from over 300 °C combustion has imaginary part  $k$  of 0.05~0.09 and  
434 real part  $n$  of 1.59~1.68 at 375 nm, and RI at 405 nm is  $1.57 + 0.03i$ , corresponded  $\hat{A}_{\text{abs}}$  over 375~405 nm is 6.4~7.4.

435 Optical mixing rules can be used to estimate or explain the refractive indices of internally mixed substances,  
436 and three mixing rules are commonly applied in climate models: molar refraction of absorption (Jacobson, 2002),  
437 volume-weighted linear average of the refractive indices (d'Almeida et al., 1991), and the Maxwell-Garnett rule  
438 (Chýlek et al., 2000). The “linear mixing rule” and molar refraction mixing rules were tested in this work for  
439 mixtures of tar ball particles against the retrieved optical data. Relevant data analysis details are provided in the  
440 supporting materials (Table S3-S4, [Fig. S8-S12](#)). It was found that both mixing rules can predict the index of  
441 refraction for the polar/nonpolar tar balls, and values calculated based on “linear mixing rule” fit better with the  
442 experimental data. As mentioned above, the real fractions for polar and nonpolar BrC contributing to the  
443 mass/absorption of BBOA are undefined, some investigations report the dynamic polar BrC dominate in mass  
444 loading (50~85%), but contribute less to the absorption in BBOA (less than 40%) (Asa-Awuku et al., 2008;  
445 Bluvshstein et al., 2017; Lin et al., 2017, 2018; Rajput et al., 2014; Sengupta et al., 2018). The “linear mixing rule”  
446 confirmed in this study should be helpful in the mathematical modeling to assess climatic impacts of biomass  
447 burning related BrC aerosol, when their chemical composition is classified.

### 448 3.2 Photooxidation of tar ball particles

449 Aerosols have a wide range of atmospheric lifetimes from hours to days, during which they are involved in various  
450 atmospheric processes, resulting in changes of properties (Reid et al., 2005; Rudich et al., 2007; Jimenez et al.,  
451 2009). Therefore, we studied the effects of photochemical oxidation of the nonpolar wood-pyrolyzed tar ball  
452 aerosols to investigate the physiochemical changes that can occur during tar balls' atmospheric lifetime. [Fig. 5](#)  
453 presents the evolution of the wavelength-dependent RI and SSA as a function of the aerosols' O:C ratio following  
454 NO<sub>x</sub>-free photochemical aging in the OFR. The oxidation covers 0.7-6.7 EAD. Substantial decrease of the RI and  
455 an increase of the SSA are correlated with an increase of the O:C ratio, [these](#) specific parameters are summarized  
456 in Table S5 (SI). Light scattering as well as the absorption by the tar balls aerosol decrease with increasing OH  
457 oxidation. The tar aerosols lose their scattering and absorption significantly up to 3.9 EAD aging. The average RI  
458 decreased from initial  $1.661 \pm 0.020i$  to  $1.632 \pm 0.007i$ , and the corresponding average SSA increased from  
459  $0.89 \pm 0.01$  to  $0.96 \pm 0.02$ . Then, the RI by tar balls persisted with enhanced oxidation, so that the MAC values  
460 remained stable after 3.9 days oxidation ([Fig. S13, SI](#)), suggesting that all the photochemical-labile chromophores  
461 were largely eliminated, while the remaining fraction still presented some light absorption. Forrister et al. (2015)  
462 also observed a stable fraction of biomass burning BrC that had persistent absorption even after long  
463 photochemical evolution time in the ambient environment. They suggested that the remaining persistent fraction  
464 determines the background BrC levels. In our study, the O:C ratio for tar ball aerosols increased continuously with  
465 photochemical oxidation, implying production of oxygenated constituents (carboxylic, carbonyl compounds, etc.),  
466 and the interaction between these increasingly oxidized species coupled with the relative stable intrinsic  
467 chromophoric structures (e.g., fused aromatic rings in [Fig. 3](#)) in some supermolecular structure that may explain  
468 the persistent absorption for aged tar ball aerosols (Dewar and Lepley, 1961; Desyaterik et al., 2013; Samburova  
469 et al., 2016). In addition, a balance between photobleaching of intrinsic chromophores and photochemical  
470 formation of BrC via gas-particle transfer, as well as dynamic gas-particle partitioning of chromophores and  
471 products of their photo-degradation should also be considered in the overall absorption behavior for BBOA during  
472 photochemical processes.

473 The observed photooxidation bleaching is consistent with previous studies on atmospheric processes of BrC.  
474 Sumlin et al. (2017) conducted multiple-day photochemical oxidation on primary biomass burning BrC aerosols  
475 and observed that BrC losses its light absorption and scattering in the near-UV wavelengths by aging. Their  
476 derived RI at 375 nm decreased from  $1.59 \pm 0.03i$  for fresh emission to  $1.50 \pm 0.02i$  after 4.5 EAD oxidation with a

477 corresponding O:C ratio increase from 0.34 to 0.40. Decrease in the overall BBOA absorption and scattering was  
478 also detected *in-situ* following a one day evolution by Adler et al. (2011). They monitored an average RI of  
479  $1.53+0.07i$  and  $1.54+0.04i$  for aerosols dominated by open fire and smoldering emissions, respectively, while the  
480 RI decreased to  $1.49+0.02i$  of the aged aerosols during the following day. Zhong and Jang (2014) reported that  
481 light absorption of wood smoke BrC was modified by the photochemical process, owing to the production of BrC  
482 from SOA formation and loss of BrC from photochemical bleaching of the chromophores. The total MAC for the  
483 BrC eventually decreased by 19~68% within one day of aging. They proposed that bleaching occurred by  
484 excitation of electrons through the absorption of sunlight via  $\pi-\pi^*$  (UV and near UV illumination) or  $n-\pi^*$  (visible  
485 wavelengths irradiation) transitions. Then, the excited electrons disrupted the conjugated structure of  
486 chromophores, leading to the fading of wood smoke color.

487 When tar ball aerosols were illuminated merely by 254 nm UV light at residence time of 144s, photolysis  
488 occurred and weakly diminished their light absorption in line with the extent of photon flux exposure. UV  
489 irradiation similar to the O<sub>3</sub> condition slightly decreased the average RI to  $1.649+0.018i$ , indicating that  
490 photolysis played a minor role in tar ball aerosols bleaching and contributed to less than 15% of imaginary k  
491 changes in NO<sub>x</sub>-free photochemical aging process. Even at full power of UV lamps in the OFR, the average RI  
492 decreased by 0.012 and 0.005i for maximum photolyzed tar balls (Table S6-S7, [Fig. S14-S17, SI](#)). As we also did  
493 not observe detectable optical changes in blank tests upon exposure to O<sub>3</sub> under dark (SI, [Fig. S18-S19](#)), the  
494 bleaching of the tar balls in the OFR is mainly attributed to OH-initiated chromophores decomposition via  
495 heterogeneous reactions, rather than to O<sub>3</sub> oxidation or photolysis.

496 These results indicate a fundamental relationship between photochemical processes and impairment of light  
497 absorbing and scattering abilities in tar ball aerosols. The optical behaviors of tar balls are a consequence of their  
498 chemical composition changes, which are very sensitive to photochemical process, and even one daytime  
499 atmospheric aging resulted in significant oxidation and bleaching of tar balls. In [Fig. 6a](#), the H:C, OM/OC,  $\overline{osc}$ ,  
500 and particle effective density versus O:C ratio are shown. [Fig. 6b](#) presents the contributions of C<sub>x</sub>H<sub>y</sub><sup>+</sup>, C<sub>x</sub>H<sub>y</sub>O<sup>+</sup>,  
501 C<sub>x</sub>H<sub>y</sub>O<sub>z</sub><sup>+</sup>, and C<sub>x</sub>H<sub>y</sub>O<sub>i</sub>N<sub>p</sub><sup>+</sup> groups to the tar balls composition under a range of OH exposure conditions. Mass  
502 spectra features and densities of the tar ball aerosols under various oxidation processes are summarized in Table  
503 S8 (SI). Increasing the OH exposure leads to continuous increase of O:C and H:C ratios, leading to higher  $\overline{osc}$   
504 for the tar ball aerosols. This result is consistent with Sumlin et al. (2017), who reported that the O:C and H:C for  
505 BBOA increased by ~0.08 and ~0.03 after 4.5 EAD photochemical oxidation, respectively. In this work, the  
506 measured O:C ratio increased from 0.25 to 0.38 after maximum aging, while the H:C ratio increased by 0.07 from

507 initial value of 1.55.

508 Other previous studies also depicted dynamic change of elemental ratios for SOA upon aging (Aiken et al.,  
509 2008). The H:C ratio may either increase or decrease, depending on the precursor type and oxidation conditions.  
510 Overall, O:C and H:C ratios changes relate to specific chemical processes or/and to gas-particle mass transfer  
511 during aging of aerosols (Heald et al., 2010; Kim et al., 2014). The tar ball aerosols consist of mostly reduced  
512 species ( $\overline{\delta_{sc}} < 0$ ), which can be oxidized primarily via oxidative formation of polar functional groups to the carbon  
513 skeletons. In OH-initiated oxidation, functionalization includes OH/OOH function group addition and  
514 COOH:Carbonyl groups formation that increase the net oxygen content in SOA (Kroll et al., 2011). Hydration or  
515 polar functional groups addition to unsaturated C-C bonds may also increase the H:C ratio. Moreover,  
516 fragmentation or evaporation also mediate the O:C and H:C ratios of SOA in further aging (Zhang and Seinfeld,  
517 2013; Kim et al., 2014). We attribute the increase in H:C ratio to such oxidation mechanisms that involve bulk  
518 species in the particles. As shown in Table S8 (SI),  $f_{m/z>100}$  decreased monotonically with aging. After 6.7 EAD  
519 photooxidation,  $f_{m/z>100}$  contributed only 21% of the total organic signals. The decrease of  $f_{m/z>100}$  indicates that  
520 fragmentation reactions are involved in the photochemical evolution, and decomposition of high-molecular weight  
521 compounds, thereby, reduced the size of the conjugated molecular system. The persistent high value of  $f_{m/z>100}$   
522 after 6.7 EAD photooxidation imply that some high molecular weight compounds remained in the tar ball aerosols,  
523 and continue to contribute to light absorption either as individual chromophores or as charge transfer complexes.  
524 From Fig. 6b,  $C_xH_y^+$  fragments deplete with OH exposure, while  $C_xH_yO^+$  and  $C_xH_yO_z^+$  fragments increase,  
525 implying the formation of oxygenated moieties in the tar ball aerosols. In addition, a decrease in the  $C_xH_yO_iN_p^+$   
526 fraction was measured from initial 3.6% to 1.9% after the maximum oxidation. Ng et al. (2010) suggested to use  
527  $f_{44}(CO_2^+)$  vs.  $f_{43}(C_2H_3O^+)$  triangle space as indication of OA sources and for estimation of their degree of  
528 oxidation and volatility. The  $C_2H_3O^+$  (less oxidized fragments) is a indicative fragment from aldehydes or ketones.  
529 High  $f_{44}/f_{43}$  ratio indicates low volatility and high oxidation level of SOA. Moreover, high  $f_{44}/f_{43}$  and O:C ratio  
530 are associated with increased hygroscopicity and possible CCN activity of OA (Hennigan et al., 2011; Lambe et  
531 al., 2011). The  $f_{44}$  vs.  $f_{43}$  in this study varied with photochemical aging and fell within the expected range for  
532 ambient OOA, as shown in Fig. 7. Increase of  $f_{44}/f_{43}$  ratio with OH oxidation in Fig. 6b depicted the increase of  
533 carboxylic and/or peroxide compounds compared to carbonyl species in the tar balls, which is consistent with the  
534 atmospheric evolution of ambient biomass burning plumes (Hennigan et al., 2011; Canonaco et al., 2015).

535 To infer the possible chemical processes, detailed mass spectras were compared between fresh and 6.7 EAD  
536 photochemical oxidized tar balls (Fig. S20, SI). We found that decrease of alkyl/alkenyl chains (e.g.,  $C_nH_{2n-1}^+$ ,

537  $C_nH_{2n+1}^+$ ) and aromatic ring structure fragments (e.g.,  $C_6H_5^+$ ,  $C_6H_9^+$ ) contributed the prominent changes in the  
538  $C_xH_y^+$  group, and relative higher  $CO_2^+$  increment relative to  $C_2H_3O^+$  explained the increase in the  $f_{44}/f_{43}$  ratio.  
539 The decrease in the abundance of  $C_2H_4O_2^+$  ( $m/z$  60) and  $C_3H_5O_2^+$  ( $m/z$  73) is consistent with recent studies that  
540 levoglucosan or similar species can decay in the atmosphere due to photochemical oxidation (Hennigan et al.,  
541 2010). The pronounced decrease of intensity at  $m/z$  137 ( $C_8H_9O_2^+$  and  $C_7H_5O_3^+$ ) suggests that the methoxy-phenol  
542 components were dissipated substantially in the aged tar balls .

543 In summary, photochemical oxidation by OH radicals destructed the aromatic rings and methoxy phenolic  
544 structures, which are expected to be the primary chromophores in the tar balls. The NOC content and high-  
545 molecular weight species were also depleted via OH oxidation. These chemical changes upon OH oxidation may  
546 explain the observed diminishing in light scattering and absorption upon photochemical aging.

### 547 3.3 NO<sub>x</sub>-dependent tar ball particles oxidation

548 N<sub>2</sub>O was recently introduced for simulating NO<sub>x</sub>-dependent SOA formation pathways in OFR under high O<sub>3</sub>  
549 concentration, as O(<sup>1</sup>D)+N<sub>2</sub>O reactions can be applied to systematically vary the branching ratio of the RO<sub>2</sub>+NO  
550 reactions relative to the RO<sub>2</sub>+HO<sub>2</sub> and/or RO<sub>2</sub>+RO<sub>2</sub> reactions over a range of conditions relevant to atmospheric  
551 SOA formation (Lambe et al., 2017). Here we introduced 0.5 and 2.0 vol.% N<sub>2</sub>O to investigate NO<sub>x</sub>-involved  
552 daytime aging of tar ball aerosols in the OFR. The OH exposures were maintained for all these tests at about 4  
553 EAD. The corresponded NO<sub>2</sub> concentrations downstream of the OFR was measured to be 96.1±1.3 and 528.3±6.2  
554 ppbv. The concentration of static NO can be neglected under these severe oxidation conditions. Fig. 8 shows the  
555 mass spectra features for fresh and aged tar balls reacted in the absence/presence of NO<sub>x</sub>. Parameters including  
556 organic elemental ratios and densities are summarized in Table S8 (SI). In general, tar balls oxidized under N<sub>2</sub>O  
557 addition exhibit higher O:C and relative lower H:C ratios. NO<sub>y</sub><sup>+</sup> (NO<sup>+</sup> and NO<sub>2</sub><sup>+</sup>) signals appear in the mass spectra  
558 and the intensities of NO<sub>y</sub><sup>+</sup> display a positive trend with N<sub>2</sub>O concentration, together with an increase of  
559 oxygenated fragments ( $C_xH_yO^+$  and  $C_xH_yO_z^+$ ) and decrease of hydrocarbon fragments ( $C_xH_y^+$ ). The signal ratio of  
560 NO<sup>+</sup> ( $m/z$  30) to NO<sub>2</sub><sup>+</sup> ( $m/z$  46) is used to distinguish organic nitrate from inorganic nitrate. The signal from  
561 standard inorganic nitrate (e.g., NH<sub>4</sub>NO<sub>3</sub>) has a typical NO<sub>2</sub><sup>+</sup>/NO<sup>+</sup> ratio of 0.485 obtained from our AMS data  
562 (detailed mass spectra is shown in Fig. S21, SI). The ratio and standard mass spectra are similar to previous studies  
563 (Zhou et al., 2017). The fraction of NO<sub>y</sub><sup>+</sup> (NO<sup>+</sup> and NO<sub>2</sub><sup>+</sup>) signals in the aged tar balls increased from 0% to 0.7%  
564 and 1.5% at 0.5 vol.% and 2.0 vol.% N<sub>2</sub>O additions, respectively. The corresponding values of NO<sub>2</sub><sup>+</sup>/NO<sup>+</sup> ratio  
565 are 0.162 and 0.174, which are much lower than that for inorganic nitrates. Furthermore, the contribution of

566  $C_xH_yO_iN_p^+$  fragments increased from 1.9% to 4.4% and 4.5% over the course of aging. Therefore, we can conclude  
567 that NOC rather than inorganic nitrate formed in the  $NO_x$ -dependent photooxidation process, resulting in an  
568 overall increase of N:C ratio from 0.010 to 0.012 and 0.015. Additionally, the density of tar balls slightly increased  
569 from 1.24 for the fresh tar balls to 1.26 for the one aged in presence of 2 vol.%  $N_2O$ .

570 Detailed changes in the mass spectra over the course of the experiment are shown in Fig. S22 (SI). Indicative  
571 ions of cyclolakyl fragments (e.g.,  $C_2H_3^+$ ,  $C_3H_5^+$ ,  $C_4H_7^+$ ) decreased, while  $NO_x$  addition increased the  $CO^+$  and  
572  $CO_2^+$  intensities relative to  $C_2H_3O^+$ , leading to higher  $f_{44}/f_{43}$  ratio. Ng et al. (2007) observed a similar change for  
573 photooxidation of terpenes in presence of  $NO_x$ . Changes in AMS spectra with  $NO_x$  addition may mark differences  
574 between the dominating reaction pathways in tar ball photooxidation as  $RO_2+NO$  versus  $RO_2+HO_2$  and/or  
575  $RO_2+RO_2$  reactions.

576 Photochemical oxidation with  $NO_x$  addition enhances the oxidation level and increases both the absorption and  
577 scattering of tar ball aerosols. Dynamic changes of the complex RI are shown in Fig. 9 and summarized in Table  
578 S5 (SI). The RI of tar ball aerosols increased from an average of  $1.632+0.007i$  for pure OH-initiated  
579 photooxidation to  $1.635+0.015i$  with the addition of 0.5 vol.%  $N_2O$ , and a greater increase up to  $1.648+0.019i$   
580 with 2.0 vol.%  $N_2O$ . The increase of RI is therefore primarily attributed to NOC formation. Zhong and Jang (2014)  
581 observed that higher  $NO_x$  level slowed photo-bleaching of wood smoke BrC, and they suggested that  $NO_x$ -  
582 modified reaction pathways produce secondary NOC chromophores (i.e., nitro-phenols). Liu et al. (2016)  
583 simulated daytime chemistry of various VOCs in the presence of  $NO_x$  and found that light absorption of produced  
584 SOA, especially aromatic ones, increased with  $NO_x$  concentration. These findings were also corroborated by  
585 experimental study of Lin et al. (2015), where the chemical composition and the light absorption properties of  
586 laboratory generated toluene SOA were reported to have strong positive dependence on the presence of nitro-  
587 phenols formed at high  $NO_x$  oxidation conditions. The color of the BrC diminished with photolysis, correlated  
588 with a decline of the NOC fraction. Nitration of aromatic species via  $NO_x/N_2O_5/NO_3$  has been proposed as one  
589 of the main mechanisms to produce secondary BrC in the atmosphere (Lu et al., 2011; Lin et al., 2015, 2017;  
590 Bluvshstein et al., 2017).

591 The imaginary part at 2.0 vol. %  $N_2O$  addition was almost comparable with that of the fresh tar ball aerosols  
592 (average value:  $RI=1.661+0.020i$ ), although the real part was lower, suggesting that photooxidation in the  
593 presence of  $NO_x$  promote the formation of N-containing chromophores via secondary processes. In our  
594 experiments, formation of the N-containing chromophores outweighed the bleaching from OH photooxidation  
595 to eventually regain the absorption of the aged tar balls. The average SSA calculated for 150 nm particles

596 decreased from 0.96 to 0.91 and 0.89 with N<sub>2</sub>O addition. Absorption enhancement with N<sub>2</sub>O addition for tar balls  
597 upon photooxidation can also be seen in the MAC changes shown in [Fig. S23 \(SI\)](#), where MAC at 375 nm for  
598 fresh tar ball was 0.854 m<sup>2</sup> g<sup>-1</sup>, it decreased to 0.416 m<sup>2</sup> g<sup>-1</sup> via OH photo-bleaching, then MAC increased to 0.459  
599 m<sup>2</sup> g<sup>-1</sup> at 0.5 vol.% N<sub>2</sub>O addition, and up to 0.598 m<sup>2</sup> g<sup>-1</sup> at 2.0 vol.% N<sub>2</sub>O addition due to chromophores formation.

### 600 **3.4 Atmospheric and Climate implication**

601 Atmospheric aging alters the RI of SOA, and the dynamic changes of RI depend on complicated reaction pathways  
602 (Liu et al., 2016). OH-initiated photochemical oxidation and photolysis decrease the RI of laboratory proxies of  
603 tar balls under NO<sub>x</sub>-free condition, while photooxidation under high NO<sub>x</sub> has an opposite effect on the RI of tar  
604 balls. We investigated the relationship between the dynamic RI values of tar ball particles and their possible  
605 climatic implications, including the change of light extinction/absorption efficiency and the clear-sky direct  
606 radiative forcing. For clarity, light extinction/absorption efficiencies were calculated and compared at wavelength  
607 of 375 and 405 nm, while radiative forcing was estimated over all the measured wavelengths from 365 to 425 nm.  
608 Atmospheric and climatic implications were assessed for fresh and oxidized tar ball upon NO<sub>x</sub>-dependent ~3.9  
609 [EAD](#) photooxidation (O\_3.9, N\_0.5, and N\_2.0), in which fresh tar balls were taken as reference.

610 As shown in [Fig. 10](#), photochemical oxidation under NO<sub>x</sub>-free condition (O\_3.9) diminished light extinction  
611 and absorption efficiency of tar ball aerosols in the atmospheric relevant size of 50-300 nm, causing about 5~40%  
612 decrease in extinction at 375 and 405 nm wavelength. For aerosols larger than 400 nm, the extinction efficiency  
613 of tar ball aerosols increased instead after photochemical aging. The light extinction efficiency presented higher  
614 size-dependence than absorption, and extinction changes were more sensitive to particle size, especially in the  
615 smaller sizes. The decreased absorption was more pronounced with ~60% decrease at 375 nm and over 75% at  
616 405 nm. Previous studies have confirmed the relationship between biomass burning emissions and acute regional  
617 visibility deterioration (Huang et al., 2012; Chen et al., 2017). Our results demonstrate that OH radical initiated  
618 daytime aging may play an important role in improving visibility degradation caused by primary biomass BrC.  
619 However, photochemical evolution under high NO<sub>x</sub> conditions may compensate effects of the photooxidation  
620 bleaching of tar ball aerosols via the formation of NOC chromophores. At N\_0.5 conditions, the light extinction  
621 decreased by 4 to 20% at 375 nm and 5 to 24% at 405 nm, respectively. The corresponding absorption decrease  
622 was 20~27% at both wavelengths. With more N<sub>2</sub>O addition, formation of secondary N-containing chromophores  
623 almost completely offsets light extinction/absorption decrease caused by photooxidation. Under the N\_2.0  
624 conditions, enhancement of light absorption efficiency for tar ball was about 0~9% at 405 nm in the entire size

625 range of 50-500 nm.

626 Radiative forcing from aerosols over both ground and snow is vital to climate models (Barnett et al., 2005;  
627 Kanakidou et al., 2005). Integrated radiative forcing for tar ball aerosols as a function of particle size under various  
628 oxidation conditions is shown in [Fig. 11](#). Size-/wavelength-resolved SRF are also shown in [Fig. S24](#) and [S25 \(SI\)](#).  
629 Integrated SRF over ground has negative values for tar balls over almost all the atmospheric relevant sizes,  
630 indicating a radiative cooling effect by tar ball aerosols except at 195~210 nm, where fresh tar ball particles present  
631 warming effect with SRF up to  $\sim 0.48 \text{ W g}^{-1}$ . In practical fire emissions, the size of tar balls depends on the burning  
632 and environment conditions and biomass fuel types with typical values between tens to hundreds of nanometers  
633 (Reid et al., 2005; Pósfai et al., 2004). The complicated size-dependence character of SRF makes it difficult to  
634 assess the real climatic effect of tar ball particles without extensive calculations. [Fig. 11a](#) suggests fresh tar balls  
635 have SRF values of  $-7.46 \text{ W g}^{-1}$  at 150 nm and  $0.45 \text{ W g}^{-1}$  at 200 nm, respectively. The SRF decreased for all size  
636 ranges due to photochemical oxidation to  $-7.93 \text{ W g}^{-1}$  at 150 nm and  $-1.37 \text{ W g}^{-1}$  at 200 nm for tar ball aerosols  
637 under O<sub>3.9</sub> condition. At N<sub>0.5</sub> conditions, SRF was  $-7.37 \text{ W g}^{-1}$  at 150 nm and  $0.16 \text{ W g}^{-1}$  at 200 nm, and the  
638 corresponding values at N<sub>2.0</sub> conditions increased to  $-7.20 \text{ W g}^{-1}$  at 150 nm and  $0.31 \text{ W g}^{-1}$  at 200 nm.

639 In contrast, tar ball particles contributed to positive forcing (warming effect) over the bright terrain throughout  
640 the atmospheric aging, as shown in [Fig. 11b](#). Radiative forcing over the snow showed a simple increasing trend  
641 with particle size, indicating that larger BrC aerosol with identical mass loading in the air have a higher warming  
642 effect. The changes of snow-based radiative forcing upon photochemical aging followed the same trends as in the  
643 ground-based cases. Fresh tar ball at size of 200 nm has SRF of  $20.12 \text{ W g}^{-1}$  over the incident solar wavelength of  
644 365~425 nm on the snow terrain. With photochemical oxidation under NO<sub>x</sub>-free condition, radiative forcing  
645 decreased significantly. After 3.9 EAD atmospheric aging, snow-based radiative forcing for tar ball decreased by  
646 65~73% over the size range of 50~500 nm, the value of 200 nm tar ball became  $6.99 \text{ W g}^{-1}$ . When NO<sub>x</sub> was  
647 involved in the photochemical oxidation of tar balls, the decrement of radiative forcing was weakened. At N<sub>0.5</sub>,  
648 SRF for 200 nm tar ball was  $14.01 \text{ W g}^{-1}$ , while at N<sub>2.0</sub> condition, size-dependent SRF from the aged tar ball  
649 was almost comparable with that from fresh tar ball, and SRF for 200 nm tar ball was  $18.56 \text{ W g}^{-1}$ .

650 Although less than 10% of the solar spectrum's energy is distributed between 365 and 425 nm, the radiative  
651 forcing over this range represents a significant warming or cooling potential over the arctic terrain. In conclusion,  
652 photochemical oxidation under NO<sub>x</sub>-free conditions can decrease radiative forcing of tar ball aerosols, resulting  
653 in enhancement in the cooling effect over ground and decreased in warming effect over the snow. However, NO<sub>x</sub>  
654 involvement in photooxidation inhibits the decrease in radiative forcing of tar ball aerosols. Overall, the complex

655 changes in optical properties of tar balls at long aging times impose great uncertainties in traditional model-based  
656 estimation of BBOA. Our study emphasizes the importance of taking this atmospheric process into consideration  
657 to refine the understanding of the climatic and atmospheric influences from these aerosols.

#### 658 **4 Conclusions**

659 In this study, proxies for tar ball aerosols were generated in the laboratory following a flameless wood pyrolysis  
660 process. The optical and chemical properties of the generated tar balls were constrained using BBCES and HR-  
661 Tof-AMS/SP-LD-REMPI-MS and were shown to have many similarities to ambient biomass burning aerosols.  
662 Laboratory generated fresh tar ball aerosols have light absorption characteristics similar to atmospheric BrC with  
663 higher absorption efficiency towards the UV. The average complex refractive indices between 365 and 425 nm  
664 are  $1.661+0.020i$  and  $1.635+0.003i$  for nonpolar and polar tar ball aerosols, respectively.

665 Atmospheric evolution for tar ball aerosols was experimentally simulated using an oxidation flow reactor. The  
666 study focused on dynamic changes in the optical and chemical properties due to NO<sub>x</sub>-dependent photochemical  
667 oxidation. Furthermore, the relationship between oxidation level and the resulting RI of the tar ball aerosols was  
668 explored. We found a substantial decrease in the scattering and absorption properties of tar balls, with a  
669 corresponding increase in SSA with OH oxidation in the absence of NO<sub>x</sub>. A correlation between the RI decrease  
670 and increase in the O:C and H:C ratios was observed. The decrease in light scattering and absorption is attributed  
671 to the destruction of aromatic/phenolic/NOC and high-molecular weight species chromophores via OH-initiated  
672 photooxidation of tar balls. Over longer aging times, the average RI of the tar ball aerosols decreased from  
673  $1.661+0.020i$  to  $1.632+0.007i$  upon atmospheric equivalent to 3.9 days aging, and the corresponding O:C and H:C  
674 ratio increased from initial 0.25 and 1.55 to 0.35 and 1.59, respectively.

675 Our results suggest that OH oxidation rather than photolysis or ozone reactions plays the dominate role that  
676 determine the optical and chemical properties in tar balls aging. The observed decrease in absorption results from  
677 depletion of chromophores such as aromatic rings, phenolic compounds and high molecular weights species.

678 Simulations under high NO<sub>x</sub> environment enhanced the aerosol oxidation state and increased the scattering and  
679 absorption of tar ball aerosols relative to OH photooxidation in the absence of NO<sub>x</sub>. At ~3.9 EAD, addition of 0.5  
680 and 2.0 vol.% N<sub>2</sub>O increased the organic elemental ratios (O:C, H:C, and N:C ratios) and doubled the organic  
681 nitrates fraction in the particles from 1.9 % to ~4.4 %. The formation of NOC chromophores overweigh the  
682 intrinsic depletion of chromophores, leading to higher RI of  $1.635+0.015i$  and  $1.648+0.019i$ .

683 The atmospheric and climatic implications from tar ball aerosols under various oxidation conditions were

684 assessed using a simple radiative forcing model in terms of extinction/absorption efficiency changes and ground-  
685 /snow-based radiative forcing. These results demonstrate that the optical and chemical properties of tar ball  
686 particles are dynamically related to atmospheric aging, and optical changes are governed by both photobleaching  
687 and secondary chromophores formation. Therefore, the atmospheric process should be emphasized in model  
688 predictions for evaluating biomass burning BrC aerosol radiative forcing as well as climate change.

689

## 690 **Acknowledgments**

691 This research was partially supported by research grants from the US-Israel Binational Science Foundation (BSF)  
692 grant no. 2016093 and Israel Ministry of Science, Maimonide program. Dr. Li acknowledges support from the  
693 Planning & Budgeting Committee, Israel (2018/19). J. Schade, J. Passig and R. Zimmermann gratefully  
694 acknowledge financial support from the German Research Foundation, project number ZI 764/6-1, and Photonion  
695 GmbH, Schwerin, Germany.

696 **Reference**

697 Abo Riziq, A., Erlick, C., Dinar, E., and Rudich, Y.: Optical properties of absorbing and non-absorbing aerosols  
698 retrieved by cavity ring down (CRD) spectroscopy, *Atmos. Chem. Phys.*, 7, 1523-1536, doi:10.5194/acp-7-1523-  
699 2007, 2007.

700 [Adachi, K., and Buseck, P. R.: Atmospheric tar balls from biomass burning in Mexico, \*J. Geophys. Res. Atmos.\*,](#)  
701 [116, D05204, doi:10.1029/2010/2010JD015102, 2011.](#)

702 Adler, G., Riziq, A. A., Erlick, C., and Rudich, Y.: Effect of intrinsic organic carbon on the optical properties of  
703 fresh diesel soot, *Proc. Natl. Acad. Sci. USA*, 107, 6699-6704, doi:10.1073/pnas.0903311106, 2010.

704 Adler, G., Flores, J. M., Abo Riziq, A., Borrmann, S., and Rudich, Y.: Chemical, physical, and optical evolution  
705 of biomass burning aerosols: a case study, *Atmos. Chem. Phys.*, 11, 1491-1503, doi:10.5194/acp-11-1491-2011,  
706 2011.

707 Aiken, A. C., Decarlo, P. F., Kroll, J. H., Worsnop, D. R., Huffman, J. A., Docherty, K. S., Ulbrich, I. M., Mohr,  
708 C., Kimmel, J. R., and Sueper, D.: O/C and OM/OC ratios of primary, secondary, and ambient organic aerosols  
709 with high-resolution time-of-flight aerosol mass spectrometry, *Environ. Sci. Technol.*, 42, 4478-4485,  
710 doi: 10.1021/es703009q, 2008.

711 Alexander, D. T., Crozier, P. A., and Anderson, J. R.: Brown carbon spheres in East Asian outflow and their optical  
712 properties, *Science*, 321, 833-836, doi: 10.1126/science.1155296, 2008.

713 Andreae, M. O. and Gelencsér, A.: Black carbon or brown carbon? The nature of light-absorbing carbonaceous  
714 aerosols, *Atmos. Chem. Phys.*, 6, 3131-3148, doi:10.5194/acp-6-3131-2006, 2006.

715 [Asa-Awuku, A., Sullivan, A., Hennigan, C., Weber, R., and Nenes, A.: Investigation of molar volume and](#)  
716 [surfactant characteristics of water-soluble organic compounds in biomass burning aerosol, \*Atmos. Chem.\*](#)  
717 [Phys.](#), 8, 799-812, doi:10.5194/acp-8-799-2008, 2008.

718 Bahadur, R., Praveen, P. S., Xu, Y., and Ramanathan, V.: Solar absorption by elemental and brown carbon  
719 determined from spectral observations, *Proc. Natl. Acad. Sci. USA*, 201205910, doi:10.1073/pnas.1205910109,  
720 2012.

721 Barnett, T. P., Adam, J. C., and Lettenmaier, D. P.: Potential impacts of a warming climate on water availability  
722 in snow-dominated regions, *Nature*, 438, 303-309, doi:10.1038/nature04141, 2005.

723 Bente, M., Sklorz, M., Streibel, T., and Zimmermann, R.: Online laser desorption-multiphoton postionization mass  
724 spectrometry of individual aerosol particles: molecular source indicators for particles emitted from different  
725 traffic-related and wood combustion sources, *Anal. Chem.*, 80, 8991-9004, doi:10.1021/ac801295f, 2008.

726 Bente, M., Sklorz, M., Streibel, T., and Zimmermann, R.: Thermal desorption-multiphoton ionization time-of-  
727 flight mass spectrometry of individual aerosol particles: A simplified approach for online single-particle analysis  
728 of Polycyclic Aromatic Hydrocarbons and their derivatives, *Anal. Chem.*, 81, 2525-2536, doi:10.1021/ac802296f,  
729 2009.

730 Bluvshstein, N., Lin, P., Flores, J. M., Segev, L., Mazar, Y., Tas, E., Snider, G., Weagle, C., Brown, S. S., and  
731 Laskin, A.: Broadband optical properties of biomass-burning aerosol and identification of brown carbon  
732 chromophores, *J. Geophys. Res. Atmos.* 122, 5441-5456, doi:10.1002/2016JD026230, 2017.

733 Boesl, U., Neusser, H., and Schlag, E.: Two-photon ionization of polyatomic molecules in a mass spectrometer,  
734 *Zeitschrift für Naturforschung A*, 33, 1546-1548, doi:10.1515/zna-1978-1218, 1978.

735 Bond, T. C., and Bergstrom, R. W.: Light absorption by carbonaceous particles: An investigative review, *Aerosol*  
736 *Sci. Tech.*, 40, 27-67, doi:10.1080/02786820500421521, 2006.

737 Canonaco, F., Slowik, J., Baltensperger, U., and Prévôt, A.: Seasonal differences in oxygenated organic aerosol  
738 composition: implications for emissions sources and factor analysis, *Atmos. Chem. Phys.*, 15, 6993-7002,  
739 doi:10.5194/acp-15-6993-2015, 2015.

740 Chakrabarty, R., Moosmüller, H., Chen, L. W., Lewis, K., Arnott, W., Mazzoleni, C., Dubey, M., Wold, C., Hao,  
741 W., and Kreidenweis, S.: Brown carbon in tar balls from smoldering biomass combustion, *Atmos. Chem. Phys.*,  
742 10, 6363-6370, doi:10.5194/acp-10-6363-2010, 2010.

743 Chen, Y., and Bond, T.: Light absorption by organic carbon from wood combustion, *Atmos. Chem. Phys.*, 10,  
744 1773-1787, doi:10.5194/acp-10-1773-2010, 2010.

745 Chen, J., Li, C., Ristovski, Z., Milic, A., Gu, Y., Islam, M. S., Wang, S., Hao, J., Zhang, H., and He, C.: A review  
746 of biomass burning: Emissions and impacts on air quality, health and climate in China, *Sci. Total Environ.*, 579,  
747 1000-1034, doi:10.1016/j.scitotenv.2016.11.025, 2017.

748 [Chung, C. E., V. Ramanathan, and D. Decremet: Observationally constrained estimates of carbonaceous aerosol](#)  
749 [radiative forcing, \*P. Natl. Acad. Sci. USA.\*, 109\(29\), 11624-11629, doi:10.1073/pnas.1203707109, 2012.](#)

750 Chýlek, P., Videen, G., Geldart, D., Dobbie, J. S., and Tso, H.: Effective medium approximations for  
751 heterogeneous particles, *Light scattering by nonspherical particles: theory, measurements, and applications*, pp.  
752 273–308, edited by: Mishchenko, M. I., Hovenier, J. W., and Travis, L. D., Academic Press, 2000.

753 Czech, H., Pieber, S. M., Tiitta, P., Sippula, O., Kortelainen, M., Lamberg, H., Grigonyte, J., Streibel, T., Prévôt,  
754 A. S., and Jokiniemi, J.: Time-resolved analysis of primary volatile emissions and secondary aerosol formation  
755 potential from a small-scale pellet boiler, *Atmos. Environ.*, 158, 236-245, doi:10.1016/j.atmosenv.2017.03.040,  
756 2017.

757 d'Almeida, G. A., Koepke, P., and Shettle, E. P.: Atmospheric aerosols: global climatology and radiative  
758 characteristics, A. Deepak Publishing, Hampton, Va, 1991.

759 DeCarlo, P. F., Kimmel, J. R., Trimborn, A., Northway, M. J., Jayne, J. T., Aiken, A. C., Gonin, M., Fuhrer, K.,  
760 Horvath, T., and Docherty, K. S.: Field-deployable, high-resolution, time-of-flight aerosol mass spectrometer,  
761 *Anal. Chem.*, 78, 8281-8289, doi:10.1021/ac061249n, 2006.

762 Desyaterik, Y., Sun, Y., Shen, X., Lee, T., Wang, X., Wang, T., and Collett, J. L.: Speciation of “brown” carbon in  
763 cloud water impacted by agricultural biomass burning in eastern China, *J. Geophys. Res. Atmos.*, 118, 7389-7399,  
764 doi:10.1002/jgrd.50561, 2013.

765 Dewar, M. J., and Lepley, A. R.:  $\pi$ -Complexes. I. Charge Transfer Spectra of  $\pi$ -Complexes Formed by  
766 Trinitrobenzene with Polycyclic Aromatic Compounds, *J. Am. Chem. Soc.*, 83, 4560-4563, 1961.

767 Dinar, E., Riziq, A. A., Spindler, C., Erlick, C., Kiss, G., and Rudich, Y.: The complex refractive index of  
768 atmospheric and model humic-like substances (HULIS) retrieved by a cavity ring down aerosol spectrometer  
769 (CRD-AS), *Faraday Discuss.*, 137, 279-295, doi:10.1039/B703111D, 2008.

770 Epstein, S. A., Blair, S. L., and Nizkorodov, S. A.: Direct photolysis of  $\alpha$ -pinene ozonolysis secondary organic  
771 aerosol: effect on particle mass and peroxide content, *Environ. Sci. Technol.*, 48, 11251-11258,  
772 doi:10.1021/es502350u, 2014.

773 Feng, Y., Ramanathan, V., and Kotamarthi, V.: Brown carbon: a significant atmospheric absorber of solar  
774 radiation?, *Atmos. Chem. Phys.*, 13, 8607-8621, doi:10.5194/acp-13-8607-2013, 2013.

775 Finewax, Z., de Gouw, J. A., and Ziemann, P. J.: Identification and quantification of 4-Nitrocatechol formed from  
776 OH and NO<sub>3</sub> radical-initiated reactions of catechol in air in the presence of NO<sub>x</sub>: Implications for secondary  
777 organic aerosol formation from biomass burning, *Environ. Sci. Technol.*, 52, 1981-1989,  
778 doi:10.1021/acs.est.7b05864, 2018.

779 Flores, J., Zhao, D., Segev, L., Schlag, P., Kiendler-Scharr, A., Fuchs, H., Watne, Å., Bluvshstein, N., Mentel, T.  
780 F., and Hallquist, M.: Evolution of the complex refractive index in the UV spectral region in ageing secondary  
781 organic aerosol, *Atmos. Chem. Phys.*, 14, 5793-5806, doi:10.5194/acp-14-5793-2014, 2014a.

782 Flores, J. M., Washenfelder, R., Adler, G., Lee, H., Segev, L., Laskin, J., Laskin, A., Nizkorodov, S., Brown, S.,  
783 and Rudich, Y.: Complex refractive indices in the near-ultraviolet spectral region of biogenic secondary organic  
784 aerosol aged with ammonia, *Phys. Chem. Chem. Phys.*, 16, 10629-10642, doi:10.1039/C4CP01009D, 2014b.

785 Flowers, B., Dubey, M., Mazzoleni, C., Stone, E., Schauer, J., Kim, S. W., and Yoon, S.: Optical-chemical-  
786 microphysical relationships and closure studies for mixed carbonaceous aerosols observed at Jeju Island; 3-laser  
787 photoacoustic spectrometer, particle sizing, and filter analysis, *Atmos. Chem. Phys.*, 10, 10387-10398,  
788 doi:10.5194/acp-10-10387-2010, 2010.

789 Forrister, H., Liu, J., Scheuer, E., Dibb, J., Ziemba, L., Thornhill, K. L., Anderson, B., Diskin, G., Perring, A. E.,  
790 and Schwarz, J. P.: Evolution of brown carbon in wildfire plumes, *Geophys. Res. Lett.*, 42, 4623-4630,  
791 doi:10.1002/2015GL063897, 2015.

792 Forster, P. M. F., and Taylor, K. E.: Climate forcings and climate sensitivities diagnosed from coupled climate  
793 model integrations, *J. Clim.*, 19, 6181-6194, doi:10.1175/JCLI3974.1\_2006.

794 Fu, H., Zhang, M., Li, W., Chen, J., Wang, L., Quan, X., and Wang, W.: Morphology, composition and mixing  
795 state of individual carbonaceous aerosol in urban Shanghai, *Atmos. Chem. Phys.*, 12, 693-707, doi:10.5194/acp-  
796 12-693-2012, 2012.

797 Ge, X., Setyan, A., Sun, Y., and Zhang, Q.: Primary and secondary organic aerosols in Fresno, California during  
798 wintertime: Results from high resolution aerosol mass spectrometry, *J. Geophys. Res. Atmos.*, 117, D19301,  
799 doi:10.1029/2012JD018026, 2012.

800 Grottemeyer, J., Boesl, U., Walter, K., and Schlag, E. W.: A general soft ionization method for mass spectrometry:  
801 Resonance-enhanced multi-photon ionization of biomolecules, *Org. Mass. Spectrom.*, 21, 645-653,  
802 doi:10.1002/oms.1210211008, 1986.

803 Hand, J. L., Malm, W., Laskin, A., Day, D., Lee, T. B., Wang, C., Carrico, C., Carrillo, J., Cowin, J. P., and Collett,  
804 J.: Optical, physical, and chemical properties of tar balls observed during the Yosemite Aerosol Characterization  
805 Study, *J. Geophys. Res. Atmos.*, 110, D21210, doi:10.1029/2004JD005728, 2005.

806 He, L. Y., Lin, Y., Huang, X. F., Guo, S., Xue, L., Su, Q., Hu, M., Luan, S. J., and Zhang, Y. H.: Characterization  
807 of high-resolution aerosol mass spectra of primary organic aerosol emissions from Chinese cooking and biomass  
808 burning, *Atmos. Chem. Phys.*, 10, 11535-11543, doi:10.5194/acp-10-11535-2010, 2010.

809 Heald, C., Kroll, J., Jimenez, J., Docherty, K., DeCarlo, P., Aiken, A., Chen, Q., Martin, S., Farmer, D., and Artaxo,  
810 P.: A simplified description of the evolution of organic aerosol composition in the atmosphere, *Geophys. Res.*  
811 *Lett.*, 37, L08803, doi:10.1029/2010GL042737, 2010.

812 Hennigan, C., Miracolo, M., Engelhart, G., May, A., Presto, A., Lee, T., Sullivan, A., McMeeking, G., Coe, H.,  
813 and Wold, C.: Chemical and physical transformations of organic aerosol from the photo-oxidation of open biomass  
814 burning emissions in an environmental chamber, *Atmos. Chem. Phys.*, 11, 7669-7686, doi:10.5194/acp-11-7669-  
815 2011, 2011.

816 Hennigan, C. J., Sullivan, A. P., Collett Jr, J. L., and Robinson, A. L.: Levoglucosan stability in biomass burning  
817 particles exposed to hydroxyl radicals, *Geophys. Res. Lett.*, 37, L09806, doi:10.1029/2010GL043088, 2010.

818 He, Q., Bluvshstein, N., Segev, L., Meidan, D., Flores, J. M., Brown, S. S., Brune, W., and Rudich, Y.: Evolution  
819 of the complex refractive index of secondary organic aerosols during atmospheric aging, *Environ. Sci. Technol.*,  
820 52, 3456-3465, doi:10.1021/acs.est.7b05742, 2018.

821 Heger, H. J., Zimmermann, R., Dorfner, R., Beckmann, M., Griebel, H., Kettrup, A., and Boesl, U.: On-line  
822 emission analysis of polycyclic aromatic hydrocarbons down to pptv concentration levels in the flue gas of an  
823 incineration pilot plant with a mobile resonance-enhanced multiphoton ionization time-of-flight mass  
824 spectrometer, *Anal. Chem.*, 71, 46-57, doi:10.1021/ac980611y, 1999.

825 Herring, C. L., Faiola, C. L., Massoli, P., Sueper, D., Erickson, M. H., McDonald, J. D., Simpson, C. D., Yost, M.  
826 G., Jobson, B. T., and VanReken, T. M.: New methodology for quantifying polycyclic aromatic hydrocarbons  
827 (PAHs) using high-resolution aerosol mass spectrometry, *Aerosol Sci. Tech.*, 49, 1131-1148,  
828 doi:10.1080/02786826.2015.1101050, 2015.

829 Hoffer, A., Gelencsér, A., Guyon, P., Kiss, G., Schmid, O., Frank, G., Artaxo, P., and Andreae, M.: Optical  
830 properties of humic-like substances (HULIS) in biomass-burning aerosols, *Atmos. Chem. Phys.*, 6, 3563-3570,  
831 doi: 10.5194/acp-6-3563-2006, 2006.

832 Hoffer, A., Tóth, A., Nyirő-Kósa, I., Pósfai, M., and Gelencsér, A.: Light absorption properties of laboratory-  
833 generated tar ball particles, *Atmos. Chem. Phys.*, 16, 239-246, doi:10.5194/acp-16-239-2016, 2016.

834 Huang, K., Zhuang, G., Fu, J. S., Wang, Q., Liu, T., Zhang, R., Jiang, Y., Deng, C., Fu, Q., and Hsu, N.: Typical  
835 types and formation mechanisms of haze in an Eastern Asia megacity, Shanghai, *Atmos. Chem. Phys.*, 12, 105-  
836 124, doi:10.5194/acp-12-105-2012, 2012.

837 Huang, R. J., Yang, L., Cao, J. J., Chen, Y., Chen, Q., Li, Y., Duan, J., Zhu, C., Dai, W., and Wang, K.: Brown  
838 carbon aerosol in Urban Xi'an, Northwest China: the composition and light absorption properties, *Environ. Sci.*  
839 *Technol.*, 52, 6825-6833, doi:10.1021/acs.est.8b02386, 2018.

840 IPCC. Climate Change 2013: the physical science basis. Contribution of working group I to the fifth assessment  
841 report of the intergovernmental panel on climate change. Cambridge, and New York, NY: Cambridge University  
842 Press, 2013.

843 Jacobson, M. Z.: Analysis of aerosol interactions with numerical techniques for solving coagulation, nucleation,  
844 condensation, dissolution, and reversible chemistry among multiple size distributions, *J. Geophys. Res. Atmos.*,  
845 107, D19, 4366, doi:10.1029/2001JD002044, 2002.

846 [Jacobson, M. Z.: Investigating cloud absorption effects: Global absorption properties of black carbon, tar balls,  
847 and soil dust in clouds and aerosols. \*J. Geophys. Res. Atmos.\*, 117\(D6\), doi:10.1029/2011JD017218, 2012.](#)

848 Jacobson, M. Z.: Effects of biomass burning on climate, accounting for heat and moisture fluxes, black and brown  
849 carbon, and cloud absorption effects, *J. Geophys. Res. Atmos.*, 119, 8980-9002,  
850 doi.org/10.1002/2014JD021861, 2014.

851 Jimenez, J., Canagaratna, M., Donahue, N., Prevot, A., Zhang, Q., Kroll, J. H., DeCarlo, P. F., Allan, J. D., Coe,  
852 H., and Ng, N.: Evolution of organic aerosols in the atmosphere, *Science*, 326, 1525-1529, doi:  
853 10.1126/science.1180353, 2009.

854 Jo, D. S., Park, R. J., Lee, S., Kim, S. W., and Zhang, X.: A global simulation of brown carbon: implications for  
855 photochemistry and direct radiative effect, *Atmos. Chem. Phys.*, 16, 3413-3432, doi:10.5194/acp-16-3413-2016,  
856 2016.

857 Kanakidou, M., Seinfeld, J., Pandis, S., Barnes, I., Dentener, F., Facchini, M., Dingenen, R. V., Ervens, B., Nenes,  
858 A., and Nielsen, C.: Organic aerosol and global climate modelling: a review, *Atmos. Chem. Phys.*, 5, 1053-1123,  
859 doi: 1680-7324/acp/2005-5-1053, 2005.

860 Kang, E., Root, M., Toohey, D., and Brune, W.: Introducing the concept of potential aerosol mass (PAM), *Atmos.*  
861 *Chem. Phys.*, 7, 5727-5744, doi: 10.5194/acp-7-5727-2007, 2007.

862 Kim, H., Liu, S., Russell, L. M., and Paulson, S. E.: Dependence of real refractive indices on O:C, H:C and mass  
863 fragments of secondary organic aerosol generated from ozonolysis and photooxidation of limonene and  $\alpha$ -pinene,  
864 *Aerosol Sci. Tech.*, 48, 498-507, doi: 10.1080/02786826.2014.893278, 2014.

865 Kroll, J. H., Donahue, N. M., Jimenez, J. L., Kessler, S. H., Canagaratna, M. R., Wilson, K. R., Altieri, K. E.,  
866 Mazzoleni, L. R., Wozniak, A. S., and Bluhm, H.: Carbon oxidation state as a metric for describing the chemistry  
867 of atmospheric organic aerosol, *Nat. Chem.*, 3, 133, doi: 10.1038/NCHEM.948, 2011.

868 Lack, D. A., Langridge, J. M., Bahreini, R., Cappa, C. D., Middlebrook, A. M., and Schwarz, J. P.: Brown carbon  
869 and internal mixing in biomass burning particles, *Proc. Natl. Acad. Sci. USA*, 109, 14802-14807,  
870 doi:10.1073/pnas.1206575109, 2012.

871 Lambe, A., Onasch, T., Massoli, P., Croasdale, D., Wright, J., Ahern, A., Williams, L., Worsnop, D., Brune, W.,  
872 and Davidovits, P.: Laboratory studies of the chemical composition and cloud condensation nuclei (CCN) activity  
873 of secondary organic aerosol (SOA) and oxidized primary organic aerosol (OPOA), *Atmos. Chem. Phys.*, 11,  
874 8913-8928, doi:10.5194/acp-11-8913-2011, 2011.

875 Lambe, A., Massoli, P., Zhang, X., Canagaratna, M., Nowak, J., Daube, C., Chao, Y., Nie, W., Onasch, T., and  
876 Jayne, J.: Controlled nitric oxide production via O (<sup>1</sup>D)+ N<sub>2</sub>O reactions for use in oxidation flow reactor studies,  
877 *Atmos. Meas. Tech.*, 10, 2283, doi: 10.5194/amt-10-2283-2017, 2017.

878 Laskin, A., Laskin, J., and Nizkorodov, S. A.: Chemistry of atmospheric brown carbon, *Chem. Rev.*, 115, 4335-  
879 4382, doi:10.1021/cr5006167, 2015.

880 Laskin, A., Smith, J. S., and Laskin, J.: Molecular characterization of nitrogen-containing organic compounds in  
881 biomass burning aerosols using high-resolution mass spectrometry, *Environ. Sci. Technol.*, 43, 3764-3771,  
882 doi:10.1021/es803456n, 2009.

883 Lee, H. J., Aiona, P. K., Laskin, A., Laskin, J., and Nizkorodov, S. A.: Effect of solar radiation on the optical  
884 properties and molecular composition of laboratory proxies of atmospheric brown carbon, *Environ. Sci. Technol.*,  
885 48, 10217-10226, doi:10.1021/es502515r, 2014.

886 Levinson, R., Akbari, H., and Berdahl, P.: Measuring solar reflectance-Part I: Defining a metric that accurately  
887 predicts solar heat gain, *Sol. Energy*, 84, 1717-1744, doi:10.1016/j.solener.2010.04.018, 2010.

888 Li, C., Ma, Z., Chen, J., Wang, X., Ye, X., Wang, L., Yang, X., Kan, H., Donaldson, D., and Mellouki, A.:  
889 Evolution of biomass burning smoke particles in the dark, *Atmos. Environ.*, 120, 244-252,  
890 doi:10.1016/j.atmosenv.2015.09.003, 2015.

891 Li, C., Hu, Y., Zhang, F., Chen, J., Ma, Z., Ye, X., Yang, X., Wang, L., Tang, X., and Zhang, R.: Multi-pollutant  
892 emissions from the burning of major agricultural residues in China and the related health-economic effects, *Atmos.*  
893 *Chem. Phys.*, 17, 4957-4988, doi:10.5194/acp-17-4957-2017, 2017.

894 Li, Y., Huang, D., Cheung, H. Y., Lee, A., and Chan, C. K.: Aqueous-phase photochemical oxidation and direct  
895 photolysis of vanillin-a model compound of methoxy phenols from biomass burning, *Atmos. Chem. Phys.*, 14,  
896 2871-2885, doi:10.5194/acp-14-2871-2014, 2014.

897 Li, Y. J., Yeung, J. W., Leung, T. P., Lau, A. P., and Chan, C. K.: Characterization of organic particles from incense  
898 burning using an aerodyne high-resolution time-of-flight aerosol mass spectrometer, *Aerosol Sci. Tech.*, 46, 654-  
899 665, doi:10.1080/02786826.2011.653017, 2012.

900 Lin, P., Liu, J., Shilling, J. E., Kathmann, S. M., Laskin, J., and Laskin, A.: Molecular characterization of brown  
901 carbon (BrC) chromophores in secondary organic aerosol generated from photo-oxidation of toluene, *Phys. Chem.*  
902 *Chem. Phys.*, 17, 23312-23325, doi:10.1039/C5CP02563J, 2015.

903 Lin, P., Aiona, P. K., Li, Y., Shiraiwa, M., Laskin, J., Nizkorodov, S. A., and Laskin, A.: Molecular characterization  
904 of brown carbon in biomass burning aerosol particles, *Environ. Sci. Technol.*, 50, 11815-11824,  
905 doi:10.1021/acs.est.6b03024, 2016.

906 Lin, P., Bluvshstein, N., Rudich, Y., Nizkorodov, S. A., Laskin, J., and Laskin, A.: Molecular Chemistry of  
907 Atmospheric Brown Carbon Inferred from a Nationwide Biomass Burning Event, *Environ. Sci. Technol.*, 51,  
908 11561-11570, doi:10.1021/acs.est.7b02276, 2017.

909 [Lin, P., Fleming, L. T., Nizkorodov, S. A., Laskin, J., and Laskin, A.: Comprehensive Molecular Characterization](#)  
910 [of Atmospheric Brown Carbon by High Resolution Mass Spectrometry with Electrospray and Atmospheric](#)  
911 [Pressure Photoionization, \*Anal. chem.\*, 90, 12493-12502, doi:10.1021/acs.analchem.8b02177, 2018.](#)

912 Liu, J., Bergin, M., Guo, H., King, L., Kotra, N., Edgerton, E., and Weber, R.: Size-resolved measurements of  
913 brown carbon in water and methanol extracts and estimates of their contribution to ambient fine-particle light  
914 absorption, *Atmos. Chem. Phys.*, 13, 12389-12404, doi:10.5194/acp-13-12389-2013, 2013.

915 Liu, J., Lin, P., Laskin, A., Laskin, J., Kathmann, S. M., Wise, M., Caylor, R., Imholt, F., Selimovic, V., and  
916 Shilling, J. E.: Optical properties and aging of light-absorbing secondary organic aerosol, *Atmos. Chem. Phys.*,  
917 16, 12815-12827, doi:10.5194/acp-16-12815-2016, 2016.

918 Lu, J. W., Flores, J. M., Lavi, A., Abo-Riziq, A., and Rudich, Y.: Changes in the optical properties of benzo[a]  
919 pyrene-coated aerosols upon heterogeneous reactions with NO<sub>2</sub> and NO<sub>3</sub>, *Phys. Chem. Chem. Phys.*, 13, 6484-  
920 6492, doi:10.1039/C0CP02114H, 2011.

921 McDonald, J. D., Zielinska, B., Fujita, E. M., Sagebiel, J. C., Chow, J. C., and Watson, J. G.: Fine particle and  
922 gaseous emission rates from residential wood combustion, *Environ. Sci. Technol.*, 34, 2080-2091,  
923 doi:10.1021/es9909632, 2000.

924 Moise, T., Flores, J. M., and Rudich, Y.: Optical properties of secondary organic aerosols and their changes by  
925 chemical processes, *Chem. Rev.*, 115, 4400-4439, doi:10.1021/cr5005259, 2015.

926 Miljevic, B., Hedayat, F., Stevanovic, S., Fairfull-Smith, K. E., Bottle, S., and Ristovski, Z.: To sonicate or not to  
927 sonicate PM filters: reactive oxygen species generation upon ultrasonic irradiation, *Aerosol Sci. Tech.*, 48, 1276-  
928 1284, doi:10.1080/02786826.2014.981330, 2014.

929 Mutzel, A., Rodigast, M., Iinuma, Y., Böge, O., and Herrmann, H.: An improved method for the quantification of  
930 SOA bound peroxides, *Atmos. Environ.*, 67, 365-369, doi:10.1016/j.atmosenv.2012.11.012, 2013.

931 Ng, N., Chhabra, P., Chan, A., Surratt, J. D., Kroll, J., Kwan, A., McCabe, D., Wennberg, P., Sorooshian, A., and  
932 Murphy, S.: Effect of NO<sub>x</sub> level on secondary organic aerosol (SOA) formation from the photooxidation of  
933 terpenes, *Atmos. Chem. Phys.*, 7, 5159-5174, doi:10.5194/acp-7-5159-2007, 2007.

934 Ng, N., Canagaratna, M., Zhang, Q., Jimenez, J., Tian, J., Ulbrich, I., Kroll, J., Docherty, K., Chhabra, P., and  
935 Bahreini, R.: Organic aerosol components observed in Northern Hemispheric datasets from Aerosol Mass  
936 Spectrometry, *Atmos. Chem. Phys.*, 10, 4625-4641, doi:10.5194/acp-10-4625-2010, 2010.

937 Ng, N., Canagaratna, M., Jimenez, J., Chhabra, P., Seinfeld, J., and Worsnop, D.: Changes in organic aerosol  
938 composition with aging inferred from aerosol mass spectra, *Atmos. Chem. Phys.*, 11, 6465-6474, doi:10.5194/acp-  
939 11-6465-2011, 2011.

940 Park, R. J., Kim, M. J., Jeong, J. I., Youn, D., and Kim, S.: A contribution of brown carbon aerosol to the aerosol  
941 light absorption and its radiative forcing in East Asia, *Atmos. Environ.*, 44, 1414-1421,  
942 doi:10.1016/j.atmosenv.2010.01.042, 2010.

943 Passig, J., Schade, J., Oster, M., Fuchs, M., Ehlert, S., Jäger, C., Sklorz, M., and Zimmermann, R.: Aerosol mass  
944 spectrometer for simultaneous detection of polyaromatic hydrocarbons and inorganic components from individual  
945 particles, *Anal. Chem.*, 89, 6341-6345, doi:10.1021/acs.analchem.7b01207, 2017.

946 Peng, Z., Day, D., Stark, H., Li, R., Lee-Taylor, J., Palm, B., Brune, W., and Jimenez, J. L.: HO<sub>x</sub> radical chemistry  
947 in oxidation flow reactors with low-pressure mercury lamps systematically examined by modeling, *Atmos. Meas.*  
948 *Tech.*, 8, 4863-4890, doi:10.5194/amt-8-4863-2015, 2015.

949 Peng, Z., Day, D. A., Ortega, A. M., Palm, B. B., Hu, W., Stark, H., Li, R., Tsigaridis, K., Brune, W. H., and  
950 Jimenez, J. L.: Non-OH chemistry in oxidation flow reactors for the study of atmospheric chemistry systematically  
951 examined by modeling, *Atmos. Chem. Phys.*, 16, 4283-4305, doi:10.5194/acp-16-4283-2016, 2016.

952 Peng, Z., and Jimenez, J. L.: Modeling of the chemistry in oxidation flow reactors with high initial NO, *Atmos.*  
953 *Chem. Phys.*, 17, 11991-12010, doi:10.5194/acp-17-11991-2017, 2017.

954 Pettersson, A., Lovejoy, E. R., Brock, C. A., Brown, S. S., and Ravishankara, A.: Measurement of aerosol optical  
955 extinction at 532 nm with pulsed cavity ring down spectroscopy, *J. Aerosol Sci.*, 35, 995-1011,  
956 doi:10.1016/j.jaerosci.2004.02.008, 2004.

957 Phillips, S. M., and Smith, G. D.: Light absorption by charge transfer complexes in brown carbon aerosols,  
958 *Environ. Sci. Technol. Lett.*, 1, 382-386, doi:10.1021/ez500263j, 2014.

959 Pósfai, M., Gelencsér, A., Simonics, R., Arató, K., Li, J., Hobbs, P. V., and Buseck, P. R.: Atmospheric tar balls:  
960 Particles from biomass and biofuel burning, *J. Geophys. Res. Atmos.*, 109, D06213, doi:10.1029/2003JD004169,  
961 2004.

962 [Rajput, P., and Sarin, M.: Polar and non-polar organic aerosols from large-scale agricultural-waste burning](#)  
963 [emissions in Northern India: implications to organic mass-to-organic carbon ratio, \*Chemosphere\*, 103, 74-](#)  
964 [79, doi:10.1016/j.chemosphere.2013.11.028, 2014.](#)

965 Reid, J. S., Eck, T. F., Christopher, S. A., Koppmann, R., Dubovik, O., Eleuterio, D., Holben, B. N., Reid, E. A.,  
966 and Zhang, J.: A review of biomass burning emissions part III: intensive optical properties of biomass burning  
967 particles, *Atmos. Chem. Phys.*, 5, 827-849, doi:10.5194/acp-5-827-2005, 2005.

968 Rettner, C. T., and Brophy, J. H.: Resonance enhanced laser ionisation mass spectrometry of four aromatic  
969 molecules, *Chem. Phys.*, 56, 53-61, doi:10.1016/0301-0104(81)85099-9, 1981.

970 Rollins, A. W., Browne, E. C., Min, K. E., Pusede, S. E., Wooldridge, P. J., Gentner, D. R., Goldstein, A. H., Liu,  
971 S., Day, D. A., and Russell, L. M.: Evidence for NO<sub>x</sub> control over nighttime SOA formation, *Science*, 337, 1210-  
972 1212, doi:10.1126/science.1221520, 2012.

973 Rudich, Y., Donahue, N. M., and Mentel, T. F.: Aging of organic aerosol: Bridging the gap between laboratory  
974 and field studies, *Annu. Rev. Phys. Chem.*, 58, 321-352, doi:10.1146/annurev.physchem.58.032806.104432, 2007.

975 Russell, P., Bergstrom, R., Shinozuka, Y., Clarke, A., DeCarlo, P., Jimenez, J., Livingston, J., Redemann, J.,  
976 Dubovik, O., and Strawa, A.: Absorption Ångström Exponent in AERONET and related data as an indicator of  
977 aerosol composition, *Atmos. Chem. Phys.*, 10, 1155-1169, doi:10.5194/acp-10-1155-2010, 2010.

978 Samburova, V., Connolly, J., Gyawali, M., Yatavelli, R. L., Watts, A. C., Chakrabarty, R. K., Zielinska, B.,  
979 Moosmüller, H., and Khlystov, A.: Polycyclic aromatic hydrocarbons in biomass-burning emissions and their  
980 contribution to light absorption and aerosol toxicity, *Sci. Total Environ.*, 568, 391-401,  
981 doi:10.1016/j.scitotenv.2016.06.026, 2016.

982 Schauer, J. J., Kleeman, M. J., Cass, G. R., and Simoneit, B. R.: Measurement of emissions from air pollution  
983 sources. 3. C1-C29 organic compounds from fireplace combustion of wood, *Environ. Sci. Technol.*, 35, 1716-  
984 1728, doi:10.1021/es001331e, 2001.

985 Sedlacek III, A. J., Buseck, P. R., Adachi, K., Onasch, T. B., Springston, S. R., and Kleinman, L.: Formation and  
986 evolution of Tar Balls from Northwestern US wildfires, *Atmos. Chem. Phys.*, 18, 11289-11301, doi:10.5194/acp-  
987 18-11289-2018, 2018.

988 Seinfeld, J. H., and Pandis, S. N.: *Atmospheric chemistry and physics: from air pollution to climate change*, 3rd  
989 edition, John Wiley & Sons, Inc., Hoboken, New Jersey, USA, 2016.

990 [Sengupta, D., Samburova, V., Bhattarai, C., Kirillova, E., Mazzoleni, L., Iaukea-Lum, M., Watts, A.,](#)  
991 [Moosmüller, H., and Khlystov, A.: Light absorption by polar and non-polar aerosol compounds from](#)  
992 [laboratory biomass combustion, \*Atmos. Chem. Phys.\*, 18, 10849-10867, doi:10.5194/acp-18-10849-2018,](#)  
993 [2018.](#)

994 Shamjad, P. M., Satish, R. V., Thamban, N. M., Rastogi, N., and Tripathi, S.: Absorbing refractive index and direct  
995 radiative forcing of atmospheric Brown Carbon over Gangetic Plain, *ACS Earth Space Chem.*, 2, 31-37,  
996 doi:10.1021/acsearthspacechem.7b00074, 2018.

997 Shen, G., Tao, S., Wei, S., Zhang, Y., Wang, R., Wang, B., Li, W., Shen, H., Huang, Y., and Yang, Y.: Retene  
998 emission from residential solid fuels in China and evaluation of retene as a unique marker for soft wood  
999 combustion, *Environ. Sci. Technol.*, 46, 4666-4672, doi:10.1021/es300144m, 2012.

1000 Shen, H., Huang, Y., Wang, R., Zhu, D., Li, W., Shen, G., Wang, B., Zhang, Y., Chen, Y., and Lu, Y.: Global  
1001 atmospheric emissions of polycyclic aromatic hydrocarbons from 1960 to 2008 and future predictions, *Environ.*  
1002 *Sci. Technol.*, 47, 6415-6424, doi:10.1021/es400857z, 2013.

1003 Shrivastava, M., Cappa, C. D., Fan, J., Goldstein, A. H., Guenther, A. B., Jimenez, J. L., Kuang, C., Laskin, A.,  
1004 Martin, S. T., and Ng, N. L.: Recent advances in understanding secondary organic aerosol: Implications for global  
1005 climate forcing, *Rev. Geophys.*, 55, 509-559, doi:10.1002/2016RG000540, 2017.

1006 Sigsgaard, T., Forsberg, B., Annesi-Maesano, I., Blomberg, A., Bølling, A., Boman, C., Bønløkke, J., Brauer, M.,  
1007 Bruce, N., and Héroux, M. E.: Health impacts of anthropogenic biomass burning in the developed world, *Eur.*  
1008 *Respir. J.*, 46, 1577-1588, doi:10.1183/13993003.01865-2014, 2015.

1009 Sumlin, B. J., Pandey, A., Walker, M. J., Pattison, R. S., Williams, B. J., and Chakrabarty, R. K.: Atmospheric  
1010 Photooxidation Diminishes Light Absorption by Primary Brown Carbon Aerosol from Biomass Burning, *Environ.*  
1011 *Sci. Technol. Lett.*, 4, 540-545, doi:10.1021/acs.estlett.7b00393, 2017.

1012 Sumlin, B. J., Oxford, C. R., Seo, B., Pattison, R. R., Williams, B. J., and Chakrabarty, R. K.: Density and  
1013 homogeneous internal composition of primary brown carbon aerosol, *Environ. Sci. Technol.*, 52, 3982-3989, doi:  
1014 10.1021/acs.est.8b00093, 2018.

1015 Tavakoli, F., and Olfert, J.: An instrument for the classification of aerosols by particle relaxation time: theoretical  
1016 models of the aerodynamic aerosol classifier, *Aerosol Sci. Tech.*, 47, 916-926,  
1017 doi:10.1080/02786826.2013.802761, 2013.

1018 Tavakoli, F., and Olfert, J. S.: Determination of particle mass, effective density, mass-mobility exponent, and  
1019 dynamic shape factor using an aerodynamic aerosol classifier and a differential mobility analyzer in tandem, *J.*  
1020 *Aerosol Sci.*, 75, 35-42, doi:10.1016/j.jaerosci.2014.04.010, 2014.

1021 Tóth, A., Hoffer, A., Nyirő-Kósa, I., Pósfai, M., and Gelencsér, A.: Atmospheric tar balls: aged primary droplets  
1022 from biomass burning?, *Atmos. Chem. Phys.*, 14, 6669-6675, doi:10.5194/acp-14-6669-2014, 2014.

1023 Washenfelder, R., Attwood, A., Brock, C., Guo, H., Xu, L., Weber, R., Ng, N., Allen, H., Ayres, B., and Baumann,  
1024 K.: Biomass burning dominates brown carbon absorption in the rural southeastern United States, *Geophys. Res.*  
1025 *Let.*, 42, 653-664, doi:10.1002/2014GL062444, 2015.

1026 Washenfelder, R., Flores, J., Brock, C., Brown, S., and Rudich, Y.: Broadband measurements of aerosol extinction  
1027 in the ultraviolet spectral region, *Atmos. Meas. Tech.*, 6, 861-877, doi:10.5194/amt-6-861-2013, 2013.

1028 Wei, C., Bandowe, B. A. M., Han, Y., Cao, J., Zhan, C., and Wilcke, W.: Polycyclic aromatic hydrocarbons (PAHs)  
1029 and their derivatives (alkyl-PAHs, oxygenated-PAHs, nitrated-PAHs and azaarenes) in urban road dusts from  
1030 Xi'an, Central China, *Chemosphere*, 134, 512-520, doi:10.1016/j.chemosphere.2014.11.052, 2015.

1031 Weimer, S., Alfara, M., Schreiber, D., Mohr, M., Prévôt, A., and Baltensperger, U.: Organic aerosol mass spectral  
1032 signatures from wood-burning emissions: Influence of burning conditions and wood type, *J. Geophys. Res.*  
1033 *Atmos.*, 113, doi:10.1029/2007JD009309, 2008.

1034 Wong, J. P., Zhou, S., and Abbatt, J. P.: Changes in secondary organic aerosol composition and mass due to  
1035 photolysis: relative humidity dependence, *J. Phys. Chem. A*, 119, 4309-4316, doi:10.1021/jp506898c, 2014.

1036 Xie, M., Hays, M. D., and Holder, A. L.: Light-absorbing organic carbon from prescribed and laboratory biomass  
1037 burning and gasoline vehicle emissions, *Scientific Reports*, 7, 7318, doi:10.1038/s41598-017-06981-8, 2017.

1038 Yee, L., Kautzman, K., Loza, C., Schilling, K., Coggon, M., Chhabra, P., Chan, M., Chan, A., Hersey, S., and  
1039 Crouse, J.: Secondary organic aerosol formation from biomass burning intermediates: phenol and  
1040 methoxyphenols, *Atmos. Chem. Phys.*, 13, 8019-8043, doi:10.5194/acp-13-8019-2013, 2013.

1041 Yu, L., Smith, J., Laskin, A., Anastasio, C., Laskin, J., and Zhang, Q.: Chemical characterization of SOA formed  
1042 from aqueous-phase reactions of phenols with the triplet excited state of carbonyl and hydroxyl radical, *Atmos.*  
1043 *Chem. Phys.*, 14, 13801-13816, doi:10.5194/acp-14-13801-2014, 2014.

1044 Zhang, H., and Ying, Q.: Secondary organic aerosol from polycyclic aromatic hydrocarbons in Southeast Texas,  
1045 *Atmos. Environ.*, 55, 279-287, doi:10.1016/j.atmosenv.2012.03.043, 2012.

1046 Zhang, X., and Seinfeld, J.: A functional group oxidation model (FGOM) for SOA formation and aging, *Atmos.*  
1047 *Chem. Phys.*, 13, 5907-5926, doi:10.5194/acp-14-13801-2014, 2013.

1048 Zhong, M., and Jang, M.: Dynamic light absorption of biomass-burning organic carbon photochemically aged  
1049 under natural sunlight, *Atmos. Chem. Phys.*, 14, 1517-1525, doi:10.5194/acp-14-1517-2014, 2014.

1050 Zhou, S., Collier, S., Jaffe, D. A., Briggs, N. L., Hee, J., Sedlacek III, A. J., Kleinman, L., Onasch, T. B., and  
1051 Zhang, Q.: Regional influence of wildfires on aerosol chemistry in the western US and insights into atmospheric  
1052 aging of biomass burning organic aerosol, *Atmos. Chem. Phys.*, 17, 2477-2493, doi:10.5194/acp-17-2477-2017,  
1053 2017.

1054

1055 **Caption of Table and Figure**

1056 **Table 1.** Experimental conditions for tar balls photochemical oxidation

1057 **Table 2.** Comparison of tar ball particle optical parameters with reference values of BBOA (mean  $\pm$  standard  
1058 deviation)

1059 **Figure 1.** Experimental setup for laboratory generation and aging of tar ball aerosol: including generation setup,  
1060 OFR photochemical aging, gaseous-particulate chemical monitoring, particle size distribution and optical  
1061 properties measurements.

1062 **Figure 2.** High-resolution AMS mass spectra of fresh polar and nonpolar tar ball particles. Four ion groups are  
1063 grouped for clarity as:  $C_xH_y^+$  (green),  $C_xH_yO^+$  (purple),  $C_xH_yO_z^+$  ( $z>1$ ) (violet),  $C_xH_yO_iN_p^+$  ( $i\geq 0, p\geq 1$ ) (light blue).  
1064 The mass fractions of the four fragment groups are presented by pie-charts.

1065 **Figure 3.** LD-REMPI mass spectra of exemplary single tar ball particles, some feature peaks were identified and  
1066 labeled. a) Nonpolar tar ball spectra shows predominantly alkyl-substituted and unsubstituted PAHs. b) Polar tar  
1067 ball spectra reveals many oxidized aromatics, e.g., methoxy-phenol, benzenediol. Note the softwood combustion  
1068 marker retene at  $m/z=234$ , its characteristic fragments ( $m/z=203, 204, 205, 219$ ) and possible retene derivatives  
1069 ( $m/z=248, 250$ ).

1070 **Figure 4.** Wavelength-dependent RI and SSA for tar ball particles generated from polar, nonpolar and mixture of  
1071 the two phases tarry solutions (only retrieval for mixture of 1:1 in vol. is shown for clarity, optical results for the  
1072 rest two mixtures can be found in supporting materials). The shaded areas indicate the upper and lower limits of  
1073 the imaginary part calculated from UV-Vis spectra of methanol extracts from the corresponding tar ball particles  
1074 samples: a) real part, b) imaginary part, and c) SSA calculated for 150 nm particles. Overplayed in green symbol  
1075 are previous measurements of biomass burning from the literature.

1076 **Figure 5.** Evolution of the retrieved wavelength-dependent complex RI and SSA as a function of O:C ratio for tar  
1077 ball particles upon OH photochemical oxidation: a) real part, b) imaginary part, and c) SSA calculated for 150 nm  
1078 particles. The color scale shows the span in the RI for the wavelengths measured from 365 to 425 nm. For clarity,  
1079 error bars for O:C ratio ( $\pm 0.01$ ), RI ( $\pm 0.007$  for real part, and  $\pm 0.003$  for imaginary part on average), and SSA  
1080 ( $\pm 0.006$ ) are not shown. Two dashed lines trace the RI and SSA at 375 nm (purple) and 405 nm (green).  
1081  $O_{0.7}\sim O_{6.7}$  represent equivalent atmospheric photochemical oxidation for 0.7 and up to 6.7 days.

1082 **Figure 6.** Dynamic changes for the chemical characteristics of tar ball particle under NO<sub>x</sub>-free OH photochemical  
1083 oxidation: a) OM/OC, H:C ratio, particle density, and average carbon oxidation state ( $\overline{OS_c}$ ) changes as a function

1084 of O:C ratio; b) mass spectra evolution with oxidation times in term of  $C_xH_y^+$ ,  $C_xH_yO^+$ ,  $C_xH_yO_z^+$ , and  $C_xH_yO_iN_p^+$   
1085 fragment groups.

1086 **Figure 7.** Comparison of  $f_{44}$  and  $f_{43}$  values from ambient data sets (Ng. et al., 2010) and values from ambient  
1087 biomass burning organic aerosol.

1088 **Figure 8.** Dynamic changes for chemical characteristics of tar ball aerosols under  $NO_x$ -dependent OH  
1089 photochemical oxidation: a) OM/OC, O:C, H:C, and particle density changes; b) mass spectra changes with  
1090 different oxidation conditions in term of  $C_xH_y^+$ ,  $C_xH_yO^+$ ,  $C_xH_yO_z^+$ , and  $C_xH_yO_zN_p^+$  fragment groups.  $C_xH_yO_zN_p^+$   
1091 include all nitrogen-containing fragments, (e.g.,  $C_xH_yON^+$ ,  $C_xH_yO_zNi^+$ ,  $C_xH_yN^+$ , etc.),  $NO_y^+$  include  $NO^+$  and  $NO_2^+$ .  
1092 O\_3.9 represents 3.9 days equivalent atmospheric photochemical aging in absence of  $NO_x$ , N\_0.5 and N\_2.0  
1093 indicate photochemical oxidation with 0.5 and 2.0 vol.%  $N_2O$  addition at  $\sim 4.0$  days atmospheric oxidation.

1094 **Figure 9.** Changes of retrieved spectra-dependent RI as a function of O:C ratio for tar ball particles upon  $NO_x$ -  
1095 dependent photochemical oxidation: a) real part, b) imaginary part, and c) SSA calculated from 150 nm particles.  
1096 For clarity, error bars for O:C ratio ( $\pm 0.01$ ), RI ( $\pm 0.006$  for real part, and  $\pm 0.003$  for imaginary part on average),  
1097 and SSA ( $\pm 0.007$ ) are not shown. O\_3.9 represents 3.9 days equivalent atmospheric photochemical aging in  
1098 absence of  $NO_x$ , N\_0.5 and N\_2.0 indicate photochemical oxidation with 0.5 and 2.0 vol.%  $N_2O$  addition at  $\sim 4.0$   
1099 days atmospheric oxidation.

1100 **Figure 10.** Size-resolved light extinction and absorption efficiency ratio of  $NO_x$ -dependent photooxidized tar balls  
1101 compared to the fresh tar ball particles: a) and c) extinction ratios at 375 and 405 nm, b) and d) absorption ratios  
1102 at 375 and 405 nm. O\_3.9 represents 3.9 days equivalent atmospheric photochemical aging in absence of  $NO_x$ ,  
1103 N\_0.5 and N\_2.0 indicate photochemical oxidation with 0.5 and 2.0 vol.%  $N_2O$  addition at  $\sim 4.0$  days atmospheric  
1104 oxidation.

1105 **Figure 11.** Calculated size-resolved simple radiative forcing (SRF,  $W g^{-1}$ ) by tar ball aerosols, integrated over  
1106 365–425 nm incident solar irradiation for fresh and  $NO_x$ -dependent photooxidized tar balls: a) ground-based  
1107 radiative forcing, b) snow-based radiative forcing.

1108 **Table 1.** Experimental conditions for tar ball particles photochemical oxidation

Experiment	O <sub>3</sub> (ppm)	N <sub>2</sub> O mixing ratio	Endpoint NO <sub>x</sub> (ppb)	RH (%)	water mixing ratio	Exposure	
						OH radical (molecules cm <sup>-3</sup> s)	photon flux (photons cm <sup>-2</sup> )
P1	—	—	—	38.90	0.0126	—	7.47E+15
P2	—	—	—	39.70	0.0128	—	4.83E+16
P3	—	—	—	40.50	0.0130	—	1.00E+17
O_0.7	24.46	—	—	37.29	0.0120	8.68E+10	1.56E+15
O_1.7	24.76	—	—	37.66	0.0122	2.23E+11	7.47E+15
O_3.9	24.63	—	—	35.58	0.0115	5.11E+11	4.83E+16
O_6.7	25.31	—	—	35.67	0.0116	8.65E+11	5.17E+16
N_0.5	24.18	0.005	96.1	36.60	0.0118	5.37E+11	5.92E+16
N_2.0	28.21	0.020	528.3	35.90	0.0116	4.85E+11	1.00E+17

1109 Note: P1~P3 mean photolysis test, O\_0.7~O\_6.7 correspond to photochemical oxidation experiment from equivalent 0.7 day to 6.7 days

1110 ageing, and N\_0.5 and N\_2.0 indicate photochemical oxidation with N<sub>2</sub>O addition at 0.5 vol.% and 2 vol.% mixing ratios (standard deviation

1111 for the parameters were not given in above table)

1112 **Table 2.** Compare of tar ball particle optical properties with reference values of BBOA (mean  $\pm$  standard deviation)

BrC	Complex Refractive index			$\hat{A}_{abs}$	$\hat{A}_{abs\_UVVIS}$	$\hat{A}_{ext}$	Reference
	Average	375nm	405nm				
Nonpolar	(1.661 $\pm$ 0.008)+(0.020 $\pm$ 0.004)i	(1.671 $\pm$ 0.003)+(0.025 $\pm$ 0.003)i	(1.659 $\pm$ 0.011)+(0.017 $\pm$ 0.002)i	5.87 $\pm$ 0.37	5.74	3.81 $\pm$ 0.18	This work
Mixture (2:1 in vol.)	(1.670 $\pm$ 0.010)+(0.017 $\pm$ 0.004)i	(1.682 $\pm$ 0.008)+(0.021 $\pm$ 0.002)i	(1.668 $\pm$ 0.007)+(0.013 $\pm$ 0.001)i	6.79 $\pm$ 0.91	7.08	4.01 $\pm$ 0.09	
Mixture (1:1 in vol.)	(1.694 $\pm$ 0.011)+(0.013 $\pm$ 0.003)i	(1.703 $\pm$ 0.015)+(0.017 $\pm$ 0.001)i	(1.689 $\pm$ 0.011)+(0.009 $\pm$ 0.002)i	6.16 $\pm$ 0.54	7.38	3.73 $\pm$ 0.23	
Mixture (1:2 in vol.)	(1.672 $\pm$ 0.010)+(0.011 $\pm$ 0.004)i	(1.683 $\pm$ 0.005)+(0.018 $\pm$ 0.002)i	(1.667 $\pm$ 0.003)+(0.006 $\pm$ 0.003)i	6.66 $\pm$ 0.63	7.24	4.06 $\pm$ 0.11	
Polar	(1.635 $\pm$ 0.009)+(0.003 $\pm$ 0.003)i	(1.647 $\pm$ 0.003)+(0.005 $\pm$ 0.001)i	(1.635 $\pm$ 0.004)+(0.004 $\pm$ 0.003)i	6.72 $\pm$ 2.28 <sup>a</sup>	7.83	3.93 $\pm$ 0.06	
BBOA	1.590+0.029i@375nm, 1.570+0.010i@405nm (IPN)			6.4~7.4			Sumlin et al., 2017; 2018
BBOA	1.590+0.017i@405nm (IPN)						Flowers et al., 2010
BBOA	k: 0.009@404nm (CRDS-PAS)						Lack et al., 2012
Tar ball	1.78+0.015i, 1.83+0.0086i@405nm (IPN)			4.2~6.4			Chakrabarty et al., 2010
Tar ball	1.56+0.02i @405nm (CRDS-UVVIS)						Hand et al., 2005
BBOA	1.53+0.07i (WELAS, open fire), 1.54+0.04i (WELAS, smoldering)						Adler et al., 2011
BBOA	1.64+0.03i@405nm (BBCES-Neph)			4~6 <sup>b</sup>		2~3 <sup>b</sup>	Bluvshstein et al., 2017
BBOA_HULIS	1.653+0.002i, 1.685+0.002i@532nm(Nep-PAS)				6~7		Hoffer et al., 2006
BBOA_HULIS	1.616+0.023i@390nm(CRDS)						Dinar et al., 2008
BBOA	1.550+0.033i@365nm (BBCES)						Washenfelder et al., 2015
BBOA					6.9~11.4 <sup>c</sup>		Chen and Bond, 2010
BBOA					5.3~8.1 <sup>c</sup>		Xie et al., 2017
Ambient SOA					6.0~6.3 <sup>c</sup>		Huang et al., 2018
Ambient SOA	k: 0.046@365nm, 0.039@405nm, 0.036@420nm (LWCC)						Shamjad et al., 2018

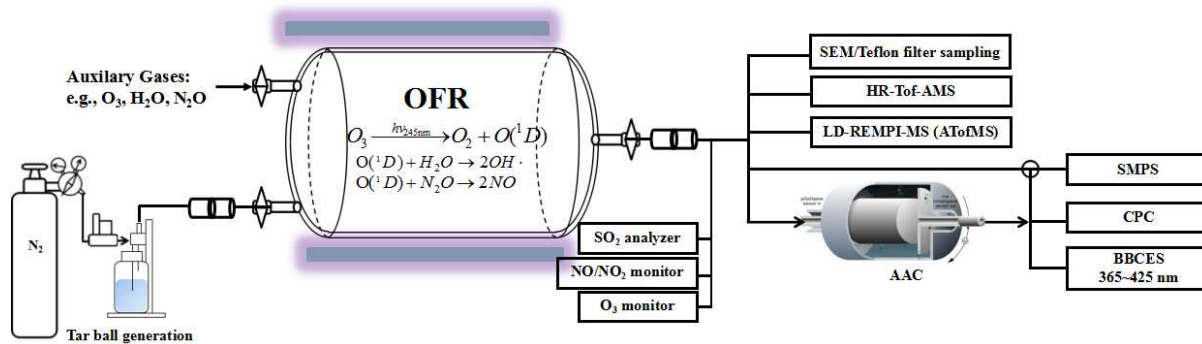
1113 Note:  $\hat{A}_{abs}$  and  $\hat{A}_{ext}$  were calculated from tar ball particle with median diameter of 150 nm in this study

1114 <sup>a</sup> regressed over wavelength range of 365~400 nm, no absorption detected over 410 nm using BBCES system

1115 <sup>b</sup> regressed over wavelength range of 300~650 nm for bulk fire plume emissions

1116 <sup>c</sup>  $\hat{A}_{abs\_UVVIS}$  of methanol extracts over whole range from 300/360~600 nm

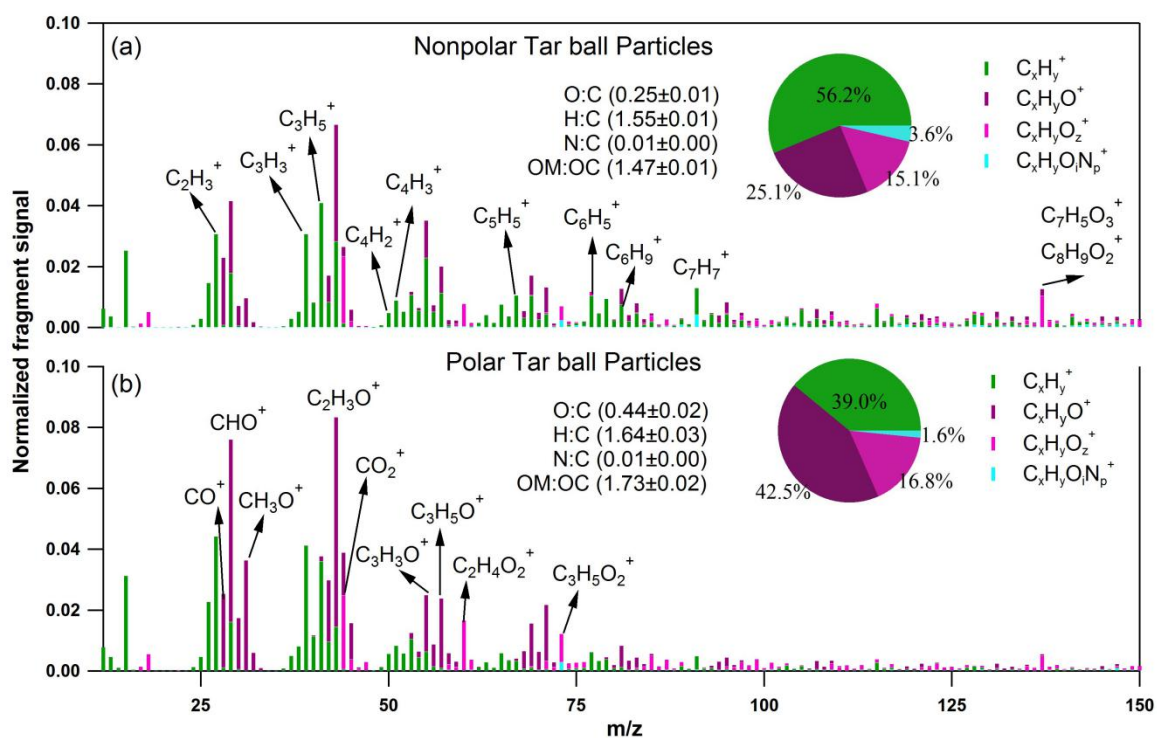
1117 Instrument: IPN(integrated photoacoustic nephelometer), CRDS (cavity ring-down spectrometer), PAS (photoacoustic absorption spectrometer), WELAS (white light optical particle counter), LWCC (a liquid waveguide  
1118 capillary cell)



1119

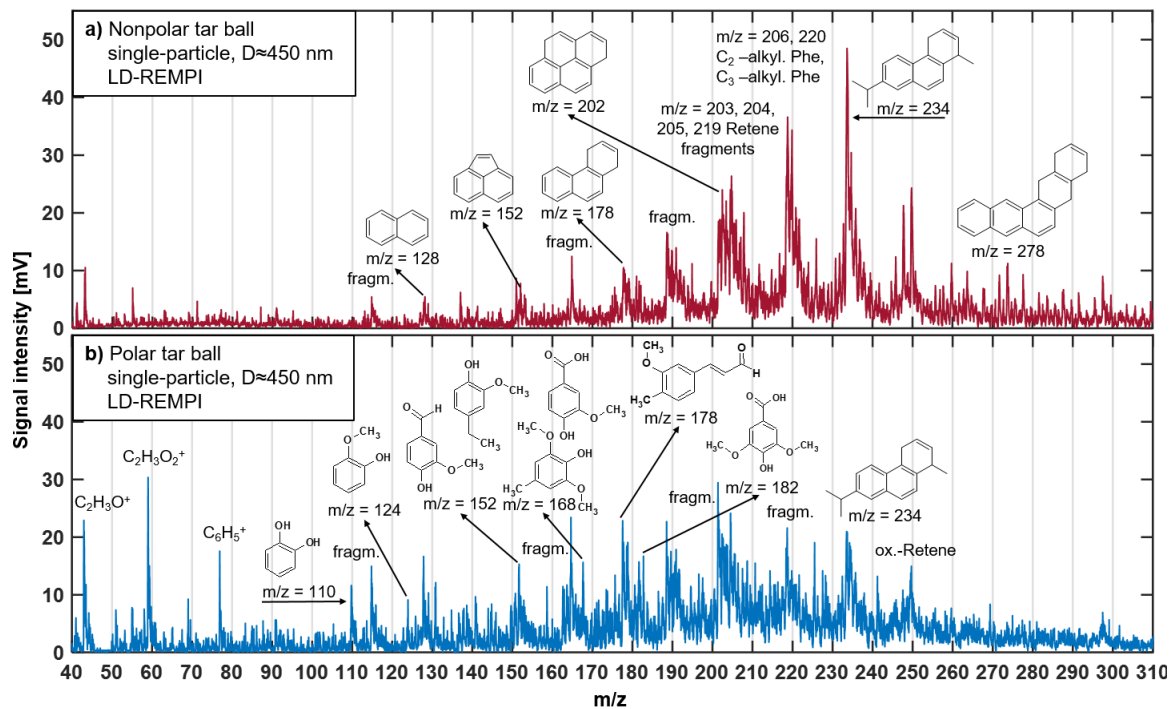
1120 **Figure 1.** Experimental setup for laboratory generation and aging of tar ball aerosol: including generation setup, OFR

1121 photochemical aging, gaseous-particulate chemical monitoring, particle size distribution and optical properties measurements.



1122

1123 **Figure 2.** High-resolution AMS mass spectra of fresh polar and nonpolar tar ball particles. Four ion groups are grouped for  
1124 clarity as:  $C_xH_y^+$  (green),  $C_xH_yO^+$  (purple),  $C_xH_yO_z^+$  ( $z>1$ ) (violet),  $C_xH_yO_iN_p^+$  ( $i\geq 0, p\geq 1$ ) (light blue). The mass fractions of  
1125 the four fragment groups are presented by pie-charts.



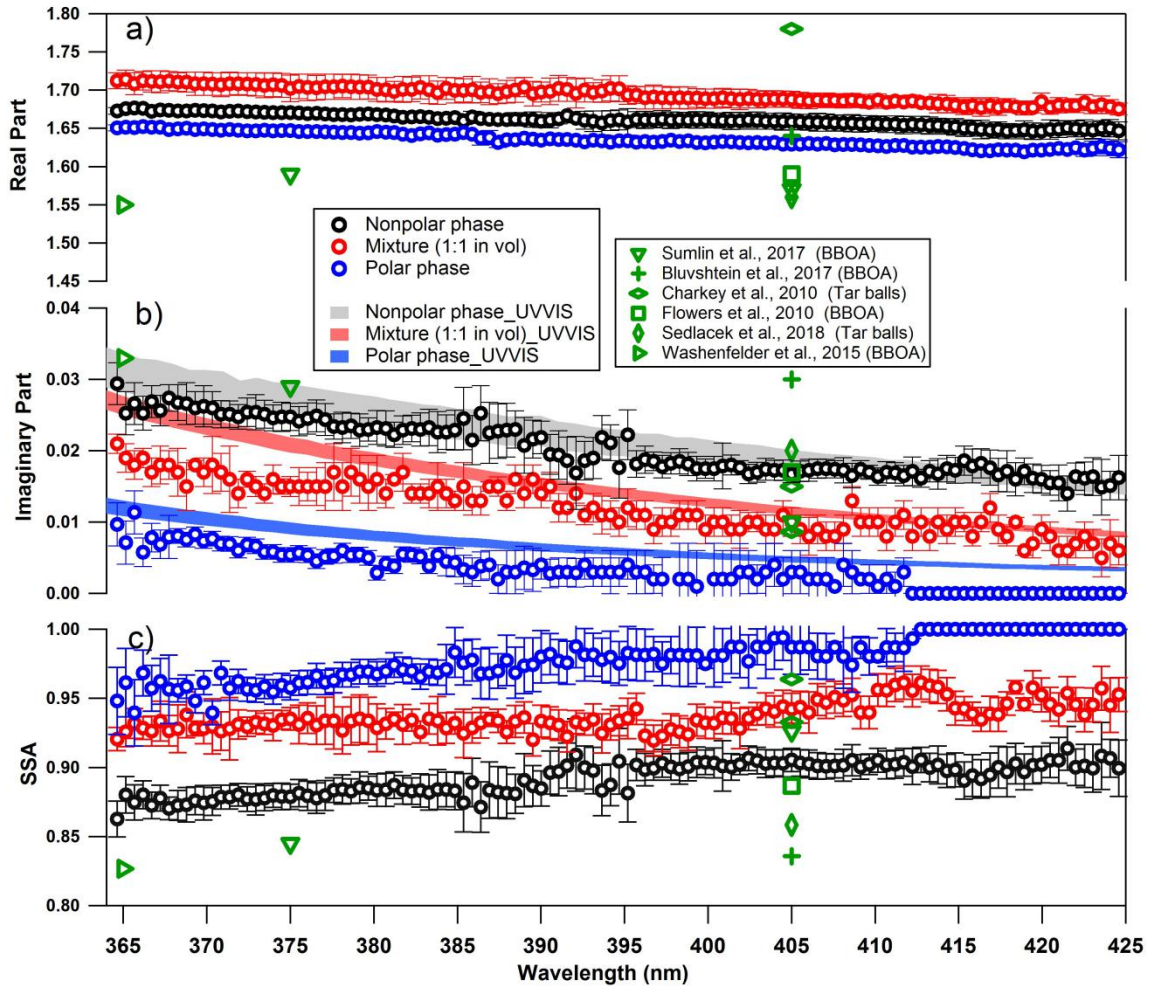
1126

1127 **Figure 3.** LD-REMPI mass spectra of exemplary single tar ball particles, some feature peaks were identified and labeled. a)

1128 Nonpolar tar ball spectra shows predominantly alkyl-substituted and unsubstituted PAHs. b) Polar tar ball spectra reveals many

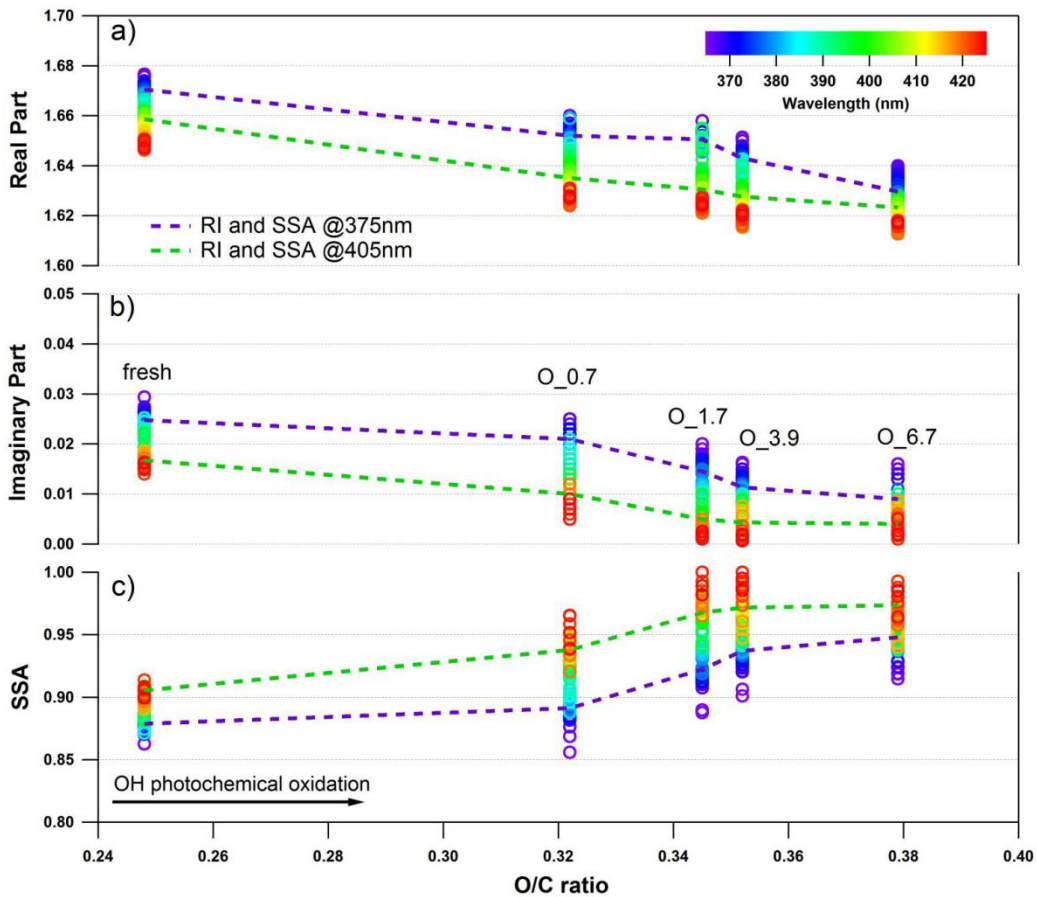
1129 oxidized aromatics, e.g., methoxy-phenol, benzenediol. Note the softwood combustion marker retene at  $m/z=234$ , its

1130 characteristic fragments ( $m/z=203, 204, 205, 219$ ) and possible retene derivatives ( $m/z=248, 250$ ).

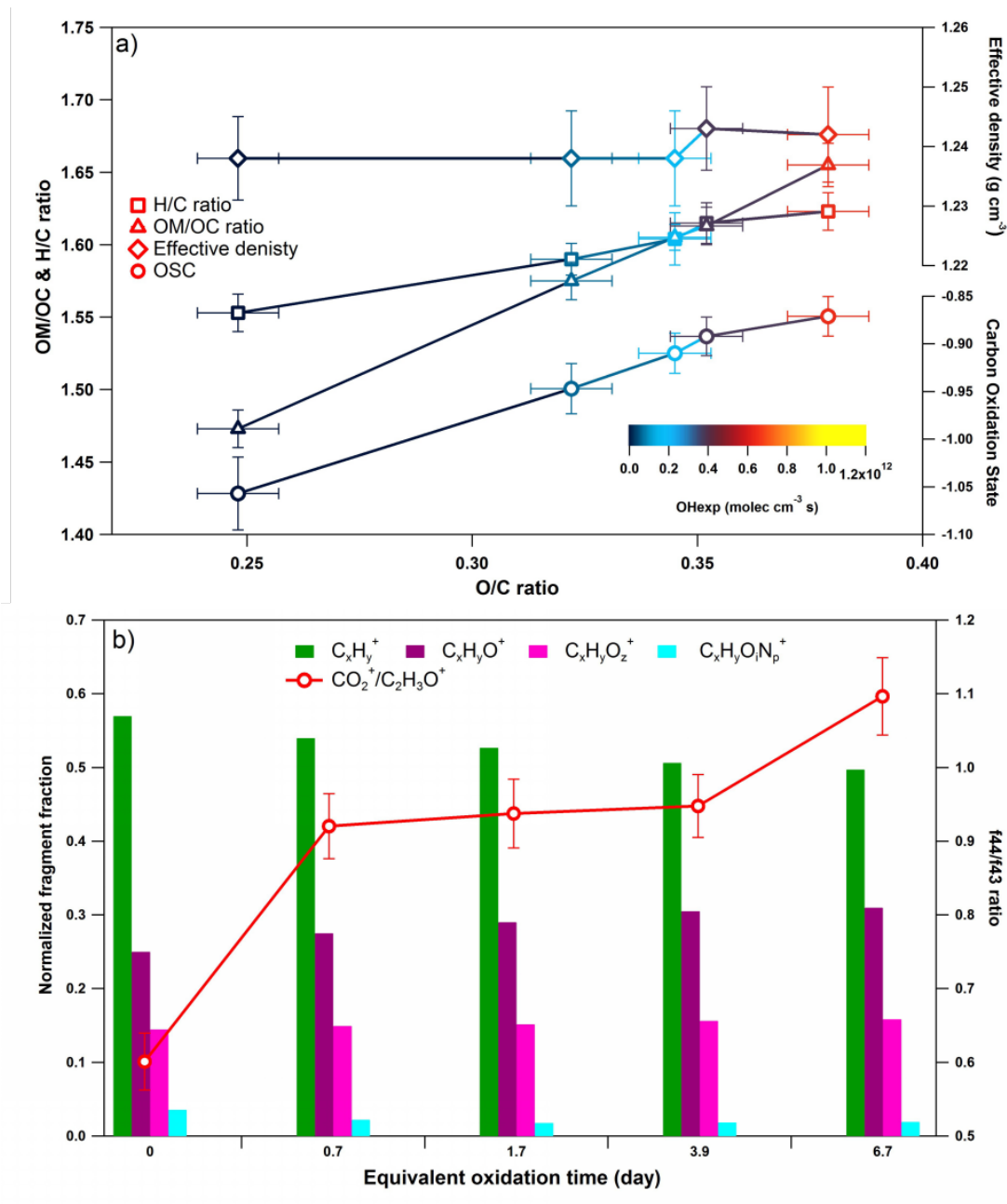


1131

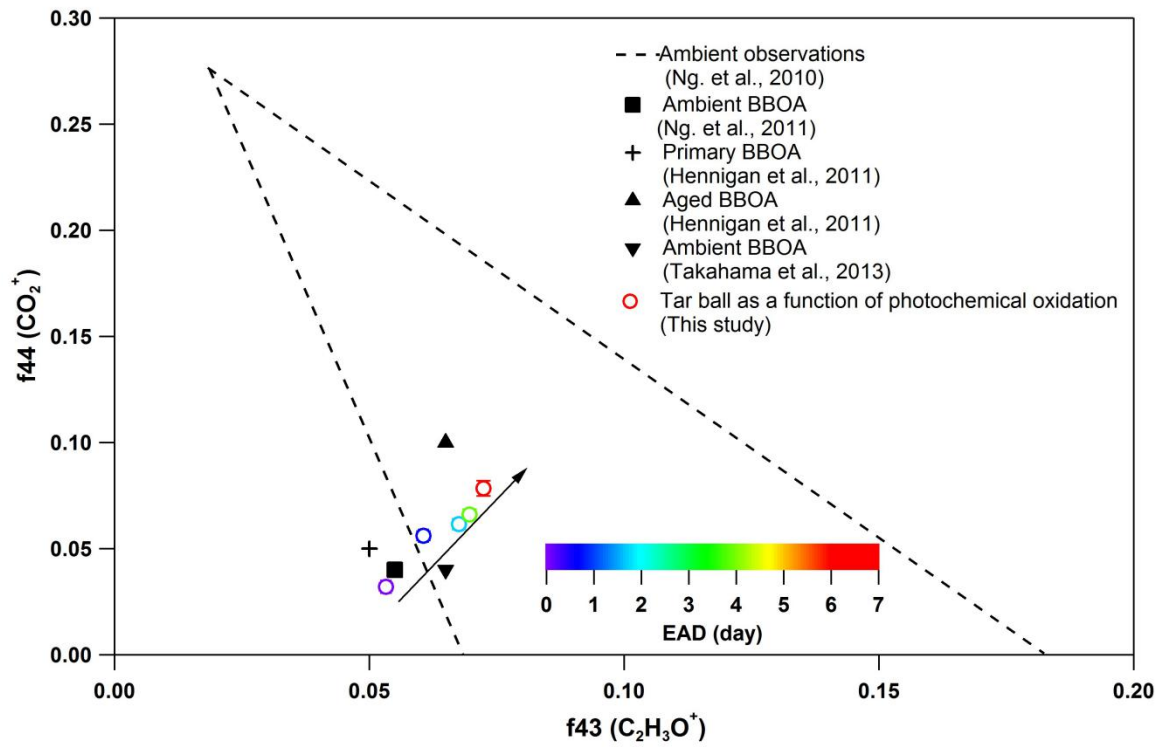
1132 **Figure 4.** Wavelength-dependent RI and SSA for tar ball particles generated from polar, nonpolar and mixture of the two  
 1133 phases tarry solutions (only retrieval for mixture of 1:1 in vol. is shown for clarity, optical results for the rest two mixtures can  
 1134 be found in supporting materials). The shaded areas indicate the upper and lower limits of the imaginary part calculated from  
 1135 UV-VIS spectra of methanol extracts from the corresponding tar ball particles samples: a) real part, b) imaginary part, and c)  
 1136 SSA calculated for 150 nm particles. Overplayed in green symbol are previous measurements of biomass burning from the  
 1137 literature.



1138 **Figure 5.** Evolution of the retrieved wavelength-dependent complex RI and SSA as a function of O:C ratio for tar ball particles  
 1139 upon OH photochemical oxidation: a) real part, b) imaginary part, and c) SSA calculated for 150 nm particles. The color scale  
 1140 shows the span in the RI for the wavelengths measured from 365 to 425 nm. For clarity, error bars for O:C ratio ( $\pm 0.01$ ), RI  
 1141 ( $\pm 0.007$  for real part, and  $\pm 0.003$  for imaginary part on average), and SSA ( $\pm 0.006$ ) are not shown. Two dashed lines trace the  
 1142 RI and SSA at 375 nm (purple) and 405 nm (green). O<sub>0.7</sub>–O<sub>6.7</sub> represent equivalent atmospheric photochemical oxidation  
 1143 for 0.7 and up to 6.7 days.

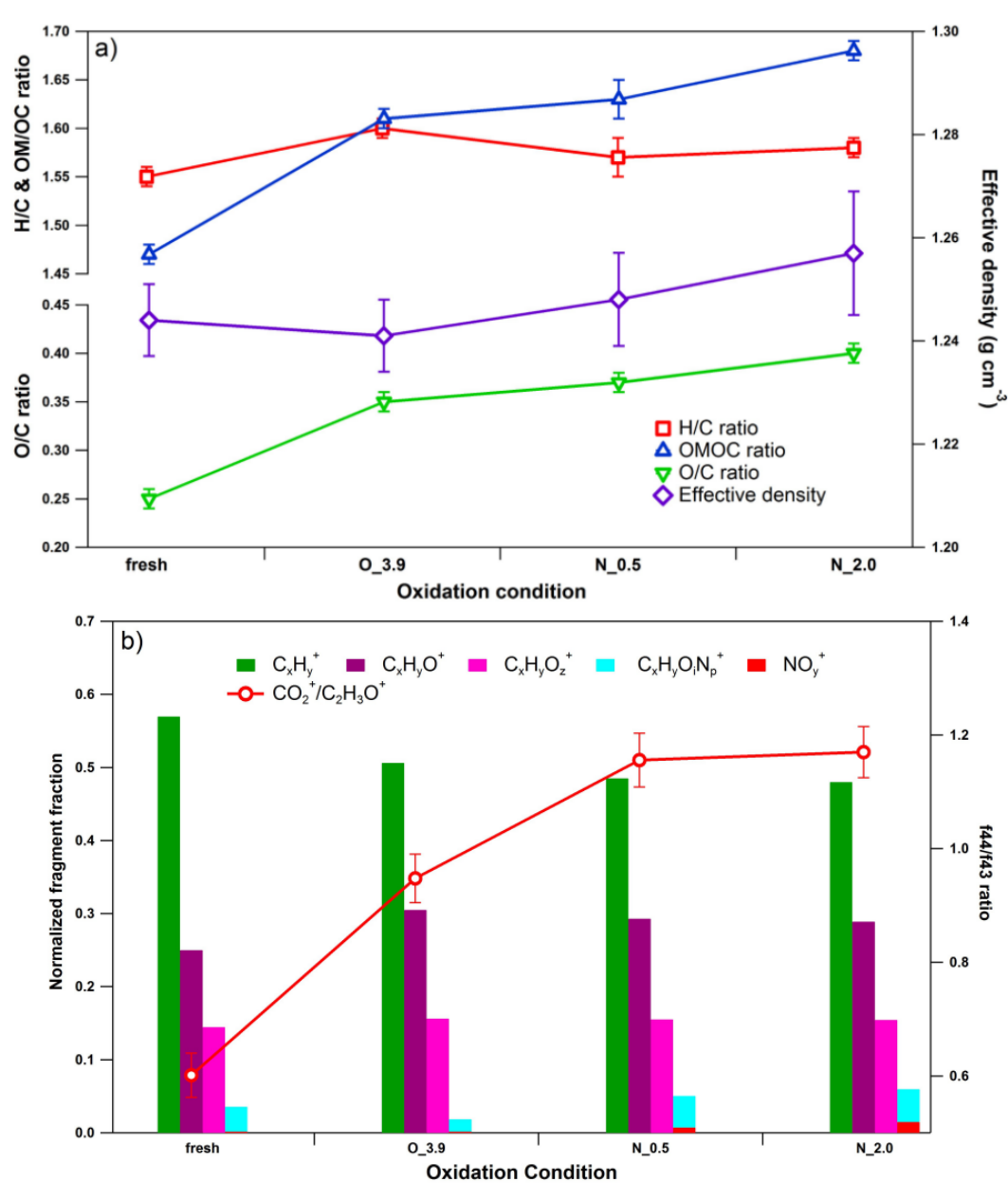


1144 **Figure 6.** Dynamic changes for the chemical characteristics of tar ball particle under NOx-free OH photochemical oxidation:  
 1145 a) OM/OC, H:C ratio, particle density, and average carbon oxidation state ( $\overline{OSC}$ ) changes as a function of O:C ratio; b) mass  
 1146 spectra evolution with oxidation times in term of  $C_xH_y^+$ ,  $C_xH_yO^+$ ,  $C_xH_yO_z^+$ , and  $C_xH_yO_iN_p^+$  fragment groups.

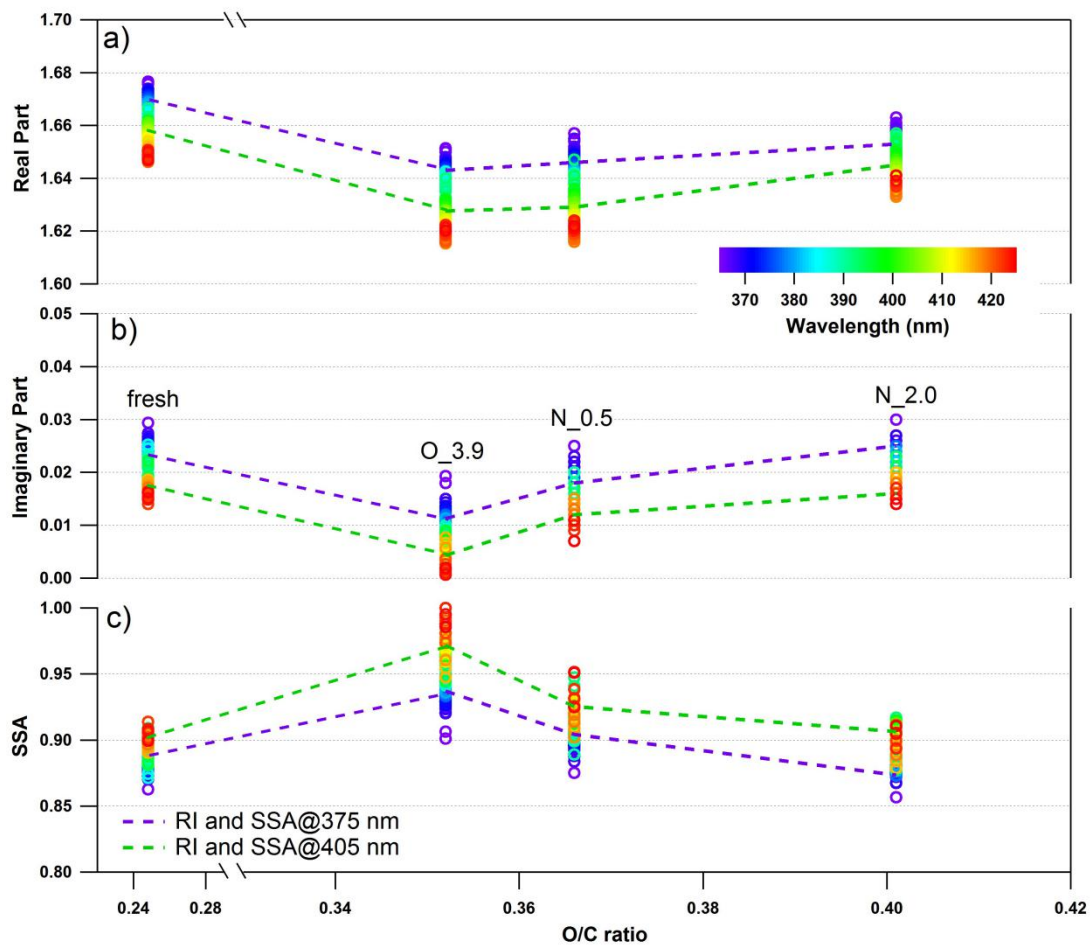


1147

1148 **Figure 7.** Comparison of f44 and f43 values from ambient data sets (Ng. et al., 2010) and values from ambient biomass burning  
 1149 organic aerosol. The hollow circles present tar ball result in this work, and color legend indicate equivalent atmospheric  
 1150 oxidation days, black arrow more clearly shows the extent of NO<sub>x</sub>-free photochemical oxidation in this study.

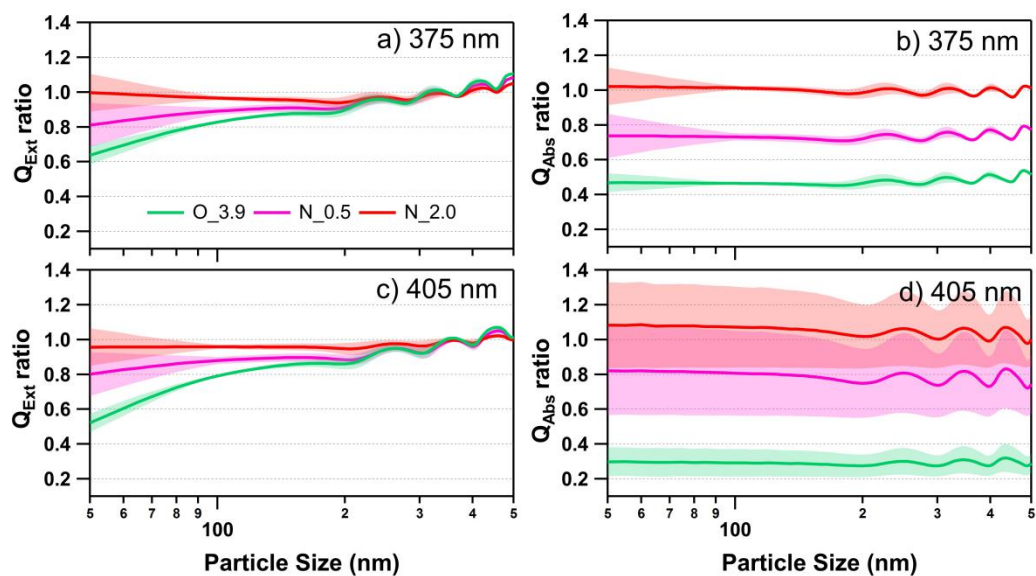


1151 **Figure 8.** Dynamic changes for chemical characteristics of tar ball aerosols under NO<sub>x</sub>-dependent OH photochemical oxidation:  
 1152 a) OM/OC, O:C, H:C, and particle density changes; b) mass spectra changes with different oxidation conditions in term of  
 1153 C<sub>x</sub>H<sub>y</sub><sup>+</sup>, C<sub>x</sub>H<sub>y</sub>O<sup>+</sup>, C<sub>x</sub>H<sub>y</sub>O<sub>2</sub><sup>+</sup>, and C<sub>x</sub>H<sub>y</sub>O<sub>z</sub>N<sub>p</sub><sup>+</sup> fragment groups. C<sub>x</sub>H<sub>y</sub>O<sub>z</sub>N<sub>p</sub><sup>+</sup> include all nitrogen-containing fragments, (e.g.,  
 1154 C<sub>x</sub>H<sub>y</sub>ON<sup>+</sup>, C<sub>x</sub>H<sub>y</sub>O<sub>2</sub>N<sub>i</sub><sup>+</sup>, C<sub>x</sub>H<sub>y</sub>N<sup>+</sup>, etc.), NO<sub>y</sub><sup>+</sup> include NO<sup>+</sup> and NO<sub>2</sub><sup>+</sup>. O\_3.9 represents 3.9 days equivalent atmospheric  
 1155 photochemical aging in absence of NO<sub>x</sub>, N\_0.5 and N\_2.0 indicate photochemical oxidation with 0.5 and 2.0 vol.% N<sub>2</sub>O  
 1156 addition at ~4.0 days atmospheric oxidation.



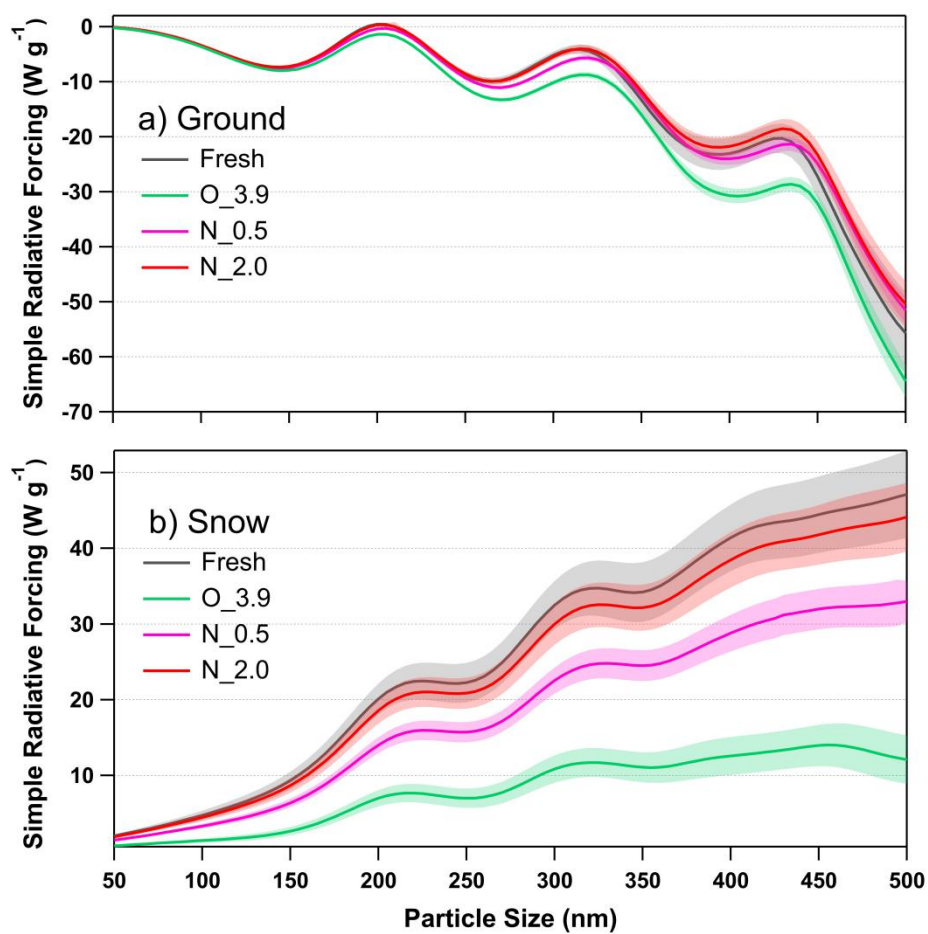
1157

1158 **Figure 9.** Changes of retrieved spectra-dependent RI as a function of O:C ratio for tar ball particles upon NO<sub>x</sub>-dependent  
 1159 photochemical oxidation: a) real part, b) imaginary part, and c) SSA calculated from 150 nm particles. For clarity, error bars  
 1160 for O:C ratio ( $\pm 0.01$ ), RI ( $\pm 0.006$  for real part, and  $\pm 0.003$  for imaginary part on average), and SSA ( $\pm 0.007$ ) are not  
 1161 shown. O\_3.9 represents 3.9 days equivalent atmospheric photochemical aging in absence of NO<sub>x</sub>, N\_0.5 and N\_2.0 indicate  
 1162 photochemical oxidation with 0.5 and 2.0 vol.% N<sub>2</sub>O addition at  $\sim 4.0$  days atmospheric oxidation.



1163

1164 **Figure 10.** Size-resolved light extinction and absorption efficiency ratio of NO<sub>x</sub>-dependent photooxidized tar balls compared  
 1165 to the fresh tar ball particles: a) and c) extinction ratios at 375 and 405 nm, b) and d) absorption ratios at 375 and 405 nm.  
 1166 O<sub>3.9</sub> represents 3.9 days equivalent atmospheric photochemical aging in absence of NO<sub>x</sub>, N<sub>0.5</sub> and N<sub>2.0</sub> indicate  
 1167 photochemical oxidation with 0.5 and 2.0 vol.% N<sub>2</sub>O addition at ~4.0 days atmospheric oxidation.



1168

1169 **Figure 11.** Calculated size-resolved simple radiative forcing (SRF, W g<sup>-1</sup>) by tar ball aerosols, integrated over  
 1170 365~425 nm incident solar irradiation for fresh and NO<sub>x</sub>-dependent photooxidized tar balls: a) ground-based  
 1171 radiative forcing, b) snow-based radiative forcing.

1 **Supporting Information for**

2

3 **Dynamic changes of optical and chemical properties of tar ball aerosols**  
4 **by atmospheric photochemical aging**

5 | Chunlin Li,<sup>†</sup> Quanfu He,<sup>†</sup> Julian Schade,<sup>‡</sup> Johannes Passig,<sup>‡,§</sup> Ralf Zimmermann,<sup>‡,§</sup> [Daphne Meidan,<sup>†</sup>](#)  
6 Alexander Laskin,<sup>§</sup> and Yinon Rudich<sup>†,\*</sup>

7 <sup>†</sup>Department of Earth and Planetary Sciences, Weizmann Institute of Science, Rehovot 76100, Israel

8 <sup>‡</sup>Joint Mass Spectrometry Centre, University of Rostock, Dr.-Lorenz-Weg 2, 18059 Rostock, Germany

9 <sup>§</sup>Joint Mass Spectrometry Centre, Cooperation Group 'Comprehensive Molecular Analytics' (CMA), Helmholtz Zentrum  
0 München, Ingolstädter Landstrasse 1, 85764 Neuherberg, Germany

1 <sup>§</sup>Department of Chemistry, Purdue University, West Lafayette, Indiana 47907, United States

2

3 *Correspondence to:* Yinon Rudich (yinin.rudich@weizmann.ac.il)

4

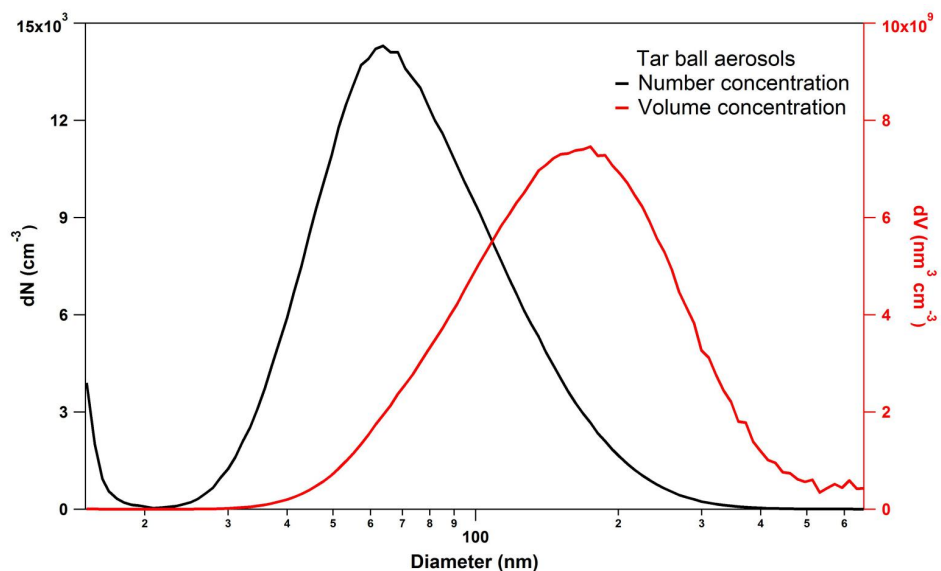
5  
6  
7  
8  
9  
0  
1  
2  
3  
4  
5  
6  
7  
8  
9  
0  
1  
2  
3  
4  
5  
6  
7  
8  
9  
0  
1  
2  
3  
4  
5  
6  
7

## Contents

1. Tar ball aerosol size distribution at downstream of the OFR (Figure S1)
2. OC-EC content of fresh polar and nonpolar tar ball aerosols
3. Fresh tar ball composition from HR-ToF-AMS measurement (Figure S2)
4. Summary of fresh tar ball particles chemical elemental ratios and effective densities (Table S1)
5. Aerodynamic size distribution for tar ball particles measured by SP-LD-REMPI-ToF-MS (Figure S3)
6. Exemplary aromatic compounds indicated by the mass spectra in Figure 3 (All listed substances are typical compounds in wood combustion emissions, Table S2)
7. Morphology of tar ball aerosols (Figure S4)
8. Refractive index for tar ball at mixture of 2:1 and 1:2 in volume of polar and nonpolar materials (Figure S5)
9. Example of absorption coefficients for some of the most absorbing PAHs identified in BBOA (Figure S6)
10. Methanol extractable BrC mass absorption cross sections (MAC) for fresh tar ball aerosols from 360 to 450 nm (Figure S7)
11. Mixing rules prediction for nonpolar-polar mixed tar ball aerosols (Figure S8-S12, Table S3-S4)
12. Summary of optical parameters for tar ball upon NO<sub>x</sub>-dependent photochemical aging (Table S5)
13. Methanol extractable BrC mass absorption cross sections (MAC) for NO<sub>x</sub>-free photochemical aged tar ball aerosols from 360 to 450 nm (Figure S13)
14. Optical and chemical changes for tar ball aerosols due to photolysis from UV light irradiation in the OFR (Table S6-S7, Figure S14-S17)
15. Optical and chemical changes of tar ball aerosols due to O<sub>3</sub> oxidation in the OFR (Figure S18-S19)
16. Mass spectra characters and effective density changes for tar ball particles upon photochemical oxidation (Table S8)
17. Detailed mass spectra changes for tar ball aerosols upon 6.7 EAD photochemical aging (Figure S20)
18. Standard AMS spectra for inorganic salt of NH<sub>4</sub>NO<sub>3</sub> (Figure S21)
19. Detailed mass spectra changes for tar ball aerosols upon 4 EAD photochemical aging with 2.0 vol.% N<sub>2</sub>O addition (Figure S22)
20. Methanol extractable BrC mass absorption cross section (MAC) for tar ball aerosols upon various NO<sub>x</sub>-dependent photochemical aging processes (Figure S23)
21. Particle size- and light wavelength-resolved radiative forcing for tar ball aerosols oxidized via various NO<sub>x</sub>-dependent oxidation processes (Figure S24-S25)

8 **1. Tar ball aerosol size distribution at downstream of the OFR**

9 Tar ball particles were generated via TSI atomizer, and concentration of tar ball particles was mediated in the OFR before these  
0 aerosols being photochemically oxidized. Polar, nonpolar, and mixture tar ball particles present similar size distributions.



1

2 **Figure S1.** Size distribution of laboratory generated tar ball aerosols at downstream of the OFR. The distribution presents a  
3 narrow range with a single peak at ~70 nm diameter, similar to the size distribution of practical tar balls obtained from the  
4 wildfires and domestic biofuel burning (Pósfai et al., 2004; Chakrabarty et al., 2010).

## 2. OC-EC content of fresh polar and nonpolar tar ball aerosols

Non-refractory organic carbon (OC) and refractory elemental carbon (EC) in fresh tar ball aerosols were analyzed using a DRI Model 2015 multi-wavelength thermal/optical carbon analyzer (Desert Research Institute, Nevada, USA) with the IMPROVE A protocol (Chow et al., 2011; Li et al., 2018). In details, fresh nonpolar and polar tar balls were collected onto pretreated quartz filters (Whatman, Mainstone, UK, baked over 450 °C for 6 hr to eliminate any contamination), a circular punch (0.8 cm in diameter) of each loaded filter including operational blank filter was taken and analyzed. Four OC fractions (OC1, OC2, OC3, and OC4 correspond to gradient cutting temperature at 140, 280, 480, and 580 °C, respectively, in a helium atmosphere), three EC fractions (EC1, EC2, EC3 with cutting temperature of 590, 780, and 840 °C, respectively, in a 2% oxygen/98% helium atmosphere), and one PC fraction (pyrolyzed carbon content determined when transmitted laser returned to its original intensity after the sample was exposed to oxygen) were determined for each sample, and  $OC=OC1+OC2+OC3+OC4+PC$ ,  $EC=EC1+EC2+EC3-PC$ , total carbon (TC) equals the sum of OC and EC. The blank-corrected and normalized carbon fractions for fresh tar ball aerosols were given below:

Tar ball	OC1	OC2	OC3	OC4	PC	EC1	EC2	EC3	OC	EC
Polar	38.8%	32.2%	18.4%	0.0%	10.6%	10.6%	0.0%	0.0%	100.0%	0.0%
Nonpolar	28.7%	25.8%	16.0%	7.7%	21.1%	21.7%	0.0%	0.0%	99.3%	0.7%

It is clear EC content was almost below detection limit for both polar- and nonpolar-tar balls, the slight EC fraction in nonpolar tar ball is less than 0.7% of TC content and resides in EC1, which can be termed as non-refractory char-EC, empirically defined as  $EC1-PC$ . Char-EC is stripped from some OC under oxygen-free heating during OC/EC measurement, which has much weak absorption, and thus can be distinguished as brown carbon rather than black carbon (Andreae and Gelencsér, 2006; Arora et al., 2015; Kim et al., 2011; Han et al., 2008, 2009). Many other studies on biomass burning emissions from wildfires and domestic burning have also reported negligible EC content in tar ball aerosols (Chakrabarty et al., 2010; Tivanski et al., 2007; Hand et al., 2005; China et al., 2013).

Formatted

3. Fresh tar ball composition from HR-ToF-AMS measurement

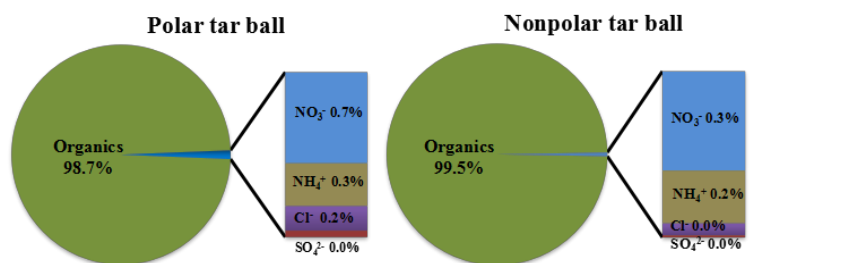


Figure S2. Fresh polar and nonpolar tar balls composition from HR-ToF-AMS measurement. Color mapping: organics-green, nitrates-blue, ammonium-yellow, chloride-purple, sulfates-red.

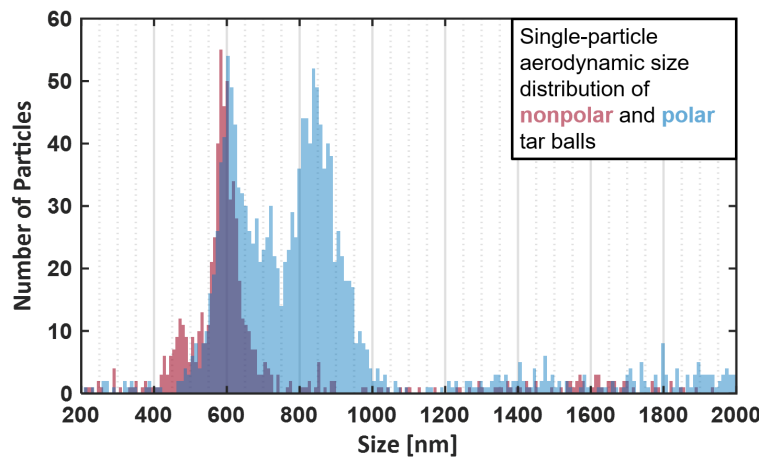
8 4. Organic elemental ratios for fresh tar ball aerosols were derived from AMS measurement at W mode, and effective  
 9 densities of tar ball aerosols were calculated from aerodynamic diameter divided by mobility diameter assuming tar ball  
 0 with sphericity of 1.0

1 Table S1. Summary of fresh tar ball particles chemical elemental ratios and effective densities

BBOA	Mass spectra			Density (g cm <sup>-3</sup> )	Reference
	O:C	H:C	M/z>100 fraction		
Nonpolar	0.25±0.01	1.55±0.01	0.32	1.24±0.01	this work
Mixture (2:1 in vol.)	0.30±0.01	1.59±0.02	0.29	1.27±0.02	
Mixture (1:1 in vol.)	0.36±0.01	1.62±0.04	0.27	1.29±0.02	
Mixture (1:2 in vol.)	0.39±0.01	1.61±0.03	0.24	1.30±0.01	
Polar	0.44±0.02	1.64±0.03	0.15	1.33±0.02	
BBOA	0.3–0.4				Aiken et al., 2008
BBOA	0.29–0.33	1.51–1.58			Li et al., 2012
BBOA	0.18–0.26	1.4–1.5			He et al., 2010
BBOA	0.15–0.7	1.5–1.6	0.11–0.20	1.4	Zhou et al., 2017
BBOA				1.5	Sedlacek III et al., 2018
BBOA	0.33	1.90		1.18–1.19	Sumlin et al., 2017; 2018

2

3 5. Aerodynamic size distribution for tar ball particles measured by SP-LD-REMPI-ToF-MS



4

5 **Figure S3.** Particle aerodynamic size distributions for fresh nonpolar (red) and polar (blue) tar ball aerosols measured via laser  
6 velocimetry by the SP-LD-REMPI-ToF-MS instrument. The major mode peaks at about 550 nm for both particle classes while a  
7 second mode of larger particles occurs for polar tar balls and a second mode of smaller particles appears for nonpolar tar balls.  
8 Note that the detection efficiency drops rapidly below 250 nm due to the descending Mie scattering efficiency for particles much  
9 smaller than the wavelength (532 nm).

6. Exemplary **Proper** Polyaromatic Compounds indicated by the REMPI PAH Spectra in this study (Table S2)

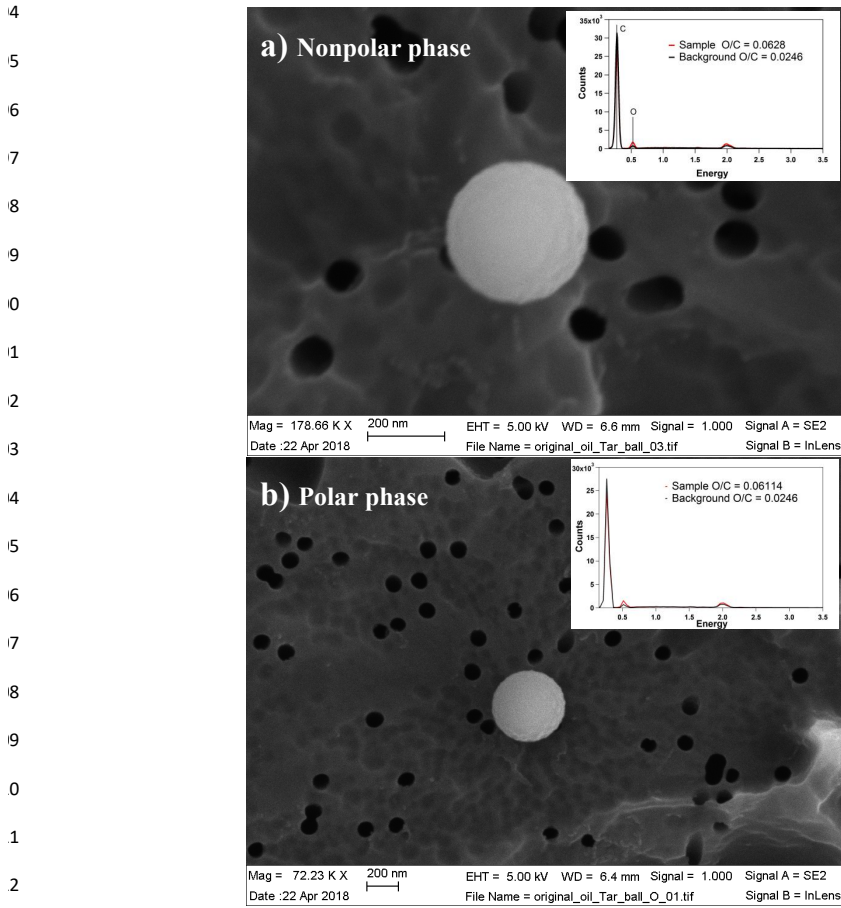
Table S2. Exemplary **proper** (poly)aromatic compounds indicated by the REMPI PAH Spectra in Figure 3

m/z	Name	Formula	Polar tar ball	Nonpolar tar ball	BBOA Reference
110	Catechol	C <sub>6</sub> H <sub>6</sub> O <sub>2</sub>	√		Veres et al., 2010; Yee et al., 2013
115	PAHs fragments		√	√	Adler et al., 2011; Bruns et al., 2015
124	Guaiacol	C <sub>7</sub> H <sub>8</sub> O <sub>2</sub>	√		Li et al., 2017; Yee et al., 2013; Hoffmann et al., 2007
128	Naphthalene	C <sub>10</sub> H <sub>8</sub>	√	√	Samburova et al., 2016; Passig et al., 2017; Bruns et al., 2015
138	4-Methylguajacol	C <sub>8</sub> H <sub>10</sub> O <sub>2</sub>	√	√	Adler et al., 2011; Yee et al., 2013
152	Vanillin 4-Ethylguajacol	C <sub>8</sub> H <sub>8</sub> O <sub>3</sub> C <sub>9</sub> H <sub>12</sub> O <sub>2</sub>	√	√	Li et al., 2014; Passig et al., 2017; Yee et al., 2013; Hoffmann et al., 2007
158	Methoxynaphthalene 1,4-Naphthalenedione Methylnaphthol	C <sub>11</sub> H <sub>10</sub> O C <sub>10</sub> H <sub>6</sub> O <sub>2</sub> C <sub>11</sub> H <sub>10</sub> O	√		Santos et al., 2016; Yee et al., 2013; Hoffmann et al., 2007
165	PAHs fragments		√	√	Adler et al., 2011; Bruns et al., 2015
168	4-Methylsyringol Vanillic acid	C <sub>9</sub> H <sub>12</sub> O <sub>3</sub> C <sub>8</sub> H <sub>8</sub> O <sub>4</sub>	√		Santos et al., 2016; Hoffmann et al., 2007; Bruns et al., 2015
178	Phenanthrene Conifery aldehyde	C <sub>14</sub> H <sub>10</sub> C <sub>10</sub> H <sub>10</sub> O <sub>3</sub>	√	√	Samburova et al., 2016; Bente et al., 2008, 2009; Passig et al., 2017
182	Syringaldehyde 4-Ethylsyringol	C <sub>9</sub> H <sub>10</sub> O <sub>4</sub> C <sub>10</sub> H <sub>14</sub> O <sub>3</sub>	√		Santos et al., 2016; Yee et al., 2013; Hoffmann et al., 2007
189, 190, 191	Retene fragments		√	√	Bente et al., 2008, 2009; Mandalakis et al., 2005
192	Methylphenanthrene	C <sub>15</sub> H <sub>12</sub>	√	√	Samburova et al., 2016; Bente et al., 2008, 2009; Passig et al., 2017
202	Pyrene Fluoranthene	C <sub>16</sub> H <sub>10</sub>	√	√	Adler et al., 2011; Bente et al., 2008, 2009; Passig et al., 2017
203, 204, 205	Retene fragments		√	√	Passig et al., 2017; Mandalakis et al., 2005
206	Ethylphenanthrene	C <sub>16</sub> H <sub>14</sub>		√	Samburova et al., 2016
219, 220	Retene fragments		√	√	Bente et al., 2008, 2009; Passig et al., 2017
234	Retene	C <sub>18</sub> H <sub>18</sub>	√	√	Samburova et al., 2016; Bente et al., 2008, 2009; Passig et al., 2017

248	Methyl. Retene	C <sub>19</sub> H <sub>20</sub>		√	Passig et al., 2017; Mandalakis et al., 2005
250	Ox. Retene	C <sub>18</sub> H <sub>18</sub> O	√	√	Samburova et al., 2016

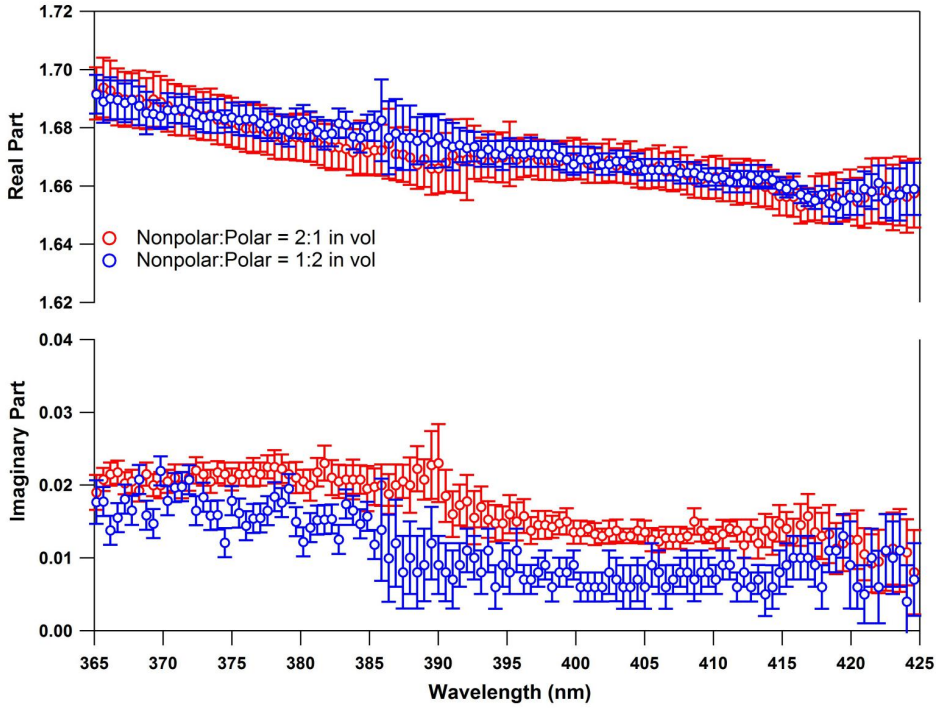
Note: only some major and most proper aromatic compounds were listed in the table

3 **7. Morphology of tar ball aerosols**



4 **Figure S4.** Morphology of fresh tar ball particles generated from polar and nonpolar phase tarry solutions. The particles are  
5 perfect spherical and amorphous in internal composition.

6 8. Refractive index for tar ball at mixture of 2:1 and 1:2 in volume of polar and nonpolar materials



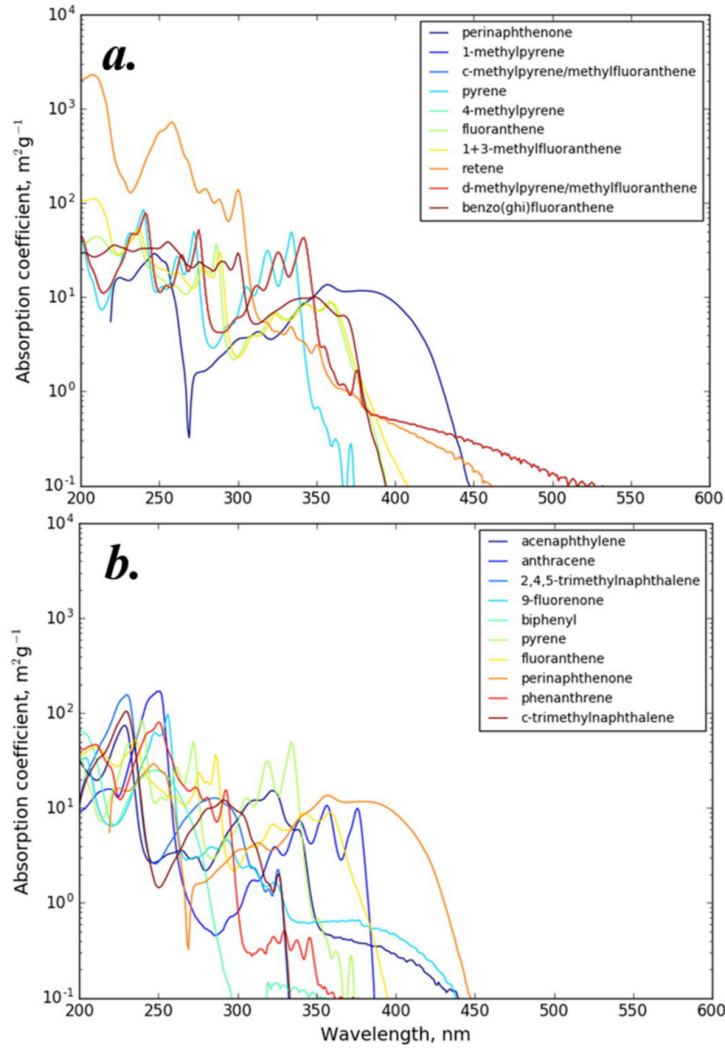
7

8 Figure S5. Wavelength-dependent refractive index (RI) for tar ball particles generated from polar and nonpolar phase solution mixtures

9

0

1 9. Example of absorption coefficients for some of the most absorbing PAHs identified in BBOA



2  
3 **Figure S6.** Absorption coefficients for some of the most absorbing PAHs identified in biomass burning emissions (Samburova et  
4 al., 2016).  
5

10. Methanol extractable BrC mass absorption cross sections (MAC) for fresh tar ball aerosols from 360 to 450 nm

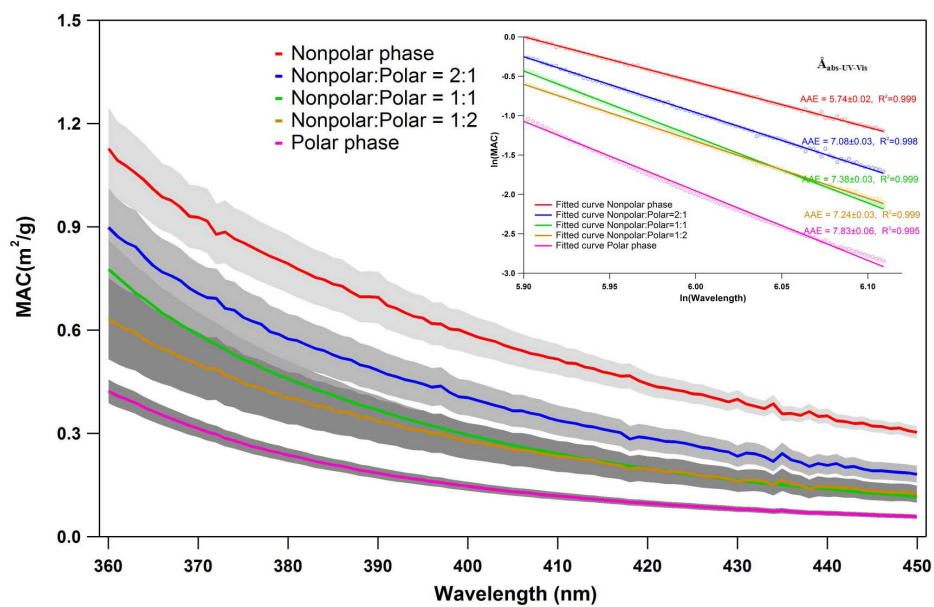


Figure S7. BrC mass absorption cross section (MAC) for methanol extracted fresh tar ball particles. Inset chart presents example of  $\hat{A}_{\text{abs\_UV-vis}}$  calculated from natural logarithm regression of MAC and wavelength.

## 11. Prediction of mixture tar ball optical properties based on different mixing rules

There are many mixing rules currently in use to predict optical properties of aerosol from matrix of various substances: 1) molar refraction and absorption (Jacobson, 2002; Tang, 1997); 2) a volume-weighted linear average of the refractive indices (d'Almeida et al., 1991); 3) the Maxwell-Garnet rule (Chýlek et al., 1984); and 4) the dynamic effective medium approximation (Jacobson, 2006). Due to the complexity of undefined chemical composition of tar ball particles, the Maxwell-Garnet and dynamic effective medium approximation are not feasible in this study, therefore, the simple molar fraction and volume-weighted mixing rules were discussed to fit the optical results.

The "linear mixing rule" simplifies mixing state and interaction between matrix, assumes that total real and imaginary refractive indices of the mixture are result of the indices of the components weighted by their their volume fractions:

$$\begin{aligned}n_{tot} &= \sum_n f_i n_i \\k_{tot} &= \sum_n f_i k_i\end{aligned}\quad [1]$$

Where  $f_i$ ,  $n_i$ , and  $k_i$  are the volume fraction, real part, and imaginary part of each component

The molar fraction mixing rule assumes that the total molar refraction of a mixture is given by the linear average of the molar refraction of each component weighted by their molar volumes, i.e.,

$$\begin{aligned}\frac{\bar{M}}{\rho} \frac{n^2 - 1}{n^2 + 2} &= \sum_n \chi_i \frac{M_i}{\rho_i} \frac{n_i^2 - 1}{n_i^2 + 2} \\ \frac{\bar{M}}{\rho} k &= \sum_n \chi_i \frac{M_i}{\rho_i} k_i \\ \sum_n \chi_i &= 1\end{aligned}\quad [2]$$

Where  $\chi_i$ ,  $M_i$ , and  $\rho_i$  are the molar fraction, molecular weight, and material density.

Refractive indices for tar ball generated from polar and nonpolar fraction mixture at solution mixing ratios of 1:2, 1:1, and 2:1 will be calculated from RI of polar and nonpolar optical results based on above two rules. The exact volume and molar fraction for bulk polar and nonpolar part in particles can be estimated from particle density and chemical elemental ratios:

$$\begin{aligned}\rho_{tot} &= f_1 \rho_1 + f_2 \rho_2 \\ f_1 + f_2 &= 1\end{aligned}\quad [3]$$

$$\begin{aligned}R_{O/C} &= \chi_1 R_{O/C_1} + \chi_2 R_{O/C_2} \\ \chi_1 + \chi_2 &= 1\end{aligned}\quad [4]$$

Where  $R_{O/C}$  is oxygen to carbon ratio from AMS measurement of tar ball particles, and calculated particulate volume and molar fraction are given below:

3 **Table S3.** Particulate molar and volume fractions of bulk polar and nonpolar tar

Polar:Nonpolar prepared solution ratio	O/C molar ratio	O/C retrieved molar mixing ratio	Density (g cm <sup>-3</sup> )	density retrieved volume mixing ratio
1:0	0.44	1:0	1.329±0.021	1:0
2:1	0.39	2.8:1	1.298±0.022	1.8:1
1:1	0.36	1.4:1	1.285±0.019	0.98:1
1:2	0.3	1:2.8	1.274±0.013	1:1.72
0:1	0.25	0:1	1.242±0.005	0:1

4

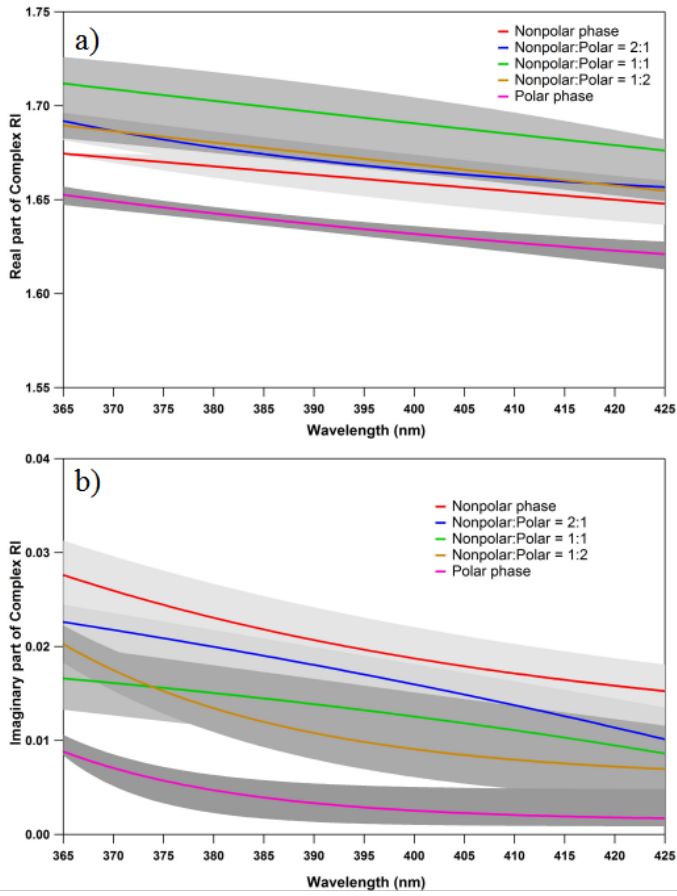
5 Molecular weight for polar and nonpolar fractions were simplified as  $M_{\text{bulk-polar}}$  and  $M_{\text{bulk-nonpolar}}$ , and mixture tar ball particles  
 6 follow the function below:

$$\frac{\bar{M}}{\rho} = \frac{x_1 M_{\text{bulk-polar}}}{\rho_1} + \frac{x_2 M_{\text{bulk-nonpolar}}}{\rho_2} \quad [5]$$

$$\bar{M} = x_1 M_{\text{bulk-polar}} + x_2 M_{\text{bulk-nonpolar}}$$

8 And it was calculated as  $M_{\text{bulk-nonpolar}} \approx 1.3M_{\text{bulk-polar}}$

9 For convenience and clarity, wavelength-dependent RI for tar ball were exponential or power-law fitted, the results were showed  
 10 in Figure S8 and corresponded parameters were summarized in Table S4:



1  
2  
3

Figure S8. Regressed RI for tar ball particles of various mixing ratios: a) real part, and b) imaginary part

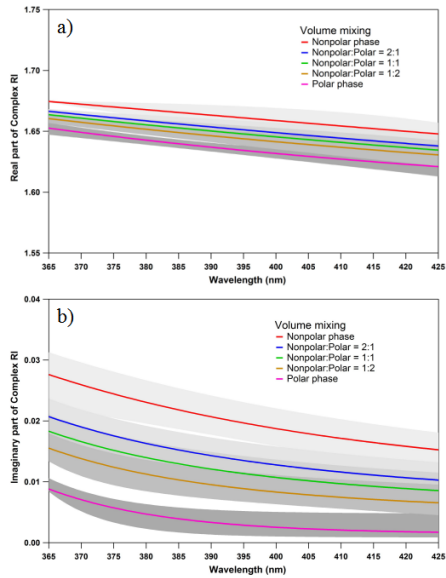
4 **Table S4.** Parameterization of the Wavelength-Dependent (365 to 425 nm) Effective Complex RI of tar ball particles

Tar ball		Real			Imaginary		
		Co	C1	C2	Co	C1	C2
Nonpolar phase	min	1.604	7.148	-1.27E-02	0.164	-8.89E-02	1.27E-03
	average	1.033	0.831	-7.08E-04	0.010	2.37E+01	-1.97E-02
	max	1.677	-1.95E-09	3.80E-02	0.010	8.75E+00	-1.65E-02
Nonpolar:polar 2:1	min	1.627	22.067	-1.65E-02	0.028	-1.05E-05	1.80E-02
	average	1.646	321.800	-2.43E-02	0.046	-1.81E-03	7.06E-03
	max	1.658	2819.637	-3.04E-02	0.330	-2.47E-01	5.86E-04
Nonpolar:polar 1:1	min	1.657	55.140	-1.98E-02	-0.291	3.52E-01	-4.01E-04
	average	1.324	0.697	-1.61E-03	0.023	-5.69E-16	5.10E+00
	max	1.754	-5.09E-18	6.145	-0.220	3.00E-01	-6.09E-04
Nonpolar:polar 1:2	min	1.832	-0.044	3.35E-03	0.002	6.88E+04	-4.19E-02
	average	1.306	0.683	-1.58E-03	0.006	8.43E+04	-4.27E-02
	max	1.550	0.826	-4.75E-03	0.009	1.56E+40	-1.64E+01
Polar phase	min	1.921	-0.133	1.97E-03	0.016	-5.83E-19	6.33E+00
	average	1.585	3.174	-1.06E-02	0.001	3.02E+06	-5.43E-02
	max	1.615	53.051	-1.95E-02	0.005	5.43E+11	-8.81E-02

5 Note: Non-shaded cells were fitted with an exponent;  $n&k(\lambda)=C_0+C_1 \times e^{(C_2 \times \lambda)}$ . Shaded cells were fitted with a power law;

6  $n&k(\lambda)=C_0+ C_1 \lambda^{\times C_2}$

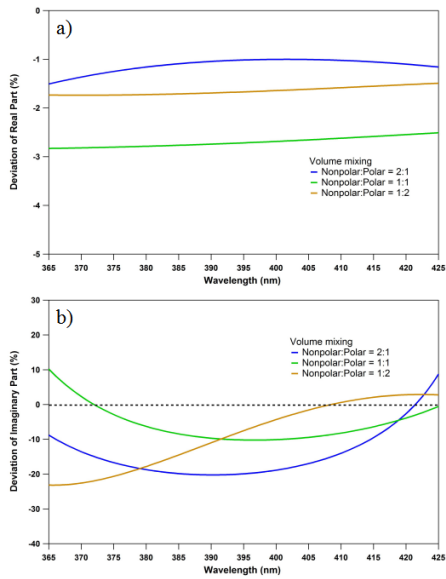
7 The calculated RI following “volume linear mixing rules” for tar ball were presented in Figure S9 and compared with  
8 experimental data in Figure S10.



9

0  
1

**Figure S9.** Estimated RI for tar ball particles of various mixing ratios based on volume linear mixing rule: a) real part, and b) imaginary part

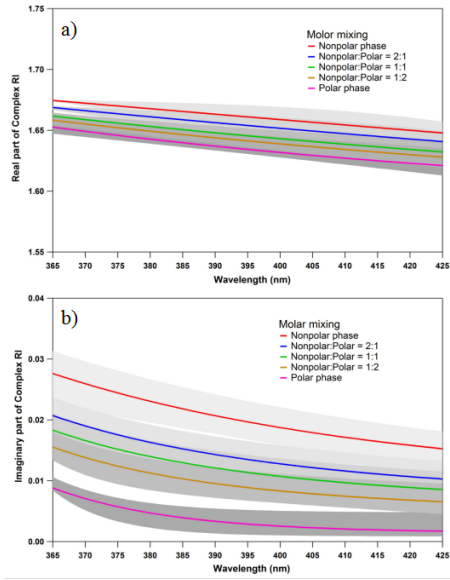


2

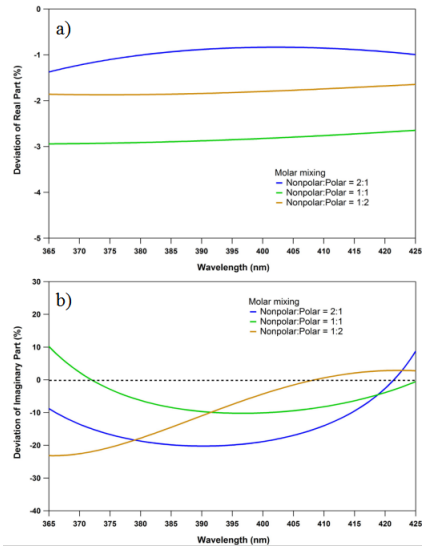
3  
4  
5

**Figure S10.** Deviation between experimental RI and predicted RI from volume linear mixing rule: a) real part, and b) imaginary part

6 The calculated RI following “molar fraction mixing rules” for tar ball were presented in Figure S11 and compared with  
 7 experimental data in Figure S12.



8  
 9 **Figure S11.** Estimated RI for tar ball particles of various mixing ratios based on molar fraction mixing rule: a) real part, and  
 0 b) imaginary part



1  
 2 **Figure S12.** Deviation between experimental RI and predicted RI from molar fraction mixing rule: a) real part, and b)  
 3 imaginary part

## 12. Summary of optical parameters for tar ball aerosol upon NO<sub>x</sub>-dependent photochemical aging

**Table S5.** Summary of RI and Ångström exponent changes for tar ball particles upon photochemical oxidation (mean ± standard deviation)

Tar ball	Complex Refractive index			SSA (average)	Å <sub>abs</sub>	Å <sub>abs_UVVIS</sub>	Å <sub>s</sub>
	Average	375nm	405nm				
Fresh	(1.661±0.008)+(0.020±0.004)i	(1.671±0.003)+(0.025±0.003)i	(1.659±0.011)+(0.017±0.002)i	0.89 ± 0.01	5.87 ± 0.37	6.74	3.81
O_0.7	(1.641±0.010)+(0.014±0.006)i	(1.652±0.001)+(0.021±0.001)i	(1.635±0.001)+(0.010±0.002)i	0.92 ± 0.02	9.33 ± 3.38	6.11	4.21
O_1.7	(1.639±0.011)+(0.008±0.005)i	(1.651±0.002)+(0.015±0.004)i	(1.631±0.002)+(0.005±0.003)i	0.96 ± 0.03	10.96 ± 3.23	6.46	4.33
O_3.9	(1.632±0.010)+(0.007±0.004)i	(1.643±0.001)+(0.011±0.002)i	(1.628±0.002)+(0.004±0.001)i	0.96 ± 0.02	10.63 ± 3.17	6.31	4.11
O_6.7	(1.624±0.007)+(0.007±0.003)i	(1.630±0.003)+(0.009±0.003)i	(1.623±0.002)+(0.004±0.003)i	0.96 ± 0.02	9.89 ± 2.59	6.02	3.74
N_0.5	(1.635±0.011)+(0.015±0.004)i	(1.646±0.001)+(0.018±0.001)i	(1.629±0.001)+(0.012±0.002)i	0.91 ± 0.01	6.92 ± 1.35	6.41	4.01
N_2.0	(1.648±0.008)+(0.019±0.004)i	(1.653±0.002)+(0.025±0.003)i	(1.645±0.002)+(0.016±0.001)i	0.89 ± 0.01	5.60 ± 0.69	6.35	3.76

13. Methanol extractable BrC mass absorption cross sections (MAC) for NO<sub>x</sub>-free photochemical aged tar ball aerosols from 360 to 450 nm

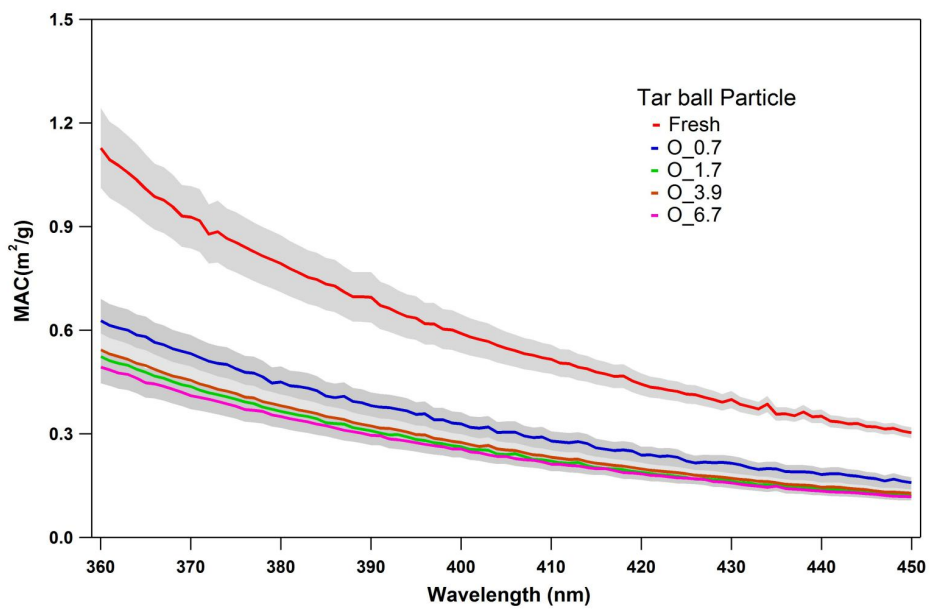


Figure S13. Diminishing in tar ball BrC mass absorption cross section (MAC) upon daytime NO<sub>x</sub>-free photochemical oxidation

#### 14. Optical and chemical changes for tar ball aerosols due to photolysis from UV light irradiation in the OFR

Studies have reported that BrC formation and SOA decomposition due to directly UV/near UV-short visible light irradiation of various precursors in both liquid and air (Bateman et al., 2011; Malecha and Nizkorodov, 2016; Wong et al., 2017). During photochemical aging through the OFR at residence time of 144s, tar ball particles were also exposed to high photon flux at 254 nm. We performed several experiments to estimate the influence of UV illumination on tar ball evolution. Irradiation tests of P1 and P2 repeated the same aging process of O\_1.7 and O\_3.9 without external O<sub>3</sub>, and P3 was conducted at a full power of the UV lamps in the OFR. We observed slight chemical composition changes in the tar ball aerosols due to photolysis, as the O/C ratio continuously increased while H/C decreased with extension of irradiation (Table S6 and Figure S14). The O/C ratio increased by 0.04 for maximal irradiation exposure, which was much smaller than that from photochemical oxidation. This indicates that OH-initiated oxidation rather than photolysis reactions play a more dominant role in tar ball aging.

The decrease of the H/C ratio due to photolysis exhibited a distinct different chemical pathway than by OH photooxidation. According to the mass spectra analysis, particularly for the P3 experiment shown in Figure S14, the fractions of signals attributed to C<sub>x</sub>H<sub>y</sub><sup>+</sup> and C<sub>x</sub>H<sub>y</sub>O<sub>z</sub><sup>+</sup> fragments decreased, and as a consequence, the contribution of the C<sub>x</sub>H<sub>y</sub>O<sup>+</sup> fractions increased in photolyzed tar ball aerosols. Comparing to the fresh tar ball mass spectra, alkyl/alkenyl chains, carboxylic acids/peroxides (CO<sub>2</sub><sup>+</sup>, CHO<sub>2</sub><sup>+</sup>), and carbonyl/aldehyde groups (CO<sup>+</sup>, CHO<sup>+</sup>, C<sub>2</sub>H<sub>3</sub>O<sup>+</sup>) fragments depleted due to irradiation by UV light. Furthermore, increase of the *f*<sub>44</sub>/*f*<sub>43</sub> ratio with photolysis shown in Figure S14, indicates decay of CO<sub>2</sub><sup>+</sup> to a less extent compared to the loss of C<sub>2</sub>H<sub>3</sub>O<sup>+</sup>. Photolysis occurs in the condensed phase as particles containing photolabile compounds that efficiently absorb light at actinic wavelengths. Oxygenated species such as carbonyls, carboxylic acids, and peroxides are more vulnerable to photolysis, especially in the UV. With cleavage of the oxygenated functional groups, molecules become more volatile and may desorb to the gas phase (Henry and Donahue, 2012). Considerable amount of VOCs productions, including small molecular acids, ketones, aldehydes (e.g., acetic acid, formic acid, acetaldehyde, acetone, etc.), and hydrocarbon species (e.g., methane, ethene, propane, etc.), were detected from photo-degradation of various SOA (Malecha and Nizkorodov, 2016; Mang et al., 2008), and photocleavage of carbonyls has been emphasized in photolysis of SOA. Bateman et al. (2011) reported that exposure to UV irradiation increased the O/C ratio of dissolved ambient SOA, and they attributed the chemical changes to photodissociation of molecules containing carbonyl groups and net production of carboxylic acids that overweigh their decomposition in pH modified solution. Detailed mechanisms were proposed such as *n*- $\pi$ \* Norrish type-I and -II splitting of carbonyls and *n*- $\sigma$ \* photolysis of peroxides to form production of carboxylic acids in the presence of dissolved oxygen (Norrish, 1934; Pitts et al., 1964).

In the current experiments, photolysis occurred in particle phase which can be different from photolysis in liquid phase. First, the photolysis of particles should be less efficient as quenching is more likely and fragment caging can prevent rapid recombination. Second, photolysis products (volatile molecules and radicals) can more easily transfer to the gas phase rather than accumulate in the solution and be involved in further reactions. Epstein et al. (2014) isolated photolysis influence on  $\alpha$ -pinene SOA. They reported suppression of SOA mass loading and marked decomposition of particle-bound organic peroxides from UV light illumination. The fraction of C<sub>x</sub>H<sub>y</sub><sup>+</sup> fragments slightly decreased while the oxygenated fragments increased upon irradiation. Wong et al. (2014) highlighted RH-dependent photolysis as a sink for SOA in the atmosphere, in particular, photolysis results in more oxidized SOA due to kinetic preference for degradation of less oxidized components, and they attributed the slower decay of *f*<sub>44</sub> (CO<sub>2</sub><sup>+</sup>) to photodissociation of peroxides and the formation of carboxylic acids in SOA upon UV irradiation.

The optical properties of SOA can change upon photolysis of photolabile carbonyl/carboxylic organics, peroxides, and other chromophores. Liu et al. (2016) investigated the influences of various environmental factors on light absorption of aromatic SOA from ozonolysis in the presence of NO<sub>x</sub>. They suggested that photolysis, rather than hydrolysis, bleached SOA absorption due to degradation of nitrogen-containing chromophores. This conclusion was also confirmed by similar studies by Lee et al. (2014) and Aiona et al. (2018). In our study, the changes in the optical properties as a function of O/C ratio for tar balls upon photolysis are

shown in Figure S16. The relevant parameters are summarized in Table S7, MAC changes for tar ball upon photolysis are presented in Figure S17. RI of both real and imaginary parts weakly diminished during irradiation, and the average RI at 375 nm decreased by  $0.012+0.006i$  for maximum photolyzed tar ball, corresponded MAC at 375 nm decreased by ~31.3%.

**Table S6.** Summary of mass spectra characters and effective density changes for tar ball particles upon photolysis from UV light irradiation (mean  $\pm$  standard deviation)

<b>Tar ball</b>	<b>O:C</b>	<b>H:C</b>	<b>N:C</b>	<b>m/z&gt;100 fraction</b>	<b>density</b>
Fresh	0.25 $\pm$ 0.01	1.55 $\pm$ 0.01	0.012 $\pm$ 0.002	0.32	1.24 $\pm$ 0.01
P1	0.26 $\pm$ 0.01	1.53 $\pm$ 0.01	0.013 $\pm$ 0.003	0.33	1.24 $\pm$ 0.01
P2	0.27 $\pm$ 0.01	1.51 $\pm$ 0.01	0.011 $\pm$ 0.001	0.32	1.24 $\pm$ 0.01
P3	0.29 $\pm$ 0.01	1.49 $\pm$ 0.01	0.012 $\pm$ 0.002	0.33	1.24 $\pm$ 0.01

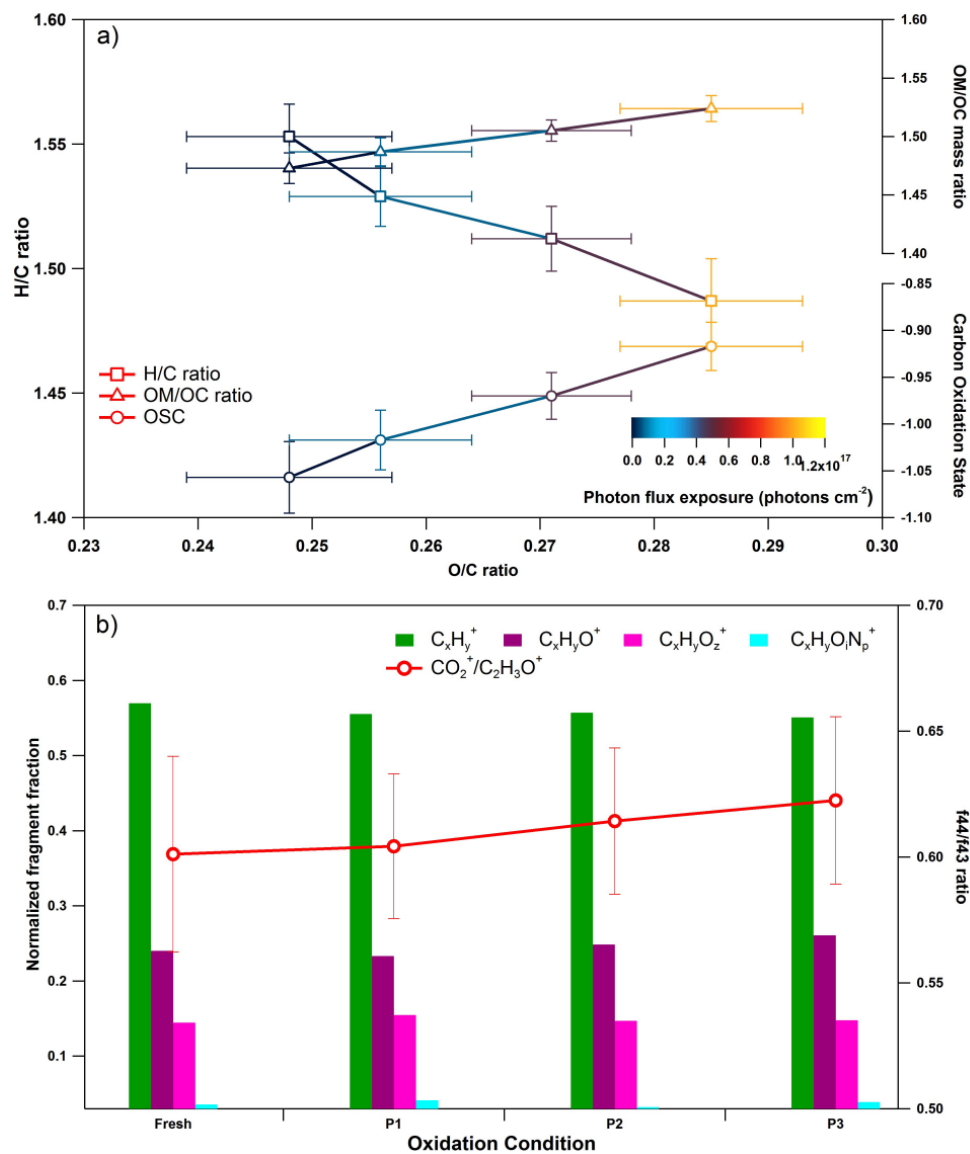


**Figure S14.** Dynamic changes for chemical characteristics of tar ball particle upon UV light irradiation: a) OM/OC, H/C ratio, and average carbon oxidation state ( $\overline{OSC}$ ) changes as a function of O/C ratio; b) mass spectra evolution with photolysis extension in term of C<sub>x</sub>H<sub>y</sub><sup>+</sup>, C<sub>x</sub>H<sub>y</sub>O<sup>+</sup>, C<sub>x</sub>H<sub>y</sub>O<sub>2</sub><sup>+</sup>, and C<sub>x</sub>H<sub>y</sub>O<sub>z</sub>N<sub>p</sub><sup>+</sup> fragment groups

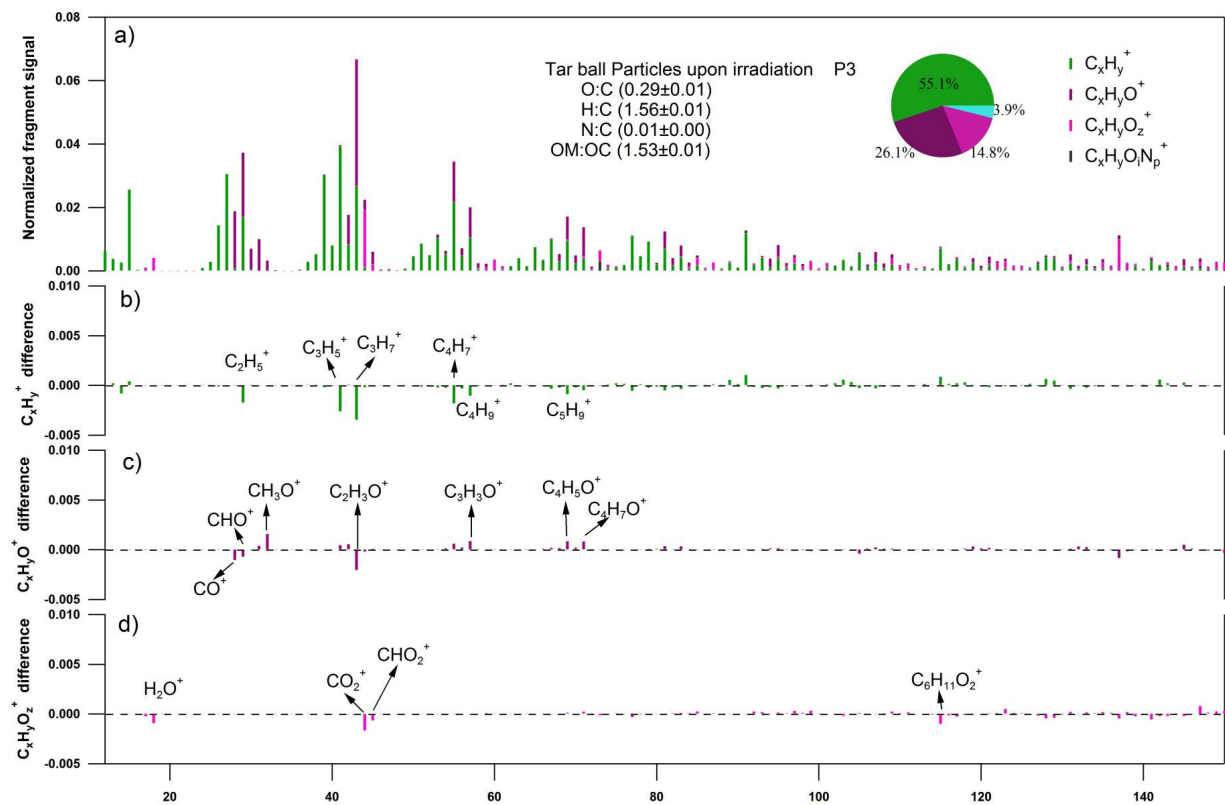


**Figure S15.** High-resolution mass spectra changes for nonpolar tar ball particles after maximum photolysis in P3 test, four ion groups were grouped for clarity as:  $C_xH_y^+$ ,  $C_xH_yO^+$ ,  $C_xH_yO_z^+$  ( $z>1$ ),  $C_xH_yO_zN_p^+$  ( $i\geq 0, p\geq 1$ ). Ions  $O^+$ ,  $OH^+$ , and  $H_2O^+$  were included in the  $C_xH_yO_z^+$  group. Mass fraction of the four fragment groups was pie-chart presented. a) normalized mass spectra of aged tar ball particles, b)-d) changes of  $C_xH_y^+$ ,  $C_xH_yO^+$ ,  $C_xH_yO_z^+$ , and  $C_xH_yO_zN_p^+$  comparing with fresh tar ball normalized mass spectra



**Table S7. Summary of RI and Ångström exponent changes for tar ball particles upon photolysis (mean ± standard deviation)**

Tar ball	Complex Refractive index			SSA (average)	Å <sub>abs</sub>	Å <sub>abs_UVVIS</sub>	Å <sub>ext</sub>
	Average	375nm	405nm				
Fresh	(1.661±0.008)+(0.020±0.004)i	(1.671±0.003)+(0.025±0.003)i	(1.659±0.011)+(0.017±0.002)i	0.89 ± 0.01	5.87 ± 0.37	6.74	3.81 ± 0.18
P1	(1.658±0.010)+(0.022±0.006)i	(1.668±0.001)+(0.027±0.001)i	(1.653±0.002)+(0.018±0.001)i	0.88 ± 0.02	6.92 ± 0.60	6.59	3.94 ± 0.03
P2	(1.649±0.008)+(0.018±0.004)i	(1.656±0.002)+(0.023±0.002)i	(1.647±0.002)+(0.014±0.003)i	0.90 ± 0.02	6.99 ± 1.22	6.50	3.79 ± 0.05
P3	(1.649±0.010)+(0.015±0.004)i	(1.659±0.005)+(0.019±0.004)i	(1.644±0.004)+(0.013±0.003)i	0.92 ± 0.01	7.42 ± 0.53	6.56	4.01 ± 0.01

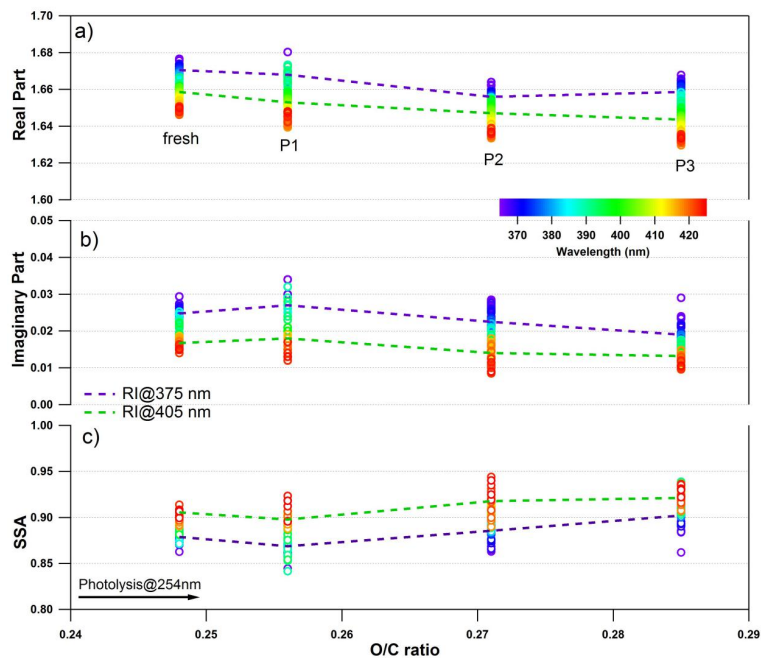


**Figure S16.** Changes in the retrieved spectral-dependent complex RI and SSA as a function of O/C ratio for tar ball particles upon 254 nm illumination: a) real part, b) imaginary part, and c) SSA calculated for 150 nm particles. The color scale shows the span in the RI for the wavelengths measured from 365 to 425 nm. For clarity, error bars for O/C ratio ( $\pm 0.01$ ), RI ( $\pm 0.008$  for real part, and  $\pm 0.003$  for imaginary part on average) and SSA ( $\pm 0.006$ ) are not shown. The two dashed lines trace RI and SSA at 375 nm (purple) and 405 nm (green). P1~P3 represent photolysis studies with low to maximal photon flux exposures.

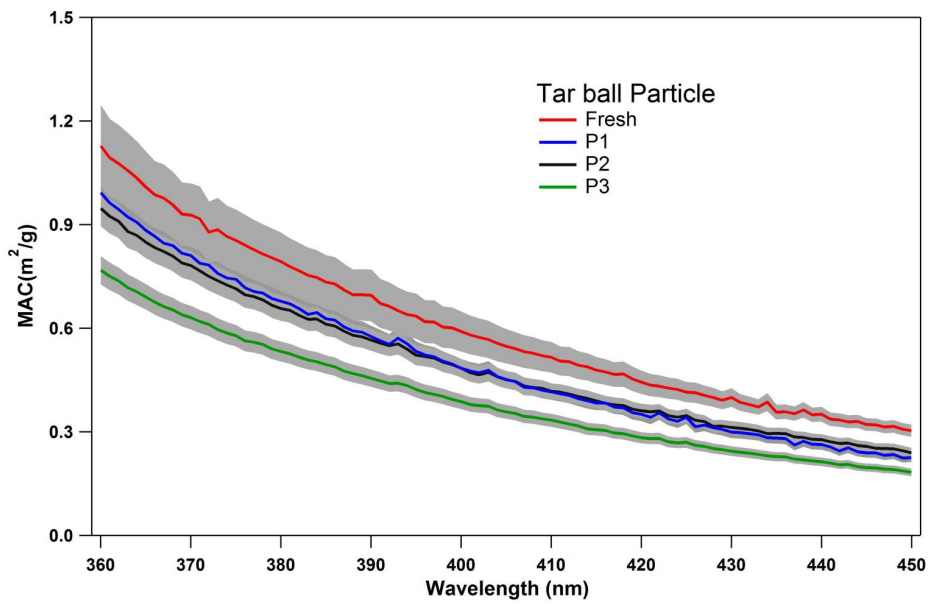


Figure S17. Changes of tar ball BrC mass absorption cross section (MAC) as a function of wavelength upon UV photolysis

### 15. Optical and chemical changes of tar ball aerosols due to O<sub>3</sub> oxidation

Prior to photochemical aging experiments, blank test of tar ball oxidation via O<sub>3</sub> under dark was conducted in the OFR. Initial environmental conditions (e.g., O<sub>3</sub> and tar balls concentrations, relative humidity, residence time, etc) were maintained the same with following daytime evolution simulations, while UV lamps were not turned on. Dynamic optical and chemical changes for tar balls were characterized and presented in Figure S18 and S19. We did not observe significant refractive index changes for tar balls after 28.6 ppm O<sub>3</sub> oxidation, taking ambient O<sub>3</sub> concentration of 50 ppb, equivalent atmospheric O<sub>3</sub> exposure for tar balls through the OFR was about one day. RIs of fresh tar ball are  $(1.671 \pm 0.003) + (0.025 \pm 0.003)i$  and  $(1.659 \pm 0.011) + (0.017 \pm 0.002)i$  at 375 and 405 nm, respectively. After O<sub>3</sub> oxidation, RIs became  $(1.677 \pm 0.012) + (0.023 \pm 0.003)i$  and  $(1.668 \pm 0.011) + (0.013 \pm 0.004)i$  at 375 and 405 nm, respectively. In Figure S19, O<sub>3</sub> oxidation weakly increased O/C and OM/OC ratios of tar balls, O/C ratio increased by 0.02 from initial 0.25, and OM/OC increased from 1.47 to 1.50, while H/C ratio remained during O<sub>3</sub> oxidation of tar ball particles. It was found C<sub>x</sub>H<sub>y</sub><sup>+</sup> fractions slight decreased in compensation of more C<sub>x</sub>H<sub>y</sub>O<sup>+</sup> and C<sub>x</sub>H<sub>y</sub>O<sub>z</sub><sup>+</sup> fragments formation, indicating oxygenated moieties produced.

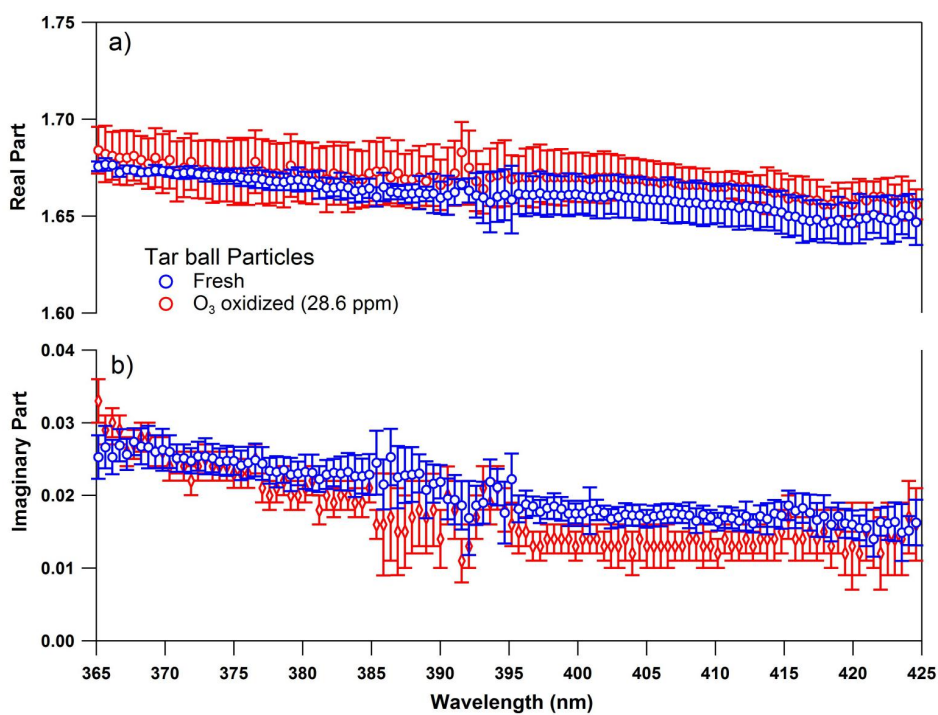
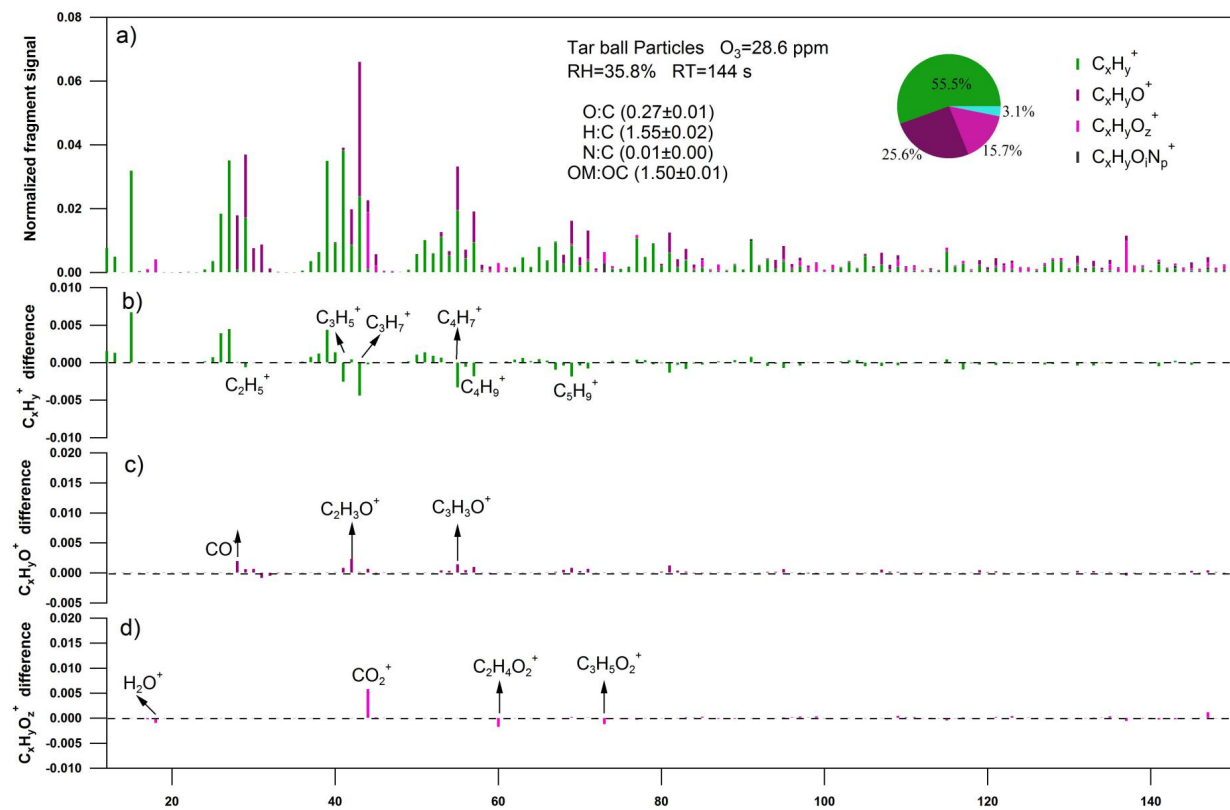


Figure S18. Refractive index as a function of wavelength for fresh and O<sub>3</sub> oxidized tar balls, a) real part, b) imaginary part



**Figure S19.** High-resolution mass spectral changes for nonpolar tar ball particles oxidized via  $O_3$ . Four ion groups were grouped for clarity:  $C_xH_y^+$ ,  $C_xH_yO^+$ ,  $C_xH_yO_z^+$  ( $z > 1$ ),  $C_xH_yO_iN_p^+$  ( $i \geq 0, p \geq 1$ ). Ions  $O^+$ ,  $OH^+$ , and  $H_2O^+$  were included in the  $C_xH_yO_z^+$  group. Mass fraction of the four fragment groups was pie-chart presented. a) normalized mass spectra of  $O_3$  oxidized tar ball particles, b)-d) changes of  $C_xH_y^+$ ,  $C_xH_yO^+$ ,  $C_xH_yO_z^+$ , and  $C_xH_yO_iN_p^+$  comparing with fresh tar ball normalized mass spectra

## 16. Mass spectra characters and effective density changes for tar ball particles upon photochemical oxidation

**Table S8.** Summary of mass spectra characters and effective density changes for tar ball particles upon photochemical oxidation (mean  $\pm$  standard deviation)

<b>Tar ball</b>	<b>O:C</b>	<b>H:C</b>	<b>N:C</b>	<b>m/z&gt;100 fraction</b>	<b>density</b>
Fresh	0.25 $\pm$ 0.01	1.55 $\pm$ 0.01	0.012 $\pm$ 0.002	0.32	1.24 $\pm$ 0.01
O_0.7	0.32 $\pm$ 0.01	1.59 $\pm$ 0.01	0.012 $\pm$ 0.000	0.28	1.24 $\pm$ 0.01
O_1.7	0.35 $\pm$ 0.01	1.60 $\pm$ 0.01	0.009 $\pm$ 0.002	0.24	1.24 $\pm$ 0.01
O_3.9	0.35 $\pm$ 0.01	1.59 $\pm$ 0.01	0.010 $\pm$ 0.003	0.24	1.24 $\pm$ 0.01
O_6.7	0.38 $\pm$ 0.01	1.62 $\pm$ 0.03	0.011 $\pm$ 0.001	0.21	1.24 $\pm$ 0.01
N_0.5	0.37 $\pm$ 0.01	1.57 $\pm$ 0.02	0.012 $\pm$ 0.001	0.25	1.25 $\pm$ 0.01
N_2.0	0.41 $\pm$ 0.01	1.58 $\pm$ 0.01	0.015 $\pm$ 0.004	0.25	1.26 $\pm$ 0.01

### 17. Detailed mass spectra changes for tar ball upon 6.7 EAD photochemical aging

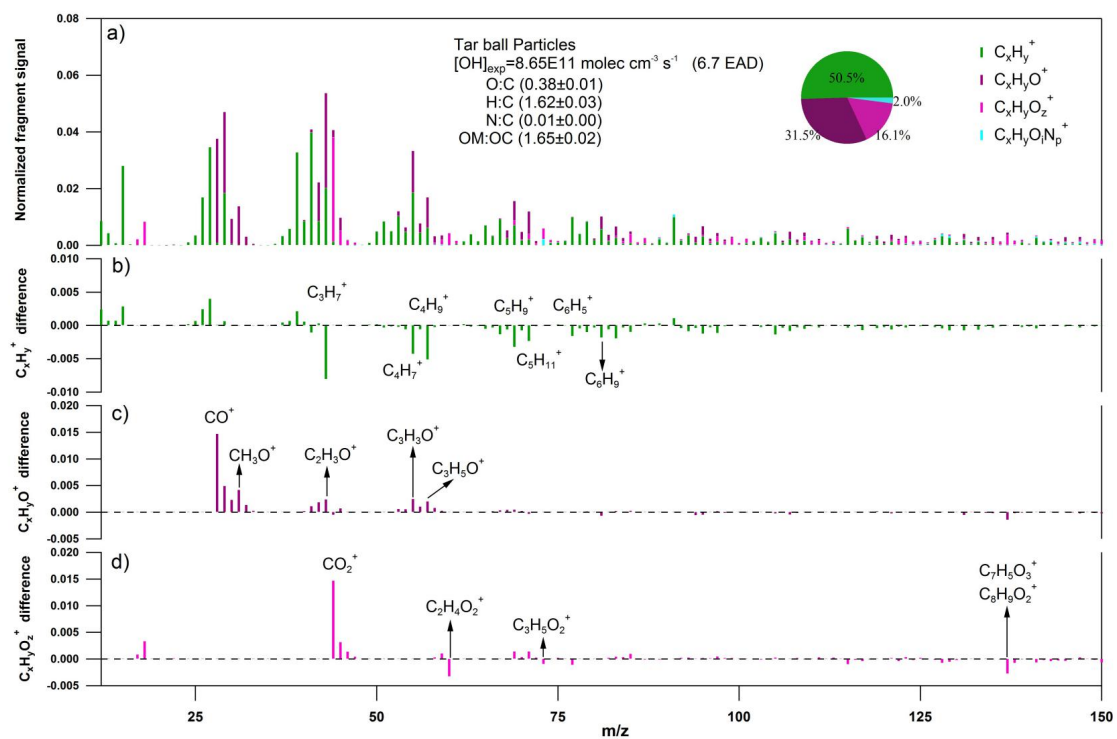


**Figure S20.** High-resolution mass spectral changes for nonpolar tar ball particles upon 6.7 EAD photochemical oxidation in absence of NOx. Four ion groups were grouped for clarity:  $\text{C}_x\text{H}_y^+$ ,  $\text{C}_x\text{H}_y\text{O}^+$ ,  $\text{C}_x\text{H}_y\text{O}_z^+$  ( $z > 1$ ),  $\text{C}_x\text{H}_y\text{O}_i\text{N}_p^+$  ( $i \geq 0, p \geq 1$ ). Ions  $\text{O}^+$ ,  $\text{OH}^+$ , and  $\text{H}_2\text{O}^+$  were included in the  $\text{C}_x\text{H}_y\text{O}_z^+$  group. Mass fraction of the four fragment groups was pie-chart presented. a) normalized mass spectra of 6.7 EAD aged tar ball particles, b)–d) changes of  $\text{C}_x\text{H}_y^+$ ,  $\text{C}_x\text{H}_y\text{O}^+$ ,  $\text{C}_x\text{H}_y\text{O}_z^+$ , and  $\text{C}_x\text{H}_y\text{O}_i\text{N}_p^+$  comparing with fresh tar ball normalized mass spectra

18. Standard AMS spectra for inorganic salt of  $\text{NH}_4\text{NO}_3$

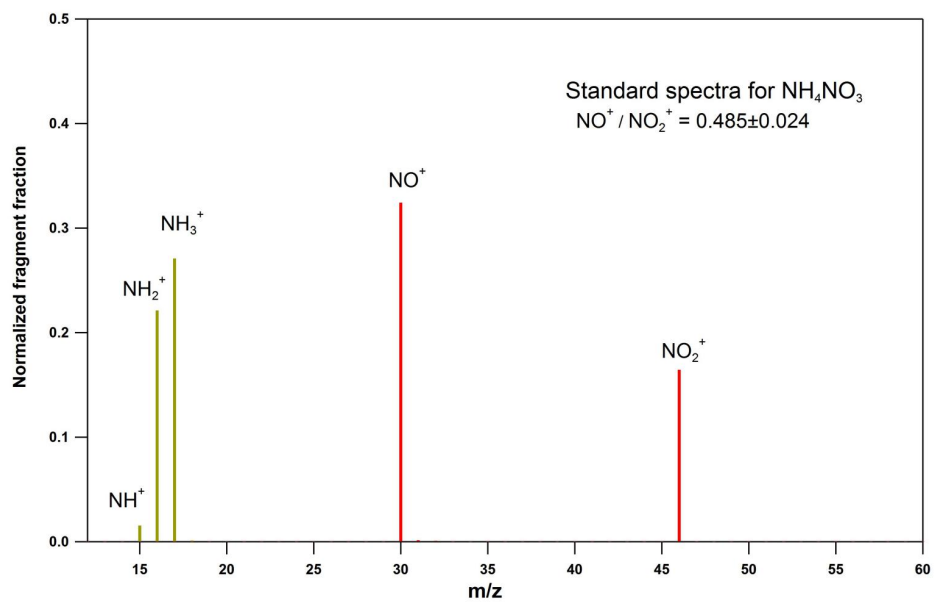
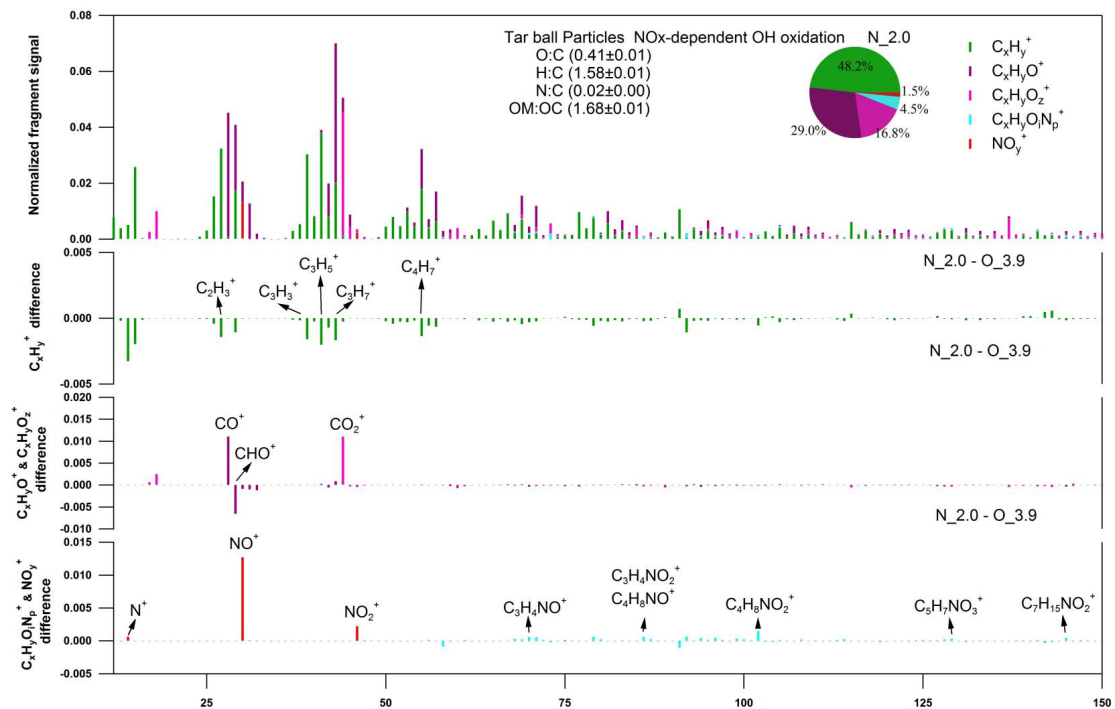


Figure S21. Standard mass spectra for  $\text{NH}_4\text{NO}_3$  measured using HR-ToF-AMS system:  $\text{NO}^+$  and  $\text{NO}_2^+$  for nitrate,  $\text{NH}^+$ ,  $\text{NH}_2^+$ , and  $\text{NH}_3^+$  for ammonium

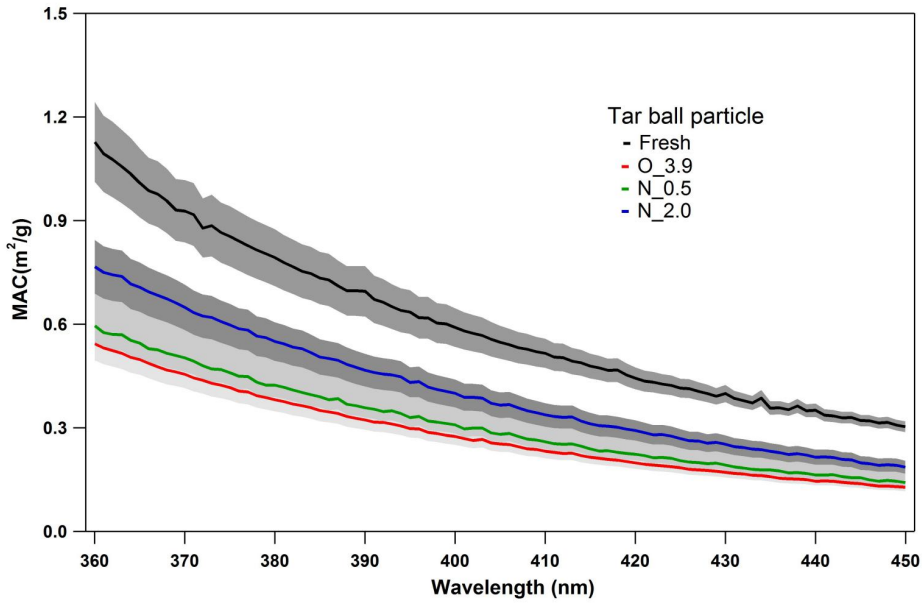
19. Detailed mass spectra changes for tar ball aerosols upon 4 EAD photochemical aging with 2.0 vol.% N<sub>2</sub>O addition



**Figure S22.** High-resolution mass spectra changes for nonpolar tar ball particles upon photochemical oxidation in presence of  $NO_x$ , five ion groups were grouped for clarity as:  $C_xH_y^+$ ,  $C_xH_yO^+$ ,  $C_xH_yO_z^+$  ( $z>1$ ),  $C_xH_yO_pN_p^+$  ( $i\geq 0, p\geq 1$ ), and  $NO_y^+$  ( $NO^+$  and  $NO_2^+$ ). Ions  $O^+$ ,  $OH^+$ , and  $H_2O^+$  were included in the  $C_xH_yO_z^+$  group. Mass fraction of the four fragment groups was pie-chart presented. a) normalized mass spectra of aged tar ball particles, b)-d) changes of  $C_xH_y^+$ ,  $C_xH_yO^+$ ,  $C_xH_yO_z^+$ ,  $C_xH_yO_pN_p^+$ , and  $NO_y^+$  comparing with photochemical oxidized tar ball in absence of  $NO_x$

1  
2

20. Methanol extractable BrC mass absorption cross section (MAC) for tar ball aerosols upon various NOx-dependent photochemical aging processes



3

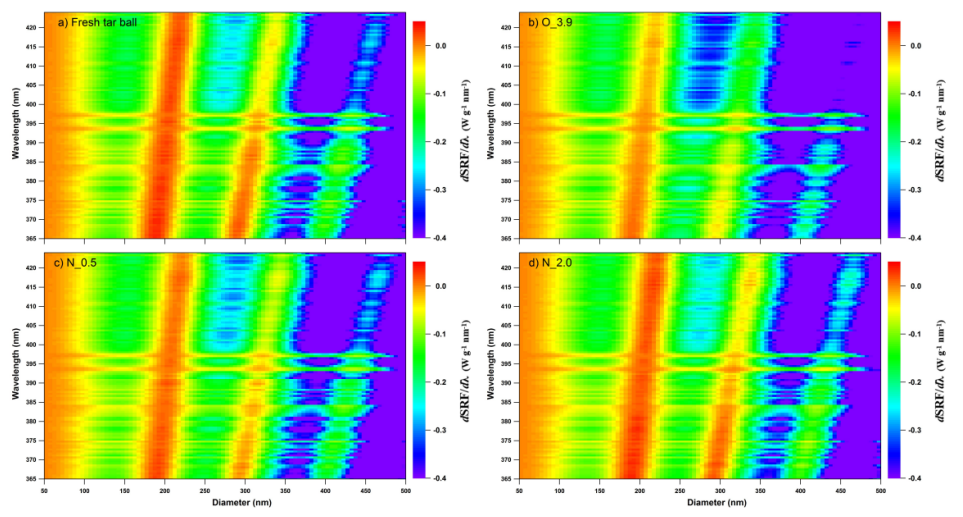
4

Figure S23. Methanol extractable BrC mass absorption cross section (MAC) for tar ball upon NOx-dependent photochemical oxidation as a function of wavelength

5

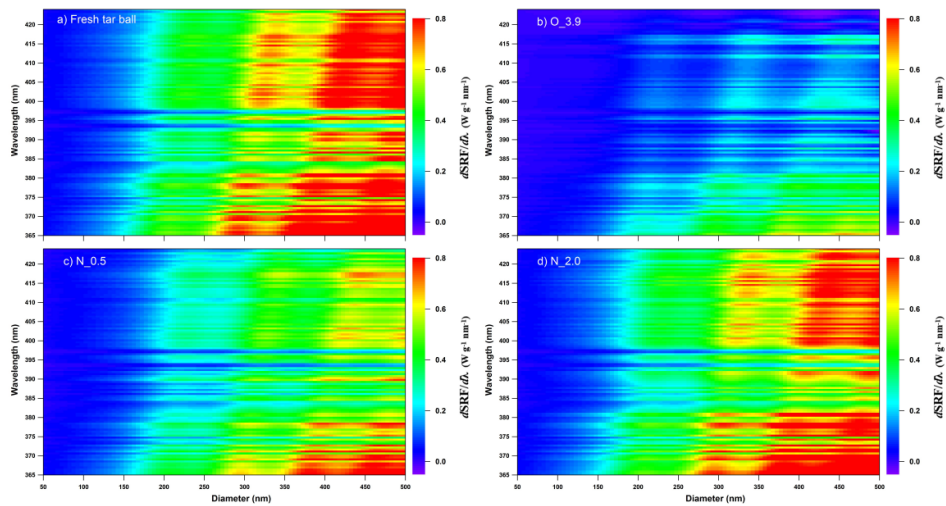
6

7 21. Particle size- and light wavelength-resolved radiative forcing for tar ball aerosols oxidized via various NO<sub>x</sub>-dependent  
8 oxidation processes



9

0 **Figure S24.** Ground based size-resolved radiative forcing spectra over solar irradiation of 365~425 nm for tar ball under various  
1 oxidation: a) fresh tar ball, b) 3.9 EAD daytime photochemical oxidized tar ball, c) photooxidized tar ball with 0.5 vol.% N<sub>2</sub>O  
2 addition, d) photooxidized tar ball with 2.0 vol.% N<sub>2</sub>O addition.  
3



4

5

6

7

8

9

**Figure S25.** Snow based size-resolved radiative forcing spectra over solar irradiation of 365–425 nm for tar ball under various oxidation: a) fresh tar ball, b) 3.9 EAD OH initiated photochemical oxidized tar ball, c) photooxidized tar ball with 0.5 vol.% N<sub>2</sub>O addition, d) photooxidized tar ball with 2.0 vol.% N<sub>2</sub>O addition.

0 **Reference**

- 1 Adler, G., Flores, J. M., Abo Riziq, A., Borrmann, S., and Rudich, Y.: Chemical, physical, and optical evolution of biomass  
2 burning aerosols: a case study, *Atmos. Chem. Phys.*, 11, 1491-1503, doi:10.5194/acp-11-1491-2011, 2011.
- 3 Aiken, A. C., Decarlo, P. F., Kroll, J. H., Worsnop, D. R., Huffman, J. A., Docherty, K. S., Ulbrich, I. M., Mohr, C., Kimmel,  
4 J. R., and Sueper, D.: O:C and OM/OC ratios of primary, secondary, and ambient organic aerosols with high-resolution  
5 time-of-flight aerosol mass spectrometry, *Environ. Sci. Technol.*, 42, 4478-4485, doi:10.1021/es703009q, 2008.
- 6 Aiona, P. K., Luek, J. L., Timko, S. A., Powers, L., Gonsior, M., and Nizkorodov, S. A.: Effect of Photolysis on Absorption  
7 and Fluorescence Spectra of Light-Absorbing Secondary Organic Aerosols, *ACS Earth Space Chem.*, 2, 235-245,  
8 doi:10.1021/acsearthspacechem.7b00153, 2018.
- 9 [Andreae, M., and Gelencsér, A.: Black carbon or brown carbon? The nature of light-absorbing carbonaceous aerosols,](#)  
0 [Atmos. Chem. Phys.](#), 6, 3131-3148, doi:10.5194/acp-6-3131-2006, 2006.
- 1 [Arora, P., and Jain, S.: Estimation of organic and elemental carbon emitted from wood burning in traditional and improved](#)  
2 [cookstoves using controlled cooking test, Environ. Sci. Technol.](#), 49, 3958-3965, doi:10.1021/es504012v, 2015.
- 3 Bateman, A. P., Nizkorodov, S. A., Laskin, J., and Laskin, A.: Photolytic processing of secondary organic aerosols dissolved  
4 in cloud droplets, *Phys. Chem. Chem. Phys.*, 13, 12199-12212, doi:10.1039/C1CP20526A, 2011.
- 5 Bente, M., Sklorz, M., Streibel, T., and Zimmermann, R.: Online laser desorption-multiphoton postionization mass  
6 spectrometry of individual aerosol particles: molecular source indicators for particles emitted from different traffic-related  
7 and wood combustion sources, *Anal. Chem.*, 80, 8991-9004, doi:10.1021/ac801295f, 2008.
- 8 Bruns, E., Krapf, M., Orasche, J., Huang, Y., Zimmermann, R., Drinovec, L., Močnik, G., El-Haddad, I., Slowik, J., and  
9 Dommen, J.: Characterization of primary and secondary wood combustion products generated under different burner loads,  
0 *Atmos. Chem. Phys.*, 15, 2825-2841, doi:10.5194/acp-15-2825-2015, 2015.
- 1 [Chakrabarty, R., Moosmüller, H., Chen, L. W., Lewis, K., Arnott, W., Mazzoleni, C., Dubey, M., Wold, C., Hao, W., and](#)  
2 [Kreidenweis, S.: Brown carbon in tar balls from smoldering biomass combustion, Atmos. Chem. Phys.](#), 10, 6363-6370,  
3 doi:10.5194/acp-10-6363-2010, 2010.
- 4 [China, S., Mazzoleni, C., Gorkowski, K., Aiken, A. C., and Dubey, M. K.: Morphology and mixing state of individual](#)  
5 [freshly emitted wildfire carbonaceous particles, Nature communications](#), 4, 2122, doi:10.1038/ncomms3122, 2013.
- 6 [Chow, J. C., Watson, J. G., Robles, J., Wang, X., Chen, L.-W. A., Trimble, D. L., Kohl, S. D., Tropp, R. J., and Fung, K. K.:](#)  
7 [Quality assurance and quality control for thermal/optical analysis of aerosol samples for organic and elemental carbon, Anal.](#)  
8 [Bioanal. Chem.](#), 401, 3141-3152, doi:10.1007/s00216-011-5103-3, 2011.
- 9 Chýlek, P., Ramaswamy, V., and Cheng, R. J.: Effect of graphitic carbon on the albedo of clouds, *J. Atmos. Sci.*, 41,  
0 3076-3084, doi:10.1175/1520-0469, 1984.

1 d'Almeida, G. A., Koepke, P., and Shettle, E. P.: Atmospheric aerosols: global climatology and radiative characteristics, A.  
2 Deepak Publishing, Hampton, Va, 1991.

3 Epstein, S. A., Blair, S. L., and Nizkorodov, S. A.: Direct photolysis of  $\alpha$ -pinene ozonolysis secondary organic aerosol:  
4 effect on particle mass and peroxide content, *Environ. Sci. Technol.*, 48, 11251-11258, doi:10.1021/es502350u, 2014.

5 [Hand, J. L., Malm, W., Laskin, A., Day, D., Lee, T.-b., Wang, C., Carrico, C., Carrillo, J., Cowin, J. P., and Collett, J.:](#)  
6 [Optical, physical, and chemical properties of tar balls observed during the Yosemite Aerosol Characterization Study, \*J.\*](#)  
7 [Geophys. Res.: Atmos.](#), 110, D21210, doi:10.1029/2004JD005728, 2005.

8 [Han, Y., Han, Z., Cao, J., Chow, J., Watson, J., An, Z., Liu, S., and Zhang, R.:](#) Distribution and origin of carbonaceous  
9 [aerosol over a rural high-mountain lake area, Northern China and its transport significance, \*Atmos. Environ.\*, 42, 2405-2414,](#)  
0 [doi:10.1016/j.atmosenv.2007.12.020, 2008.](#)

1 [Han, Y., Lee, S., Cao, J., Ho, K., and An, Z.:](#) Spatial distribution and seasonal variation of char-EC and soot-EC in the  
2 [atmosphere over China, \*Atmos. Environ.\*, 43, 6066-6073, doi:10.1016/j.atmosenv.2009.08.018, 2009.](#)

3 He, L. Y., Lin, Y., Huang, X. F., Guo, S., Xue, L., Su, Q., Hu, M., Luan, S. J., and Zhang, Y. H.: Characterization of  
4 high-resolution aerosol mass spectra of primary organic aerosol emissions from Chinese cooking and biomass burning,  
5 *Atmos. Chem. Phys.*, 10, 11535-11543, doi:10.5194/acp-10-11535-2010, 2010.

6 Henry, K. M., and Donahue, N. M.: Photochemical aging of  $\alpha$ -pinene secondary organic aerosol: effects of OH radical  
7 sources and photolysis, *J. Phys. Chem. A*, 116, 5932-5940, doi:10.1021/jp210288s, 2012.

8 Hoffmann, D., Iinuma, Y., and Herrmann, H.: Development of a method for fast analysis of phenolic molecular markers in  
9 biomass burning particles using high performance liquid chromatography/atmospheric pressure chemical ionisation mass  
0 spectrometry, *J. Chromatography A*, 1143, 168-175, doi:10.1016/j.chroma.2007.01.035, 2007.

1 Jacobson, M. Z.: Analysis of aerosol interactions with numerical techniques for solving coagulation, nucleation,  
2 condensation, dissolution, and reversible chemistry among multiple size distributions, *J. Geophys. Res.-Atmos.*, 107, D19,  
3 4366, doi:10.1029/2001JD002044, 2002.

4 Jacobson, M. Z.: Effects of externally-through-internally-mixed soot inclusions within clouds and precipitation on global  
5 climate, *J. Phys. Chem. A*, 110, 6860-6873, doi:10.1021/jp056391r, 2006.

6 [Kim, K. H., Sekiguchi, K., Kudo, S., and Sakamoto, K.:](#) Characteristics of Atmospheric Elemental Carbon (Char and Soot)  
7 [in Ultrafine and Fine Particles in a Roadside Environment, Japan, \*Aerosol Air Qual. Res.\*, 11, 1-12,](#)  
8 [doi:10.4209/aaqr.2010.07.0061, 2011.](#)

9 Lee, H. J., Aiona, P. K., Laskin, A., Laskin, J., and Nizkorodov, S. A.: Effect of solar radiation on the optical properties and  
0 molecular composition of laboratory proxies of atmospheric brown carbon, *Environ. Sci. Technol.*, 48, 10217-10226,  
1 doi:10.1021/es502515r, 2014.

2 Li, C., Hu, Y., Zhang, F., Chen, J., Ma, Z., Ye, X., Yang, X., Wang, L., Tang, X., and Zhang, R.: Multi-pollutant emissions  
3 from the burning of major agricultural residues in China and the related health-economic effects, *Atmos. Chem. Phys.*, 17,  
4 4957-4988, doi:10.5194/acp-17-4957-2017, 2017.

5 Li, Y., Huang, D., Cheung, H. Y., Lee, A., and Chan, C. K.: Aqueous-phase photochemical oxidation and direct photolysis of  
6 vanillin-a model compound of methoxy phenols from biomass burning, *Atmos. Chem. Phys.*, 14, 2871-2885,  
7 doi:10.5194/acp-14-2871-2014, 2014.

8 Li, Y. J., Yeung, J. W., Leung, T. P., Lau, A. P., and Chan, C. K.: Characterization of organic particles from incense burning  
9 using an aerodyne high-resolution time-of-flight aerosol mass spectrometer, *Aerosol Sci. Tech.*, 46, 654-665,  
0 doi:10.1080/02786826.2011.653017, 2012.

1 [Li, S., Zhu, M., Yang, W., Tang, M., Huang, X., Yu, Y., Fang, H., Yu, X., Yu, Q., and Fu, X.: Filter-based measurement of](#)  
2 [light absorption by brown carbon in PM<sub>2.5</sub> in a megacity in South China, \*Sci. Total Environ.\*, 633, 1360-1369,](#)  
3 [doi:10.1016/j.scitotenv.2018.03.235, 2018.](#)

4 Liu, J., Lin, P., Laskin, A., Laskin, J., Kathmann, S. M., Wise, M., Caylor, R., Imholt, F., Selimovic, V., and Shilling, J. E.:  
5 Optical properties and aging of light-absorbing secondary organic aerosol, *Atmos. Chem. Phys.*, 16, 12815-12827,  
6 doi:10.5194/acp-16-12815-2016, 2016.

7 Malecha, K. T., and Nizkorodov, S. A.: Photodegradation of secondary organic aerosol particles as a source of small,  
8 oxygenated volatile organic compounds, *Environ. Sci. Technol.*, 50, 9990-9997, doi:10.1021/acs.est.6b02313, 2016.

9 Mandalakis, M., Gustafsson, Ö., Alsberg, T., Egeback, A. L., Reddy, C. M., Xu, L., Klanova, J., Holoubek, I., and  
0 Stephanou, E. G.: Contribution of biomass burning to atmospheric polycyclic aromatic hydrocarbons at three European  
1 background sites, *Environ. Sci. Technol.*, 39, 2976-2982, doi:10.1021/es048184v, 2005.

2 Mang, S. A., Henricksen, D. K., Bateman, A. P., Andersen, M. P. S., Blake, D. R., and Nizkorodov, S. A.: Contribution of  
3 carbonyl photochemistry to aging of atmospheric secondary organic aerosol, *J. Phys. Chem. A*, 112, 8337-8344,  
4 doi:10.1021/jp804376c, 2008.

5 Ng, N., Canagaratna, M., Zhang, Q., Jimenez, J., Tian, J., Ulbrich, I., Kroll, J., Docherty, K., Chhabra, P., and Bahreini, R.:  
6 Organic aerosol components observed in Northern Hemispheric datasets from Aerosol Mass Spectrometry, *Atmos. Chem.*  
7 *Phys.*, 10, 4625-4641, doi:10.5194/acp-10-4625-2010, 2010.

8 Ng, N., Canagaratna, M., Jimenez, J., Chhabra, P., Seinfeld, J., and Worsnop, D.: Changes in organic aerosol composition  
9 with aging inferred from aerosol mass spectra, *Atmos. Chem. Phys.*, 11, 6465-6474, doi:10.5194/acp-11-6465-2011, 2011.

0 Norrish, R. G.: Part II. Free radicals of short life: chemical aspects. A. General and inorganic. The primary photochemical  
1 production of some free radicals, *Transactions of the Faraday Society*, 30, 103-113, 1934.

2 Passig, J., Schade, J., Oster, M., Fuchs, M., Ehlert, S., Jäger, C., Sklorz, M., and Zimmermann, R.: Aerosol mass  
3 spectrometer for simultaneous detection of polyaromatic hydrocarbons and inorganic components from individual particles,  
4 *Anal. Chem.*, 89, 6341-6345, doi:10.1021/acs.analchem.7b01207, 2017.

5 Pitts, J., Wan, J., and Schuck, E.: Photochemical studies in an alkali halide matrix. I. An o-nitrobenzaldehyde actinometer  
6 and its application to a kinetic study of the photoreduction of benzophenone by benzhydrol in a pressed potassium bromide  
7 disk, *J. Am. Chem. Soc.*, 86, 3606-3610, 1964.

8 [Pósfai, M., Gelencsér, A., Simonics, R., Arató, K., Li, J., Hobbs, P. V., and Buseck, P. R.: Atmospheric tar balls: Particles  
9 from biomass and biofuel burning, \*J. Geophys. Res. Atmos.\*, 109, D06213, doi:10.1029/2003JD004169, 2004.](#)

0 Samburova, V., Connolly, J., Gyawali, M., Yatavelli, R. L., Watts, A. C., Chakrabarty, R. K., Zielinska, B., Moosmüller, H.,  
1 and Khlystov, A.: Polycyclic aromatic hydrocarbons in biomass-burning emissions and their contribution to light absorption  
2 and aerosol toxicity, *Sci. Total Environ.*, 568, 391-401, doi:10.1016/j.scitotenv.2016.06.026, 2016.

3 Santos, G. T., Santos, P. S., and Duarte, A. C.: Vanillic and syringic acids from biomass burning: Behaviour during  
4 Fenton-like oxidation in atmospheric aqueous phase and in the absence of light, *J. Hazard. Mater.*, 313, 201-208,  
5 doi:10.1016/j.jhazmat.2016.04.006, 2016.

6 Sedlacek III, A. J., Buseck, P. R., Adachi, K., Onasch, T. B., Springston, S. R., and Kleinman, L.: Formation and evolution  
7 of Tar Balls from Northwestern US wildfires, *Atmos. Chem. Phys.*, 18, 11289-11301, doi:10.5194/acp-18-11289-2018,  
8 2018.

9 Sumlin, B. J., Pandey, A., Walker, M. J., Pattison, R. S., Williams, B. J., and Chakrabarty, R. K.: Atmospheric  
0 Photooxidation Diminishes Light Absorption by Primary Brown Carbon Aerosol from Biomass Burning, *Environ. Sci.  
1 Technol. Lett.*, 4, 540-545, doi:10.1021/acs.estlett.7b00393, 2017.

2 Sumlin, B. J., Oxford, C. R., Seo, B., Pattison, R. R., Williams, B. J., and Chakrabarty, R. K.: Density and homogeneous  
3 internal composition of primary brown carbon aerosol, *Environ. Sci. Technol.*, 52, 3982-3989, doi:10.1021/acs.est.8b00093,  
4 2018.

5 Takahama, S., Johnson, A., Morales, J. G., Russell, L. M., Duran, R., Rodriguez, G., Zheng, J., Zhang, R., Toom-Saunty, D.,  
6 and Leaitch, W. R.: Submicron organic aerosol in Tijuana, Mexico, from local and Southern California sources during the  
7 CalMex campaign, *Atmos. Environ.*, 70, 500-512, doi:10.1016/j.atmosenv.2012.07.057, 2013.

8 Tang, I. N.: Thermodynamic and optical properties of mixed-salt aerosols of atmospheric importance, *J. Geophys. Res.*  
9 *Atmos.*, 102, 1883-1893, doi:10.1029/96JD03085, 1997.

0 [Tivanski, A. V., Hopkins, R. J., Tylliszczak, T., and Gilles, M. K.: Oxygenated interface on biomass burn tar balls determined  
1 by single particle scanning transmission X-ray microscopy, \*J. Phys. Chem. A\*, 111, 5448-5458, doi:10.1021/jp070155u,  
2 2007.](#)

Formatted: Complex Script Font: 10.5 pt

3 Veres, P., Roberts, J. M., Burling, I. R., Warneke, C., de Gouw, J., and Yokelson, R. J.: Measurements of gas-phase  
4 inorganic and organic acids from biomass fires by negative-ion proton-transfer chemical-ionization mass spectrometry, *J.*  
5 *Geophys. Res. Atmos.*, 115, doi:10.1029/2010JD014033, 2010.

6 Wong, J. P., Nenes, A., and Weber, R. J.: Changes in light absorptivity of molecular weight separated brown carbon due to  
7 photolytic aging, *Environ. Sci. Technol.*, 51, 8414-8421, doi:10.1021/acs.est.7b01739, 2017.

8 Wong, J. P., Zhou, S., and Abbatt, J. P.: Changes in secondary organic aerosol composition and mass due to photolysis:  
9 relative humidity dependence, *J. Phys. Chem. A*, 119, 4309-4316, doi:10.1021/jp506898c, 2014.

0 Yee, L., Kautzman, K., Loza, C., Schilling, K., Coggon, M., Chhabra, P., Chan, M., Chan, A., Hersey, S., and Crouse, J.:  
1 Secondary organic aerosol formation from biomass burning intermediates: phenol and methoxyphenols, *Atmos. Chem.*  
2 *Phys.*, 13, 8019-8043, doi:10.5194/acp-13-8019-2013, 2013.

3 Zhou, S., Collier, S., Jaffe, D. A., Briggs, N. L., Hee, J., Sedlacek III, A. J., Kleinman, L., Onasch, T. B., and Zhang, Q.:  
4 Regional influence of wildfires on aerosol chemistry in the western US and insights into atmospheric aging of biomass  
5 burning organic aerosol, *Atmos. Chem. Phys.*, 17, 2477-2493, doi:10.5194/acp-17-2477-2017, 2017.

6  
7